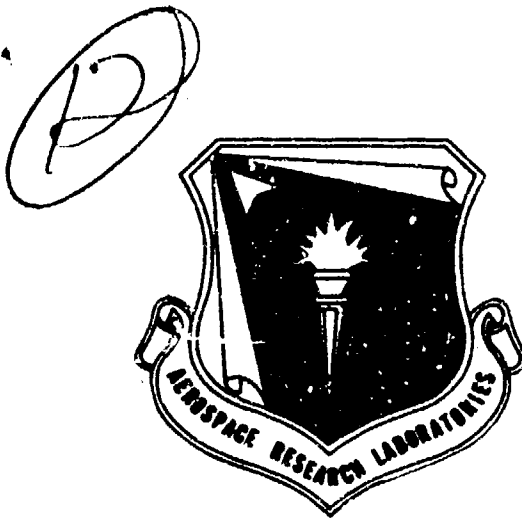


ARL TR 75-0194



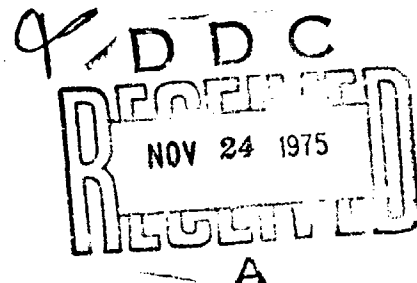
## INFLUENCE OF MICROSTRUCTURE AND SECOND PHASES ON FRACTURE TOUGHNESS

**BATTELLE**  
**COLUMBUS LABORATORIES**  
**COLUMBUS, OHIO 43201**

JUNE 1975

FINAL REPORT 1 JUNE 1971 — 31 MAY 1974

Approved for public release; distribution unlimited



**METALLURGY & CERAMICS RESEARCH LABORATORY/LL**  
**AEROSPACE RESEARCH LABORATORIES**  
**Building 450 — Area B**  
**Wright-Patterson Air Force Base, Ohio 45433**

**AIR FORCE SYSTEMS COMMAND**  
**United States Air Force**



## NOTICES

When Government drawings, specifications, or other data are used for any purpose other than in connection with a definitely related Government procurement operation, the United States Government thereby incurs no responsibility nor any obligation whatsoever; and the fact that the Government may have formulated, furnished, or in any way supplied the said drawings, specifications, or other data, is not to be regarded by implication or otherwise as in any manner licensing the holder or any other person or corporation, or conveying any rights or permission to manufacture, use, or sell any patented invention that may in any way be related thereto.

Organizations or individuals receiving reports via Aerospace Research Laboratories automatic mailing lists should refer to the ARL number of the report received when corresponding about change of address or cancellation. Such changes should be directed to the specific laboratory originating the report. Do not return this copy; retain or destroy.

Reports are not stocked by the Aerospace Research Laboratories. Copies may be obtained from:

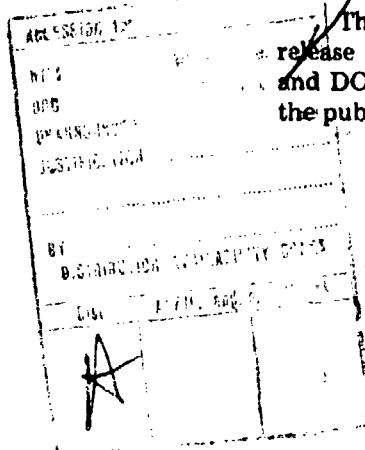
National Technical Information Services  
Clearinghouse  
Springfield, VA 22161

This technical report has been reviewed and is approved for publication.

FOR THE COMMANDER:

*Elizabeth Day*  
ELIZABETH DAY  
Technical Documents  
and STINFO Office

This report has been reviewed and cleared for open publication and public release by the appropriate Office of Information in accordance with AFR 190-12 and DODD 5230.0. There is no objection to unlimited distribution of this report to the public at large, or by DDC to the National Technical Information Service.



## UNCLASSIFIED

SECURITY CLASSIFICATION OF THIS PAGE (When Data Entered)

17) REPORT DOCUMENTATION PAGE		READ INSTRUCTIONS BEFORE COMPLETING FORM
1. REPORT NUMBER ARL-75-0194	2. GOVT ACCESSION NO.	3. RECIPIENT'S CATALOG NUMBER
4. TITLE (and Subtitle) INFLUENCE OF MICROSTRUCTURE AND SECOND PHASES / ON FRACTURE TOUGHNESS.		5. TYPE OF REPORT & PERIOD COVERED FINAL TECHNICAL 1 Jul. 71-31 May 74
7. AUTHOR(S) G. T. Hahn C. R. Barnes A. R. Rosenfield		6. PERFORMING ORG. REPORT NUMBER F33615-71-C-1915
9. PERFORMING ORGANIZATION NAME AND ADDRESS BATTELLE Columbus Laboratories Columbus, Ohio 43201		10. PROGRAM ELEMENT, PROJECT, TASK AREA & WORK UNIT NUMBERS 61102F 702101 11-3131
11. CONTROLLING OFFICE NAME AND ADDRESS METALLURGY & CERAMICS RESEARCH LAB (LL) AEROSPACE RESEARCH LABORATORIES (AFSC) WRIGHT-PATTERSON AFB, OHIO 45433		12. REPORT DATE June 1975
14. MONITORING AGENCY NAME & ADDRESS (if different from Controlling Office)		13. NUMBER OF PAGES 117
16. DISTRIBUTION STATEMENT (of this Report) Approved for public release; distribution unlimited.		15. SECURITY CLASS. (of this report) UNCLASSIFIED
17. DISTRIBUTION STATEMENT (of the abstract entered in Block 20, if different from Report)		18. DECLASSIFICATION/DOWNGRADING SCHEDULE
18. SUPPLEMENTARY NOTES		
19. KEY WORDS (Continue on reverse side if necessary and identify by block number) fracture toughness 7000-series aluminum alloy shear rupture plane strain ductility slip band offset grain boundary sliding micromechanisms plastic instability inclusions AISI 4340, Maraging Steel strain localization precipitate particles		
20. ABSTRACT (Continue on reverse side if necessary and identify by block number) The microstructure, second phases, and micromechanisms contributing to fracture toughness of AISI 4340 steel, maraging steel, Ti-6Al-4V, and 7000-series aluminum alloys are examined. The study focuses on high strength alloys and the component of toughness arising from strain localization and shear rupture, which is shown to be related to the "plane strain" ductility. Methods of measuring plane strain ductility are examined, and a new double-bend method which can be applied to both plate and sheet coupons is devised. Successive replicas of the bend specimen surface are used to follow the development of slipping regions and cracks under (Continued)		

DD FORM 1 JAN 73 1473 EDITION OF 1 NOV 65 IS OBSOLETE

UNCLASSIFIED

SECURITY CLASSIFICATION OF THIS PAGE (When Data Entered)

UNCLASSIFIED

SECURITY CLASSIFICATION OF THIS PAGE(When Data Entered)

"plane strain" biaxial loading, and to measure slip offsets. The alloys display a tendency for a more coordinated slipping of neighboring grains under "plane strain" flow leading to strain localization: (a) the formation of coplanar arrays of slip bands or sliding grain boundaries called "superbands", (b) the growth of superbands which can accommodate large shears, (c) initiation of shear microcracks within the bands, and (d) the linking of the cracks into a macrocrack. The susceptibility to strain localization and shear rupture is traced to a number of microstructural elements, including (a) fine, coherent precipitate particles cut by dislocations, (b) inclusions, and (c) the grain size and character of the grain boundaries.

R

UNCLASSIFIED

SECURITY CLASSIFICATION OF THIS PAGE(When Data Entered)

## PREFACE

This final technical report was prepared by Battelle's Columbus Laboratories, Columbus, Ohio, on Contract AF 33615-71-C-1915 for the Aerospace Research Laboratories, United States Air Force.

The report describes work carried out on this contract starting 1 June 1971 and ending 31 May 1974.

The research described was accomplished on Project 7021, "Structure and Properties of Solids" under technical cognizance of the Metallurgy and Ceramics Research Laboratory.

The authors wish to acknowledge the sustaining interest and generous assistance of the late Mr. James A. Roberson of ARL, who guided this program from its inception and passed away shortly before the work was completed. They wish to thank Drs. D. Clausing and H. Lipsitt for stimulating discussions. They are indebted to Drs. T.M.F. Ronald and D. P. Voss for making available experimental material and unpublished measurements. They also wish to thank Messrs. D. Osborne, C. Price, and G. Wheeler for assistance with scanning microscopy, and Ms. C. Pepper for her work on the manuscript.

## SUMMARY

The microstructure, second phases, and micromechanisms contributing to fracture toughness are examined. The study focuses on high strength alloys and the component of toughness arising from strain localization and shear rupture, which is shown to be related to  $\bar{\epsilon}_{PS}$ , the "plane strain" ductility. Methods of measuring  $\bar{\epsilon}_{PS}$  are examined, and a new double-bend method which can be applied to both plate and sheet coupons is devised. Successive replication of the bend specimen surface is used to follow the progressive development of particular slipping regions and cracks under "plane strain" biaxial loading.

The  $\bar{\epsilon}_{PS}$ -values of AISI 4340 steel, the 250-grade and 300-grade maraging steel, the Ti-6Al-4V alloy, and the 7075 aluminum alloy in the form of plate and sheet, and a higher purity 7000-type aluminum alloy were measured in a variety of heat treated conditions and, in one case, as a function of specimen orientation. The distribution of the size of slip offsets was also measured at different strains. All of the alloys display a tendency for a coordinated slipping of neighboring grains under "plane strain" flow, thereby setting the stage for an instability involving (a) the formation of coplanar arrays of slip bands or sliding grain boundaries called "superbands", (b) the growth of superbands which can accommodate large shears, (c) initiation of shear microcracks within the bands, and (d) the linking of the cracks into a macrocrack. The work shows that the degree with which  $\bar{\epsilon}_{PS}$ -values correlate with  $K_{Ic}$  varies directly with contribution of the localization-shear rupture mode of separation relative to the void nucleation and growth mode. The strain localization is attributed to a relative softness or softening on the part of the slipping region compared to the more lightly deformed matrix. The susceptibility to strain localization and shear rupture is traced to a number of microstructural elements including (a) fine, coherent precipitate particles cut by dislocations, (b) inclusions, and (c) the grain size and character of the grain boundaries.

## TABLE OF CONTENTS

SECTION	PAGE
I      INTRODUCTION . . . . .	1
II     EXPERIMENTAL PROCEDURE . . . . .	10
III    EXPERIMENTAL RESULTS . . . . .	22
IV    DISCUSSION . . . . .	91
V    CONCLUSIONS . . . . .	100
REFERENCES . . . . .	104
APPENDIX    MEASUREMENT OF SLIP OFFSET DISTRIBUTION . . . . .	107

## LIST OF TABLES

Table 1.    Composition of Alloys . . . . .	11
Table 2.    Influence of Surface Preparation and Specimen Width on the "Plain Strain Ductility" of 7075-T6 Aluminum as Measured With a "Double-Bend" Specimen . . . . .	18
Table 3.    Ordinary Tensile Properties, Plane Strain Ductility and Fracture Toughness Values for 7075 Aluminum Sheet . . . . .	63
Table 4.    Fracture Toughness and "Plane Strain" Ductility Values for 7075 Al Plate in the Peak Aged Condition . . . . .	64

## LIST OF FIGURES

Figure 1.   Comparison of Toughness Values Displayed by 2000 and 7000 Series Aluminum Alloys According with 2 Hypothetical Toughness Requirements . . . . .	2
Figure 2.   Influence of the Volume Fraction of Large Second Phase Particles on the Plane Strain Fracture Toughness of Commercial Alloys . . . . .	4

LIST OF FIGURES (Continued)

	<b>PAGE</b>
Figure 3. Schematic Representation of a Plastic Instability at the Crack Tip . . . . .	5
Figure 4. Schematic Representation of "Plane Strain Deformation . .	7
Figure 5. Test Piece Dimensions . . . . .	12
Figure 6. Simple Three-Point Bending Fixture . . . . .	14
Figure 7. Example of 100 $\mu\text{m}$ -Grid Produced by Vapor Depositing Copper into the Top Surface of a Bend Specimen . . . . .	15
Figure 8. Example of the Longitudinal (True) Strain, Distribution on the Surface of a 7075-T6 Aluminum Double-Bend Specimen . . . . .	17
Figure 9. Variation of the Principal Tensile (Longitudinal) Strain Along Tension Axis of a Clausing "Plane Strain" Tension Specimen . . . . .	20
Figure 10. Schematic Representation of the Deformation of the Clausing "Plane Strain" Tension Specimen Cross Section. .	21
Figure 11. Variation of Ductility and Toughness of 4340 Steel with Tempering Temperature . . . . .	23
Figure 12. Influence of State of Strain on the Distribution of Deformation on the Surface of AISI 4340 Steel . . . . .	25
Figure 13. Defroamtion Bands on the Surface of Quenched and Tempered 4340 Steel Bend Coupons . . . . .	26
Figure 14. Profiles of Super Bands Near the 232°C Tempered 4340 Steel Bend Specimens . . . . .	27
Figure 15. Deformation Bands on the Surface of A 204°C Tempered 4340 Steel Bend Coupon . . . . .	28
Figure 16. Scanning Electron Micrographs of Cracked Superbands on the Surface of Plastically Bent 4340 Steel Strips in the Vicinity of the Fracture . . . . .	30
Figure 17. SEM Stereo Pairs of Cracked Superbands on the Surface of 538°C Tempered 4340 Steel Bend Specimens . . . . .	31
Figure 18. Examples of Deformation Bands on the Surface of A 204°C Tempered 4340 Steel Bend Coupon . . . . .	33

LIST OF FIGURES (Continued)

	<b>PAGE</b>
Figure 19. Formation of a Superband at a Ruptured Inclusion on the Surface of 204°C Tempered 4340 Steel Bend Coupon . . . . .	34
Figure 20. Deformation Bands on the Surface of a 538°C Tempered 4340 Steel Bend Coupon . . . . .	35
Figure 21. Formation of Superbands and Cracks by Ruptured Inclusions on the Surface of A 538°C Tempered 4340 Steel Bend Coupon . . . . .	37
Figure 22. Slip Markings on the Surface of 538°C Tempered A157 4340 Steel Bend Specimens . . . . .	40
Figure 23. Slip Offsets on the Surface of 538°C Tempered AISI 4340 Steel Bend Specimens . . . . .	41
Figure 24. SEM Stereo Pair of a Cracked Slip Band on the Surface of a 204°C Tempered 4340 Steel Bend Specimen . . . . .	42
Figure 25. Cracks at the Base of Large Slip Offsets on the Surface 538°C Tempered AISI 4340 Steel Bend Specimens . . . . .	43
Figure 26. Distribution of Slip Offsets on Electron Micrographs of 4340 Steel Tempered at Different Temperatures . . . . .	44
Figure 27. Distribution of Slip Offsets on Electron Micrographs of 4340 Steel Plane Strain (Double) Bend Specimens at the Onset of Fracture . . . . .	45
Figure 28. Mechanical Properties of Maraging Steels . . . . .	46
Figure 29. Comparison of the Deformation Bands on the Surface of 250-Grade and 300-Grade Maraging Steel and 4340 Steel Bend Specimens . . . . .	48
Figure 30. Appearance of Superbands on the Surface of 250-Grade Maraging Steel "Plane-Strain" (Double) Bend Specimen . . .	49
Figure 31. Example of a Cracked Superband on the Surface of 250-Grade Maraging Steel "Plane Strain" (Double-Bend Specimen) . . .	50
Figure 32. Scanning Electron Micrographs of Surface of 250-Grade Maraging Steel Plane Strain (Double) Bend Specimen . . .	51
Figure 33. Slip Markings on the Surface of 300-Grade Maraging Steel in the Peak-Aged Conditions Showing Slip Bands and Grain Boundary Offsets . . . . .	52

LIST OF FIGURES (Continued)

	PAGE
Figure 34. Distribution of Slip Offsets on Electron Micrographs of 250-Grade Maraging Steel, "Plane Strain" Double Bend Specimens at the Onset of Fracture . . . . .	53
Figure 35. Measurements of Slip Band Offsets on the Surface of Two High Strength Steels . . . . .	54
Figure 36. Deformation Markings on the Surface of the Aged Ti-6Al-4V Bend Specimen . . . . .	56
Figure 37. SEM Micrographs of the Ti-6Al-4V Bend Specimen Surface .	58
Figure 38. Slip Markings on the Surface of Aged Ti-6Al-4V Bend Specimens . . . . .	59
Figure 39. Transmission Micrographs of Cellulose Acetate Replicas of the Surface of Aged Ti-6Al-4V Bend Specimens . .	60
Figure 40. Influence of Aging on the Yield Strength, Fracture Toughness, Conventional and "Plane Strain" Ductility Values for 7000-Series Aluminum Alloys . . . . .	61
Figure 41. Orientation of "Plane Strain" Double-Bend Specimens Cut From the 7075-Aluminum Alloy Plate . . . . .	65
Figure 42. Scanning in Electron Micrographs of "Plane Strain" Deformation Observed on the Surface of a Plastically Bent Strip of Aluminum Alloy X in the Peak Aged Condition	66
Figure 43. Deformation Markings on the Surface of Aluminum Alloy X "Plane Strain" Bend Specimens in the Aged Condition . .	67
Figure 44. Close-Up of the Development of a Superband on the Surface of an Aluminum Alloy X Bend Specimen in the Peak Aged Condition . . . . .	69
Figure 45. Deformation Markings on the Surface of Aluminum Alloy X "Plane Strain" Bend Specimens in the As-Solution Treated	72
Figure 46. Deformation Markings on the Surface of Overaged Alloy X "Plane-Strain" Double-Bend Specimen . . . . .	73
Figure 47. Optical Micrographs of the Surface of a Plane Strain Bend Specimen of a 7000-Series Aluminum Alloy In the Overaged Condition . . . . .	74

LIST OF FIGURES (Continued)

	PAGE
Figure 48. Influence of Heat Treatment on the Plastic Strain Distribution on the Microscale for "Plane Strain" Deformation . . . . .	75
Figure 49. Slip Steps on the Surface of the Aged Alloy X-Bend Specimens . . . . .	77
Figure 50. Large Slip Offsets on the Surface of Aged Alloy X Bend Specimens . . . . .	78
Figure 51. Examples of Coarse Slip Bands . . . . .	79
Figure 52. Micrographs of the Surface of 7075-Aluminum Alloy Sheet "Plane-Strain" Double-Bend Specimens . . . . .	80
Figure 53. Micrographs of the Surface of 7075-Aluminum Alloy Plate "Plane-Strain" Double-Bend Specimens . . . . .	84
Figure 54. Large Slip Offsets on the Surface of Fracture 7075-Alloy Plate LS-Orientation Bend Specimens . . . . .	88
Figure A-1. Schematic Representation of Slip Band Offset on Metal and on the Plastic Replica . . . . .	A-2
Figure A-2. Distribution of Slip Offsets on Electron Micrograph Replicas of 4340 Steel . . . . .	A-4

## SECTION I

### INTRODUCTION

The toughness levels of metals generally decrease as the strength level is raised by alloying and heat treatment. This trend is illustrated in Figure 1 for aluminum alloys. At the same time, the minimum fracture toughness requirements become more stringent as the yield strength is raised (see Figure 1, caption). The intersection of these two trends defines a yield strength ceiling beyond which fracture safe operation cannot be assured. For service involving extensive fatigue or the stress corrosion type of stable crack growth (Requirement 2 in Figure 1), a maximum yield strength of roughly  $\sigma_y \sim 350 \text{ MNm}^{-2}$  ( $\sim 50 \text{ ksi}$ ) is indicated for the aluminum alloys in Figure 1. Corresponding values are  $\sigma_y \sim 830 \text{ MNm}^{-2}$  ( $\sim 120 \text{ ksi}$ ) for titanium alloys, and at  $\sigma_y \sim 1250 \text{ MNm}^{-2}$  ( $\sim 180 \text{ ksi}$ ) for steels.<sup>(2)</sup> The utilization of higher strength levels and attendant opportunities for increased structural efficiency depend on improving the fracture toughness or the crack detection practice.

This report describes a study aimed at identifying the metallurgical factors that underly the loss of toughness at high strength levels. Crack extension in these materials usually proceeds by the "ductile" or "fibrous" mode with its characteristic "dimples". The failure process involves<sup>(3,4)</sup>

- (i) slip induced fracture of hard particles or inclusions either by cleavage or by separation of the particle matrix interface,
- (ii) the growth of the voids produced by these failures, and
- (iii) the linking up of voids and their joining with the main crack front.

Beginning with Krafft<sup>(5)</sup>, various attempts have been made to formulate the process of hole growth and linking up in the plastically strained region surrounding the crack tip, including detailed continuum elastic-plastic analyses by McClintock,<sup>(6)</sup> Thomasson<sup>(7)</sup>, and Rice and Johnson<sup>(8)</sup>. A highly simplified view of the contribution

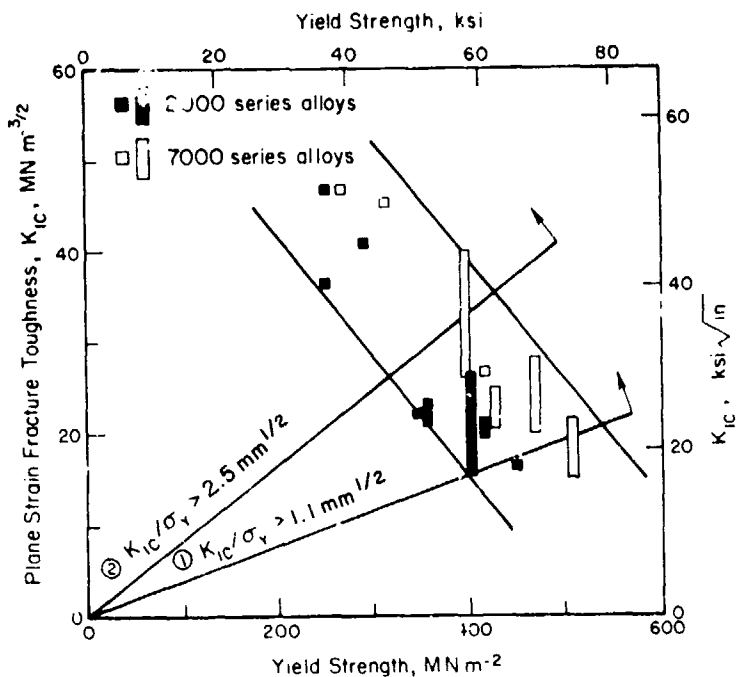


FIGURE 1. COMPARISON OF TOUGHNESS VALUES DISPLAYED BY 2000 and 7000 SERIES ALUMINUM ALLOYS ACCORDING TO DEVELAY(1) WITH 2 HYPOTHETICAL TOUGHNESS REQUIREMENTS. Requirement 1. No stable crack growth:

$a^* = a_0$ , and  $\frac{K_{Ic}}{\sigma_y} \geq 0.036 \text{ m}^{1/2}$ . This requirement is appropriate when the component is not exposed to cyclic loading or environments that produce stable crack growth. Requirement 2. Extensive stable crack growth:  $a^* = 5a_0$  and  $\frac{K_{Ic}}{\sigma_y} \geq 0.08 \text{ m}^{1/2}$ . This requirement is appropriate when cyclic loading and/or stress corrosion produce a 5-fold increase in the natural flaw size during the service life. The 2 requirements are derived in the footnote on page 3.

ligaments which limit the extent of the highly strained region that can be generated at the crack tip<sup>(8)</sup>. This concept defines the relation between  $K_{Ic}$  and the  $f_c$ , the volume fraction of cracked particles<sup>(9)</sup>:

$$K_{Ic} \approx \left[ 2\sigma_Y E \cdot \frac{\pi}{6} \right]^{1/3} f_c^{-1/6} \quad (1)$$

where  $\sigma_Y$  is the yield stress,  $E$  is the elastic modulus, and  $D$  is the particle diameter. Figure 2 shows that the negative 1/6-power dependence on volume fraction is indeed obtained. However, large differences in toughness which correlate with strength level are observed at the same volume fraction.

The loss of toughness with increasing strength level, which is illustrated in Figures 1 and 2, is associated with strain localizing instabilities within the region of large plastic strain along the line proposed by McClintock, et al<sup>(16)</sup>, Berg<sup>(17)</sup>, and Griffis and Spretnak<sup>(18)</sup>. Figure 3 illustrates the concept schematically: The instabilities tend to confine shear into narrow bands and, by intensifying strain locally, accelerate the linking of voids. Additional evidence of the contribution of localized shear to the linking up process has been reported by Cox and Low<sup>(14)</sup>. These workers find that voids in the 4340 steel link together before they coalesce when the total void volume represents as little as 3%-9% of the total cross section. The voids are linked by shear failures of the intervening material (91%-97% of the cross section) which occur along shear bands connecting the voids, a phenomenon analogous to the "void sheet" formation of Rogers<sup>(19)</sup> and the "slip

---

Footnote to Figure 1 caption.

The toughness requirement for a particular component depends on the sensitivity of the flaw detection procedures, as well as on the safety factor (the ratio  $\sigma/\sigma_Y$ , the design stress to the yield stress), or the cyclic load and environmental histories, and on the size and geometry of the part. At the present time, good NDI practices can reliably detect surface cracks  $2a_0 \geq 1.27$  mm-long (0.05 in.-long). The ratio  $\sigma/\sigma_Y = 0.8$  is frequently used in aircraft design. For the case of a deep surface flaw oriented normal to the stress axis  $K_{Ic} = \sigma \sqrt{\pi a^*}$ , where  $a^*$  is the critical flaw size. The toughness requirement then takes the form  $K_{Ic} \geq 0.8 \sigma_Y \sqrt{(0.64 \text{ mm}) \cdot \pi a^*/a_0}$ .

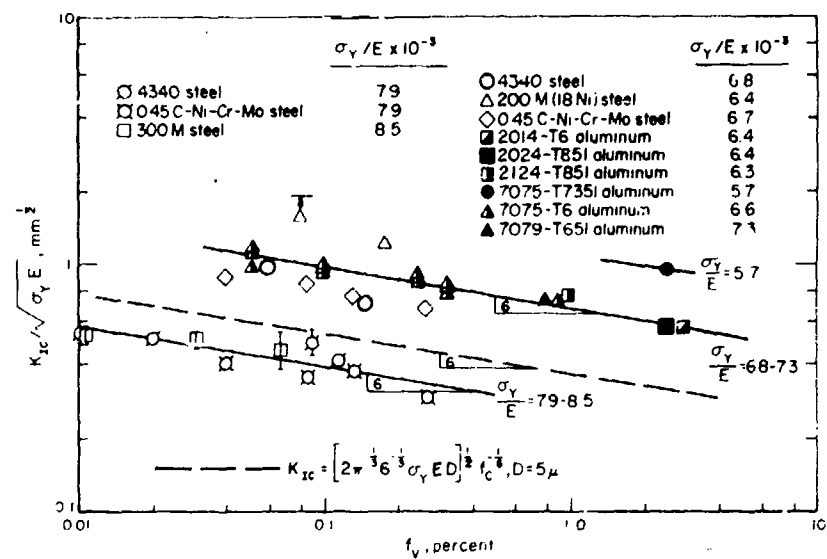


FIGURE 2. INFLUENCE OF THE VOLUME FRACTION OF LARGE ( $\sim 1\mu$  SIZE) SECOND PHASE PARTICLES ON THE PLANE STRAIN FRACTURE TOUGHNESS OF COMMERCIAL ALLOYS AFTER BIRKLE, ET AL (10), HAUSER AND WELLS (11), LOW AND COWORKERS (12-14), AND MULHERIN AND ROSENTHAL (15)

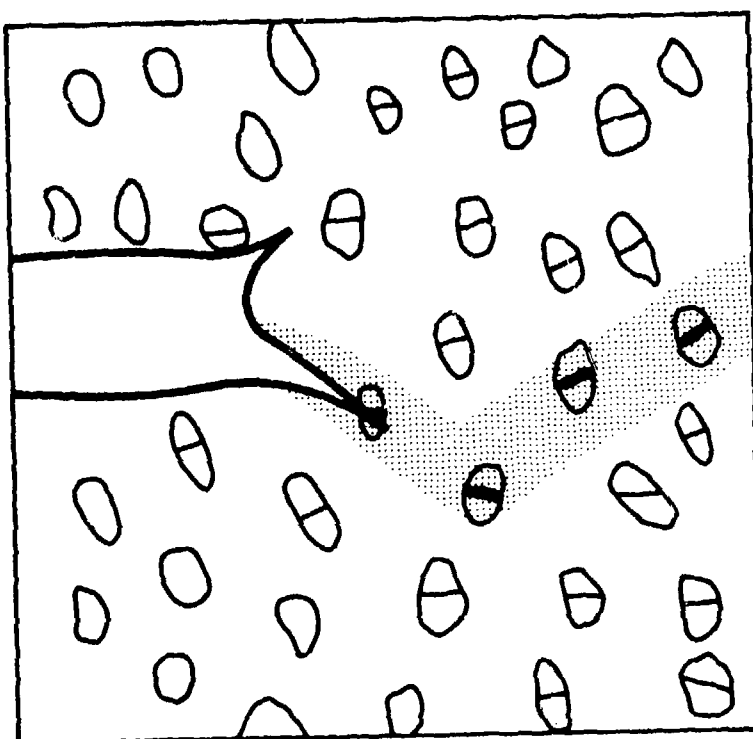


FIGURE 3. SCHEMATIC REPRESENTATION OF A PLASTIC INSTABILITY AT THE CRACK TIP. THE SHADED BAND REPRESENTS A SHEAR STRAIN CONCENTRATION WITHIN THE REGION OF LARGE STRAIN ADJACENT TO THE CRACK TIP AFTER BERG(17)

decohesion" of Griffis and Spretnak<sup>(18)</sup>. These shear failures were not observed in the 200 grade 18 Ni-maraging grade which is tougher (see Figure 2). This steel ruptures only after the voids have grown and occupy 100% of the cross section, i.e., after they impinge and coalesce.

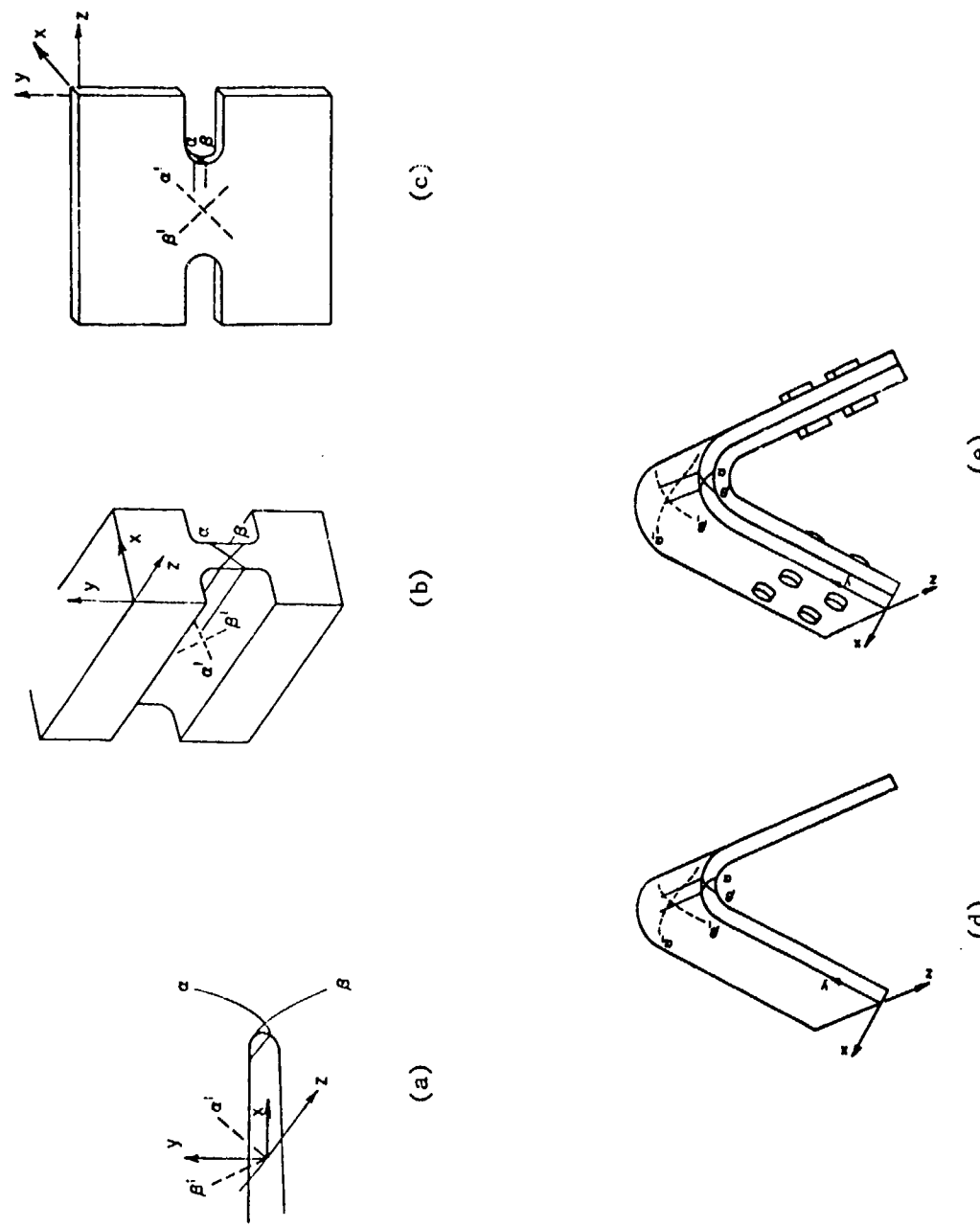
The nature of the instability has become more understandable in the light of recent studies by Clausing<sup>(20,21)</sup>, and Mohamed and Tetelman<sup>(22)</sup>, and McGarry<sup>(23)</sup>. Clausing studied the ductility of a number of alloys in the form of "plane strain" tensile specimens (Figure 4b). The gage section of this test piece is subjected to unbalanced biaxial tension and "plane strain" like the state of stress and strain at the root of a crack (Figure 4a). In both cases, slip displacements are confined to the xy plane (hence, the term "plane strain") along the characteristics  $\alpha$ ,  $\beta$ ; flow in the yz plane along  $\alpha'$ ,  $\beta'$  is in both cases constrained. Similar patterns of deformation are produced in the center of the notched sheet coupon (Figure 4c) and on the tension side of a wide, plastically bent strips; the displacements parallel to the surface along  $\alpha'$ ,  $\beta'$  are constrained by the large plastic strain gradient in the thickness direction.<sup>†</sup>

Clausing measured the plane strain ductility (true fracture strain displayed by the "plane strain" tensile specimen) of seven different steels covering a wide range of strength levels. The plane strain ductility decreases more rapidly with strength level than the ductility of ordinary round test pieces. He also demonstrated that the slow bend, V-notch Charpy energy values for these steels are consistent with the

---

<sup>†</sup> "Plane strain" biaxial loading is produced when plastic deformation in one of the principal directions is constrained as in the "plane strain" tension, bend, and sheet coupons illustrated in Figure 4b-e. These produce a state of unbalanced biaxial tension and "plane strain",  $\sigma_1 = 1/2 \sigma_2$ ,  $\sigma_3 = 0$ ;  $\epsilon_1 = -\epsilon_3$ ,  $\epsilon_2 = 0$ , analogous to the state of stress at the root of a notch or crack (see Figure 4a). They do not reproduce the high triaxial stress state characteristic of the plastic zone of a notch or crack at distance  $\gtrsim 2$  foot radii from the crack tip. For this reason "plane strain" is written with quotation marks.

FIGURE 4. SCHEMATIC REPRESENTATION OF "PLANE STRAIN" DEFORMATION: (a) at the tip of a crack, (b) in the Clausing "plane strain" tensile specimen, (c) in a "plane strain" sheet coupon, (d) in a plastically bent strip, and (e) in the double-bend coupon



idea that fractures initiate when the plane strain ductility is exceeded at the notch root. In a similar vein, Mohamed and Tetelman<sup>(22)</sup> find that the peak strain required for fracture initiation at the root of a Charpy specimen is independent of root radius and decreases with yield strength level. Their strain values display the same trend with strength level as Clausing's plane strain ductility, and appear to be quite similar in magnitude to Clausing's when averaging effects are taken into account<sup>(24)</sup>. Similar results have been obtained by McGarry<sup>(23)</sup>. A correlation between  $K_c$ -values and the "biaxial" ductility has also been reported by Weiss and Sengupta<sup>(25)</sup>.

The implications of these findings is that the "plane strain" deformation, even in the absence of triaxiality, simulates the events responsible for crack extension at the root of a crack. Clausing<sup>(20)</sup> has examined the microscopic distribution of slip in plane-strain tensile specimens of a number of steels and finds that "plane strain" plastic flow is different from that observed in axisymmetrically strained bars. The main differences are that in plane strain, deformation tends to be confined to groupings of slip bands--referred to here as "super bands" which are aligned parallel to the zero strain axis (the traces of  $\alpha$  and  $\beta$  slip systems on the  $yz$ -plane in Figure 4b). The resulting strain concentrations within the superbands lead to the formation of shear cracks and fracture at smaller values of the nominal strain than under axisymmetric conditions where the failure initiates in the interior of the test piece.

The general aim of this program was to identify the contribution of microstructure and second phases to the fracture toughness. Emphasis was placed on high strength alloys and the structural elements affecting strain localization and shear rupture. The work sought to exploit the concepts reviewed in this section by establishing the connection between  $K_{Ic}$  and  $\bar{\epsilon}_{PS}$  (the "plane strain" ductility). This made it possible to equate the events observed on the surfaces of "plane strain"

bend specimens with the micromechanisms of slip and rupture at the tip of a crack. To facilitate the metallographic studies a new, more convenient method for measuring  $\bar{\epsilon}_{ps}$ -values which can be applied to both thin sheets and plates was devised. The  $\bar{\epsilon}_{ps}$ -values of AISI 4340 steel, the 250- and 300-grade maraging steel, the Ti-6Al-4V alloy, the 7075-aluminum alloy in the form of sheet and plate, and a higher purity 7000-type aluminum alloy were measured in a variety of heat-treated conditions. These measurements were accompanied by detailed metallographic studies of the mechanisms of slip and rupture on the surfaces of the "plane-strain" bend specimens. The distribution of slip offsets was measured. The research identifies the fine precipitate particles, inclusion particles, grain boundaries, and grain size as the microstructural elements making major contributions to the strain localization-shear rupture mode of crack extension.

## SECTION II

### EXPERIMENTAL PROCEDURE

The high strength alloys used in this study are identified in Table 1. In addition to ordinary tensile specimens, 4 different types of "plane strain" test pieces were employed, (1) the Clausing plane-strain tension specimen (Figure 4b), (2) a wide bend coupon (Figure 4d), (3) an edge-notched "plane strain" sheet coupon (Figure 4c), and (4) a wide double-bend coupon which consists of two ordinary bend coupons riveted together at their ends (Figure 4e). The dimensions of these test pieces are given in Figure 5. The simple jig used to strain the bend coupons is illustrated in Figure 6.

The initial experiments were carried out with the Clausing "plane strain" tensile specimens and with ordinary bend coupons, but several problems were encountered. The geometric constraints underlying the Clausing test piece lead to a relatively small recessed gage section<sup>†</sup>, which makes it difficult to measure strain and to observe the surface in the microscope. Furthermore, the Clausing configuration cannot be adapted to the study of relatively thin sheets. Thickness measurements with an ordinary micrometer (to establish the strain at failure) proved erratic and unreliable, particularly since these involved reassembling the broken pieces. To overcome this difficulty a  $\sim 100 \mu\text{m}$  orthogonal grid was applied to the gage section of the specimens by vapor depositing copper onto the surface through a fine mesh screen (see Figure 7). While the ordinary bend coupon makes it possible to enforce "plane strain" flow near the surface of a sheet coupon, it does not lend itself to the measurement of the plane strain ductility. This is because cracks on the tensile side are relatively stable since the displacements they produce can be accommodated

---

<sup>†</sup> In order to insure plane strain conditions in the Clausing test piece the length or y-direction dimension of the reduced section (see Figure 4) must be 1/3 to 1/5 the overall width or z-direction dimension, while the thickness or x-direction dimension of the reduced section must be smaller than  $\sim 1/5$  the length of the reduced section to provide even a small uniformly strained region and to accommodate fillets. In other words, a 2 mm initial gage length requires a specimen 3 to 5 cm wide.

TABLE I. COMPOSITION OF ALLOYS

	Al	B	C	Co	Cr	Cu	Fe	H	Mg	Mn	Mo	Ni	O	P	S	Si	Ti	V	Zn	Zr
4340 Steel (a)	-	-	0.42	-	1.3	0.05	bal	-	0.5/0.6	0.5/0.6	0.2/0.3	-	1.0	-	-	0.009	0.3	-	-	
250-Maraging Steel (b)	0.4	<0.003	0.018	8.25	-	-	bal	-	0.01	0.01	4.98	-	18.2	-	-	0.902	0.03	0.3/0.4	-	
300-Maraging Steel (c)	0.15	0.005	0.03	8.52	-	0.05	bal	-	0.06	0.06	4.62	-	18.00	-	-0.003	0.007	0.04	0.68	-	
Ti-6Al-4V (e)	6.6	-	0.05	-	-	0.18	0.0047	-	-	-	0.015	-	0.15	-	-	-	-	4.1	-	
7000-Type Aluminum, (a)	bal	-	-	<0.01	1.43	<0.01	-	2.44	<0.01	-	-	-	-	-	-	<0.01	<0.01	-	5.60	
Alloy X																				
7075 Aluminum Sheet (d)	bal	-	-	-	0.19	1.71	0.22	-	2.74	0.044	-	-	-	-	-	0.26	-	6.05	-	
7075 Aluminum Plate (e)	bal	-	-	0.19	1.9	0.2	-	2.6	-	-	-	-	-	-	-	0.035	-	5.35	-	

(a) 1 in.-thick plate

(b) Plate material

(c) 0.0625 in.-thick sheet

(d) 0.0625 in.-thick plate

(e) 1.375 in.-thick plate

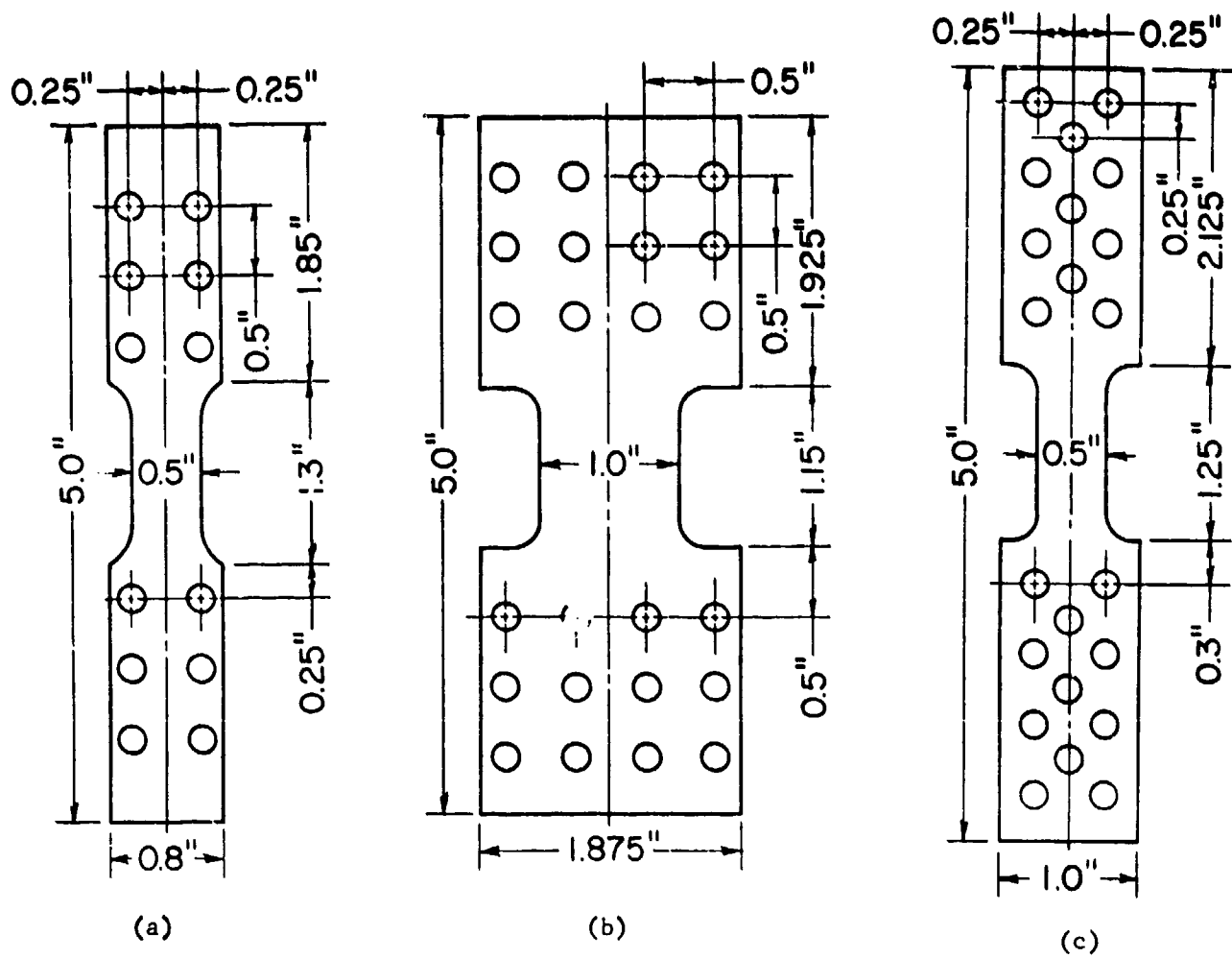
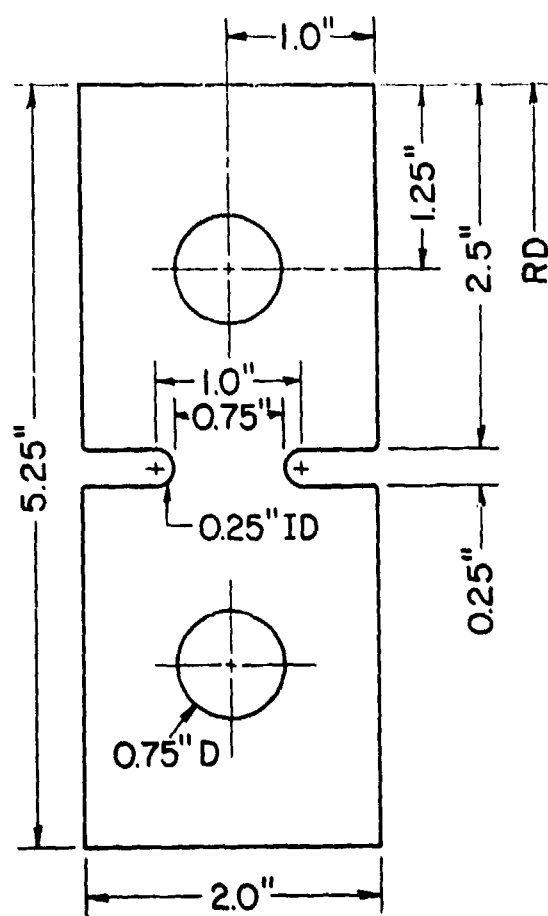
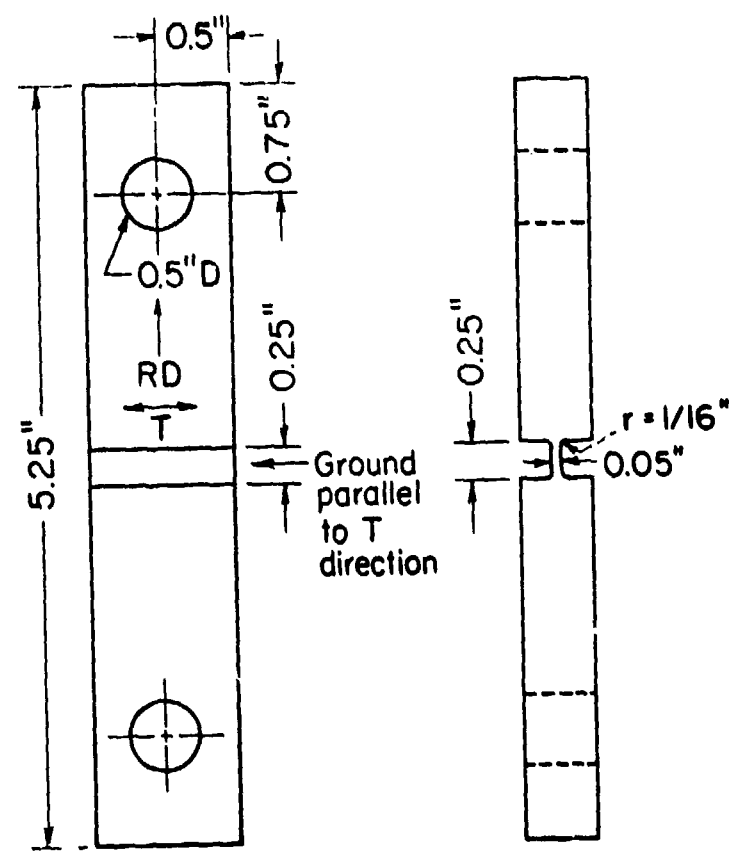


FIGURE 5. TEST PIECE DIMENSIONS: (a), (b) and (c) are double-bend coupons which were machined to a thickness of 0.060 in., (d) "plane strain" sheet coupon, and (e) Clausing plane strain tension specimen. Configuration (c) was used exclusively for the maraging grades



(d)



(e)

FIGURE 5. (Continued)

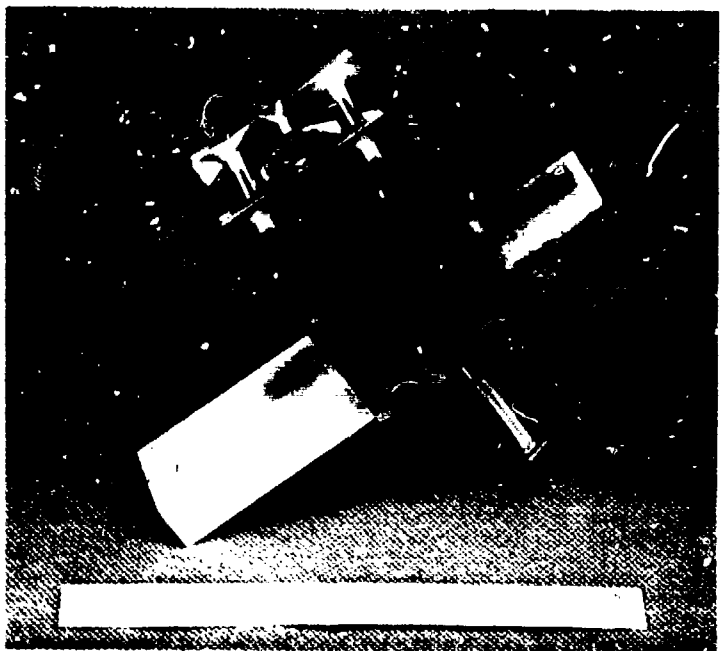


FIGURE 6. SIMPLE THREE-POINT BENDING FIXTURE. The strip specimen is forced against 2 fixed pins and plastically bent by the moveable cross piece in the center. The cross piece, a rectangular plate with a rounded bearing edge, slides in grooves cut in the 2 end plates, and is actuated by the screw in the base. The arrangement facilitates observation of the tension surface of the strip while the specimen is being bent

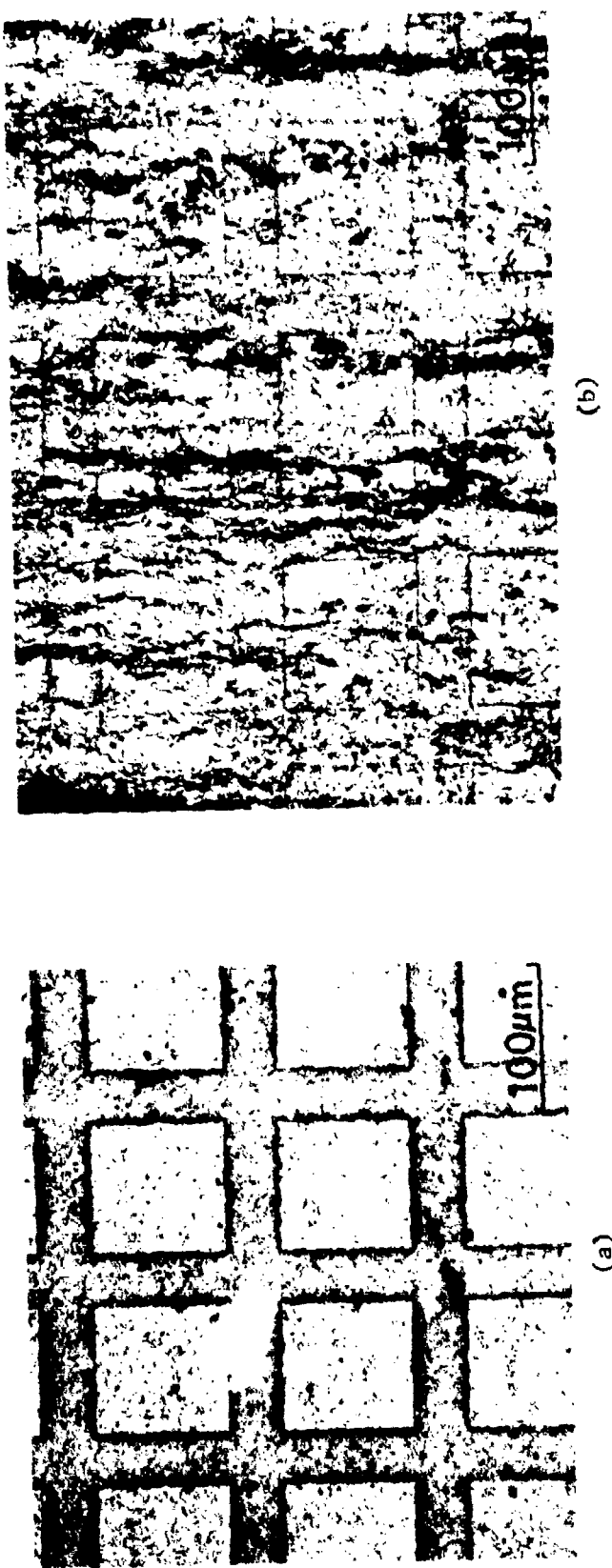


FIGURE 7. EXAMPLE OF  $100 \mu\text{m}$ -GRID PRODUCED BY VAPOR DEPOSITING COPPER INTO THE TOP SURFACE OF A BEND SPECIMEN: (a) before deformation, (b) after bending to failure. The photographs show the surface of a AISI 4340 Steel (double)-bend specimen tempered at  $208^\circ\text{C}$ ;  $\bar{\epsilon}_{\text{PS}} = 0.16$

on the far side of the neutral axis which remains in compression. To overcome this problem, measurements were attempted with the edge notched sheet coupon shown in Figure 4c, which also enforces "plane strain" in the center of the reduced section. However, it was found that the fractures did not initiate in the plane strain region in the center but in the vicinity of the notch root, presumably because of the strain concentrations in these regions.

The "double bend" specimen evolved from the idea of combining bending with tension and thereby restricting flow in the third direction without notches and making surface cracks more unstable. This is accomplished by interfacing two strips and fastening them together at their ends (see Figure 4e). When the double-bend specimen is bent, the strip in tension suffers a net extension and is exposed to a net tension in excess of the yield stress. Figure 8 illustrates the variation of  $\bar{\epsilon}_1$ , the maximum principal (true) tensile strain<sup>†</sup> with distance along the y-axis of a double bend specimen, and shows that the local strain is essentially uniform over a distance of about 2 to 3 mm. Since the intermediate (transverse) strain,  $\bar{\epsilon}_2$ , measured in the z-direction was in all cases less than  $\sim 1\%$ , plane strain conditions are maintained to a close approximation. The results in Table 2 demonstrate that the critical strain values at fracture are relatively insensitive to surface preparation or the presence of vapor deposited copper. Table 2 also illustrates that an increase in the width-to-thickness ratio of the plastically bent strip from 8.3 to 16.6 is attended by a modest 11% decrease in the ductility, presumably connected with a closer approach to the "plane-strain" biaxial loading state<sup>††</sup>. Since the aim of this program was to

<sup>†</sup> The principle (true) tensile strain  $\bar{\epsilon}_1$ , was determined from changes in the grid spacing along the y-axis averaged over 0.1-0.2 mm,  $\bar{\epsilon}_1 = \ln \frac{b_2}{b_1}$ . As shown in Figure 8, the peak value of the strain after fracture was taken as the plane strain ductility,  $\bar{\epsilon}_{1,\max} \equiv \bar{\epsilon}_{PS}$ .

<sup>††</sup> But beyond the resolving power of the strain measuring technique.

7075-T6 Aluminum Double Bend Specimen  
 Width to Thickness Ratio = 8.3  
 As-Rolled Surface  
 $\bar{\epsilon}_2 < 0.01$

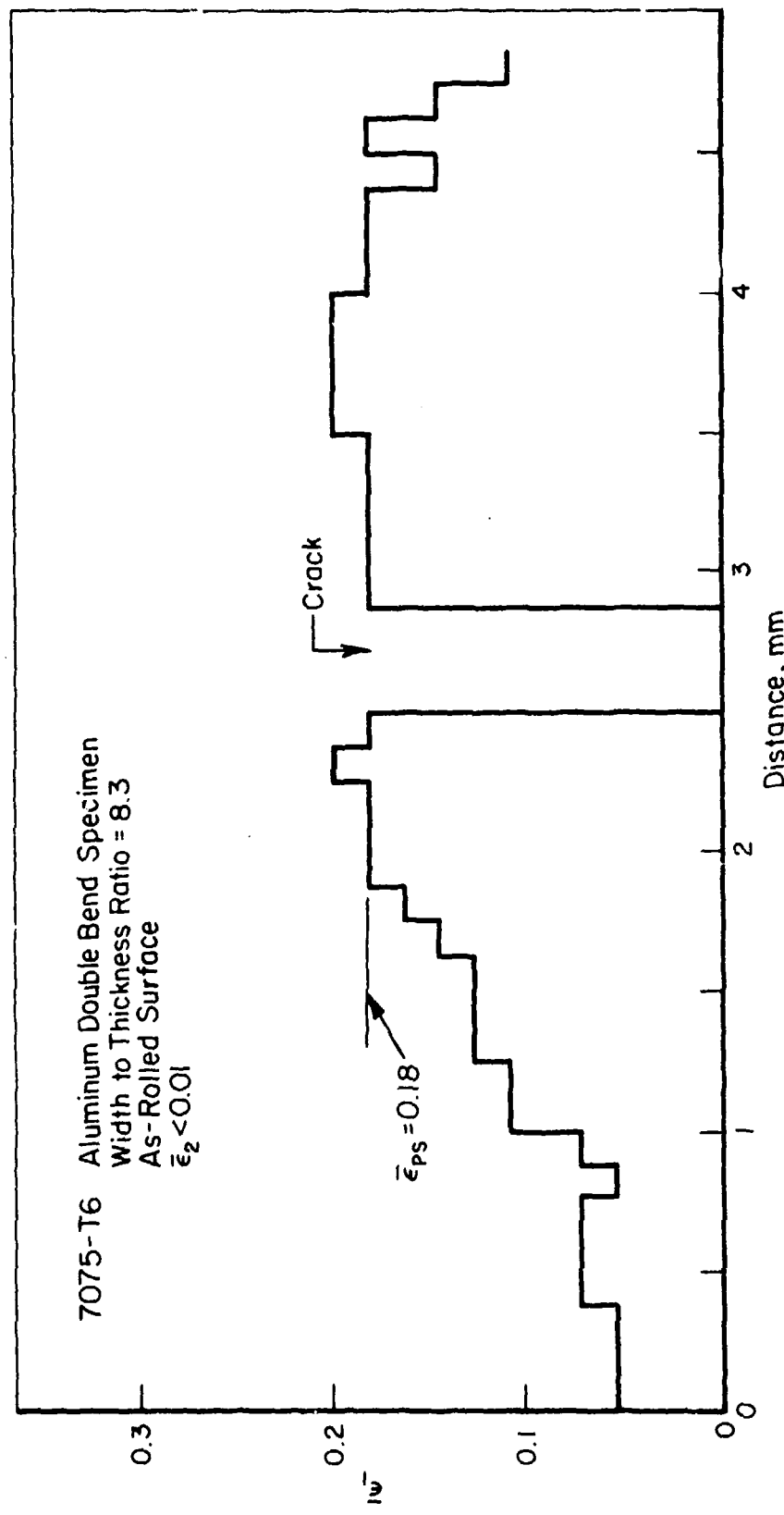


FIGURE 8. EXAMPLE OF THE LONGITUDINAL (TRUE) STRAIN, DISTRIBUTION MEASURED ON THE SURFACE OF A 7075-T6 ALUMINUM DOUBLE-BEND SPECIMEN NEAR THE CENTER OF THE STRIP. The corresponding (true) transverse strains  $\bar{\epsilon}_2 < 0.01$  in all cases

TABLE 2. INFLUENCE OF SURFACE PREPARATION AND SPECIMEN WIDTH ON THE "PLAIN STRAIN DUCTILITY" OF 7075-T6 ALUMINUM AS MEASURED WITH A "DOUBLE-BEND" SPECIMEN<sup>(a)</sup>

Condition	$\bar{\epsilon}_{PS}$ (b)	$\bar{\varphi}_{PS}$ (c)
Specimen A, width/thickness = 8.3		
Electropolished surface	0.18	< 0.01
	0.20	< 0.01
Electropolished surface with vapor deposited copper grid	0.18	< 0.01
	0.18	< 0.01
Handground (600 A grit) surface with copper grid	0.18	< 0.01
	0.18	< 0.01
As-rolled surface with copper grid	0.18	< 0.01
Specimen B, width/thickness = 16.6		
Electropolished surface with vapor deposited copper grid	0.15, 0.17, 0.16	< 0.01

(a) Dimensions of specimens are given in Figure 5.

(b)  $\bar{\epsilon}_{PS}$  - plane strain ductility. This is the value of  $\bar{\epsilon}_1$ , the maximum principle (true) strain at fracture in the long direction of the bent strip, measured in the center of the coupon.

(c)  $\bar{\varphi}_{PS}$  - The value of  $\bar{\epsilon}_2$ , the intermediate principle (true) strain or transverse, z-direction (true) strain at fracture measured in the center of the coupon.

measure the "plane strain" ductility, a width to thickness ratio of 16.6 was employed where practical.

An effort was also made to establish that the "plane strain" ductility measured on the surface of a plastically bent strip corresponds with the ductility of a Clausing plane strain tension specimen. Figure 9 shows the longitudinal strain distribution measured on the surface of the Clausing specimen. The unusual two-peak distribution arises after the onset of necking with the concentration of strain in two intersecting shearing regions, inclined at about  $\sim 45^\circ$  as shown schematically in Figure 10. Figure 9 illustrates that the two-peak longitudinal strain values measured on the surface of the Clausing specimen correspond closely with the peak value measured on the surface of the plastically bent strip (width-to-thickness ratio = 16.6). These peak strain values are larger than the maximum reduction-in-thickness strain value (for the section AA measured at the center of the Clausing test piece in Figure 10) which corresponds with the trough between the two peaks in Figures 9 and 10. This is because the through-the-thickness-strain represents a weighted average of the strain of the two heavily deformed bands and the lightly deformed regions adjacent to them. It should be noted that Clausing's "plane strain" ductility values, which are based on through-the-thickness strain measurements, undervalue the plane strain ductility represented by the maximum longitudinal values of the plane strain tension and bend specimens.<sup>†</sup>

<sup>†</sup> Comparison of plane strain ductility values for AISI 4340 steel at 2 strength levels.

YIELD STRESS MNm <sup>-2</sup>	(Ksi)	DUCTILITY					
		Clausing (a)			This Study (b)		
		$\bar{\epsilon}_{PS}$	$\bar{\epsilon}_{AS}$	$\bar{\epsilon}_{PS}/\bar{\epsilon}_{AS}$	$\bar{\epsilon}_{PS}$	$\bar{\epsilon}_{AS}$	$\bar{\epsilon}_{PS}/\bar{\epsilon}_{AS}$
1123-1157	(163-168)	0.22	0.61	0.36	0.32	0.50	0.64
1460-1474	(212-214)	0.10	0.47	0.21	0.16	0.32	0.50

(a) Based on the maximum thickness reduction  $\bar{\epsilon}_3 = -\ln \frac{t_1}{t_0}$  of "plane strain" tension specimens (20).

(b) Based on the longitudinal strain  $\bar{\epsilon}_1 = \ln \frac{l_1}{l_0}$ , measured on the surface of plastically bent strips.

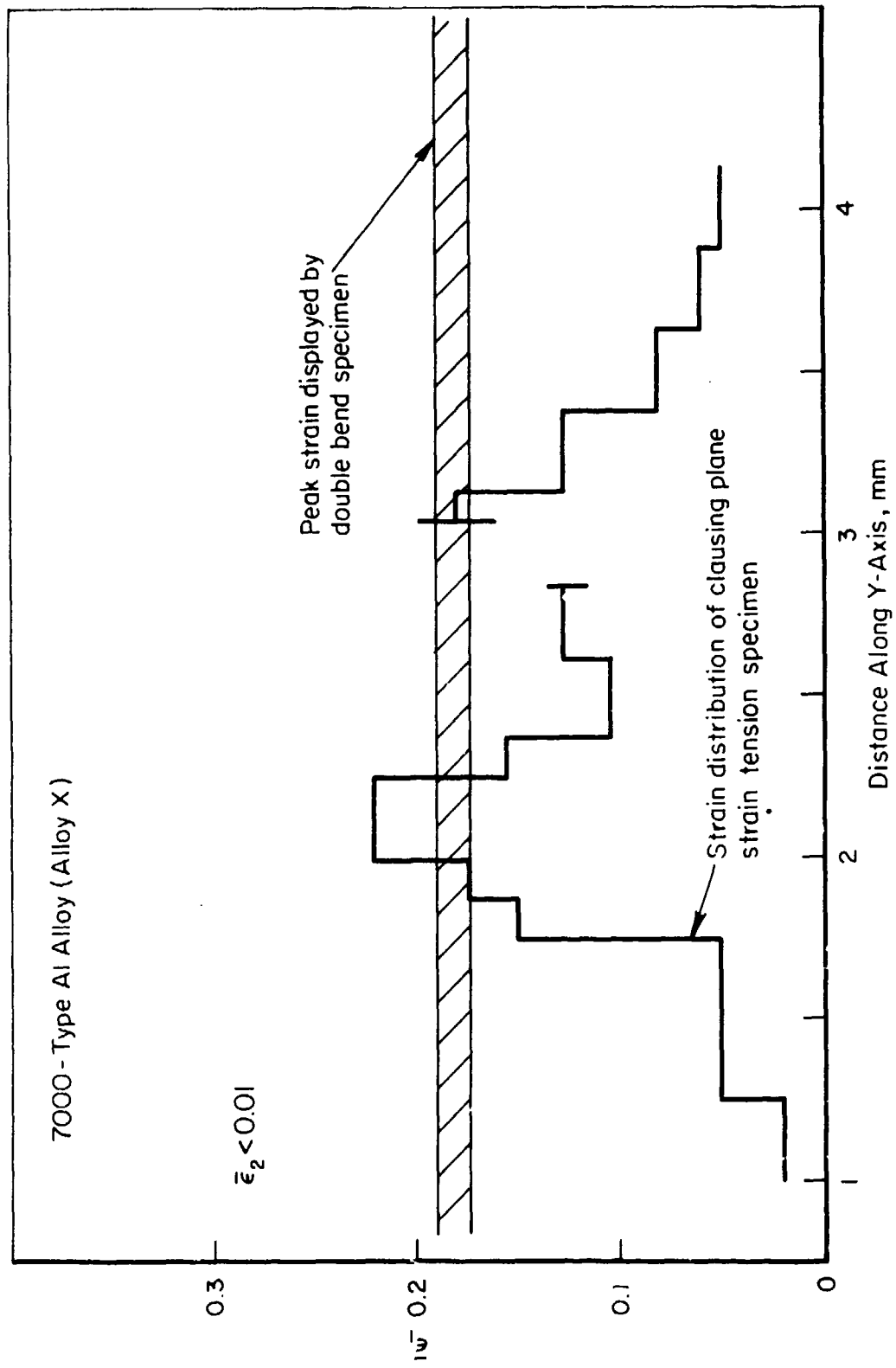


FIGURE 9. VARIATION OF THE PRINCIPAL TENSILE (LONGITUDINAL) STRAIN ALONG TENSION AXIS OF A CLAUSING "PLANE STRAIN" TENSION SPECIMEN (ALLOY X AGED 10 HRS. AT 163°C). The shaded band represents the range of peak strain values displayed by 2 double-bend specimens of the same material.

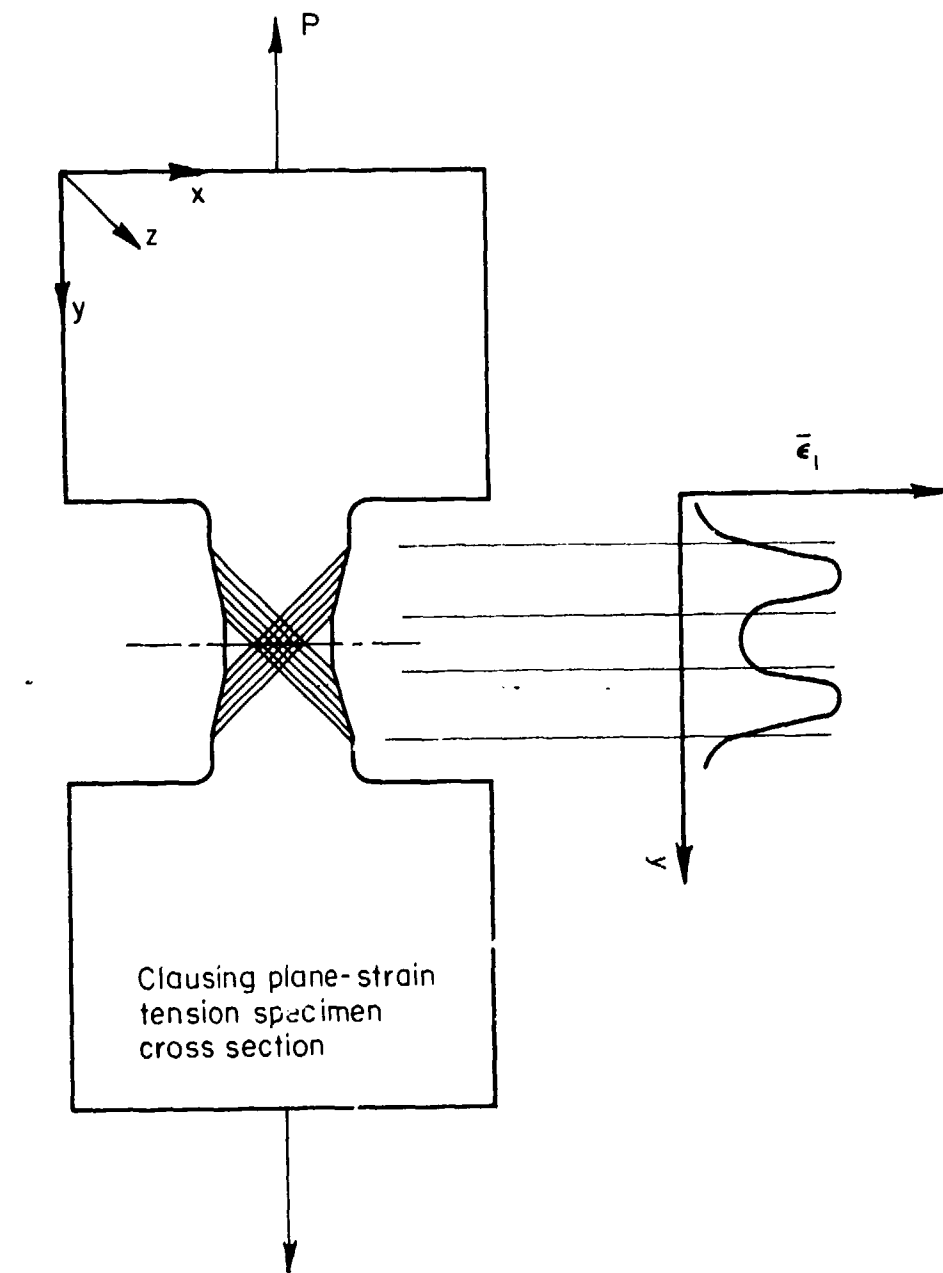


FIGURE 10. SCHEMATIC REPRESENTATION OF THE DEFORMATION OF THE CLAUSING "PLANE STRAIN" TENSION SPECIMEN CROSS SECTION. The 2 peaks in the distribution of longitudinal strain are observed where the two,  $\sim 45^\circ$ -inclined, heavily deformed regions of the neck intersect the surface.

The progressive development of slip markings and cracks on the surface was followed with platinum-carbon-shadowed cellulose acetate replicas which were taken from a prepolished surface at regular strain intervals, without unloading the test specimen. The distribution of strain on the surface of bend coupons was determined from measurements of the vapor deposited grids, or by monitoring the distance between prominent inclusions, grain boundaries, or other microstructural features visible on successive replicas. The size of slip offsets was also measured on replicas by using the simple scheme described in Appendix A.

### SECTION III

#### EXPERIMENTAL RESULTS

##### 1. AISI 4340 STEEL

"Plane strain" ductility values derived from double-bend specimens of the AISI 4340 steel heat treated to different strength levels are presented in Figure 11, together with fracture toughness values for this grade of steel.<sup>†</sup> The two outstanding features of the results are:

- 1) As noted by Clausing<sup>(20,21)</sup>, the "plane strain" ductility is substantially smaller than  $\epsilon_{AS}$ , the conventional fracture strain value displayed by a round tensile bar.
- 2) The decrease in the plane strain ductility with lower tempering temperatures and higher strength levels, correlates with the corresponding decrease in  $K_{Ic}$ -values for this steel. While

<sup>†</sup> Tensile properties of the 4340 grade employed in the present study:

Condition	$\sigma_y$ MNm <sup>-2</sup> (Ksi)	$\sigma_{ULT}$ MNm <sup>-2</sup> (Ksi)	$\epsilon_u$ % <sup>(b)</sup>	El%	RA%
Q and T <sup>(a)</sup> , 1 HR 204°C	1470 (214)	1920 (278)	4.3	7.0	28
Q and T, 1 HR 538°C	1120 (163)	1210 (176)	4.0	9.5	39

(a) Austenitized 45 minutes at 840°C and oil quenched.

(b) Uniform elongation.

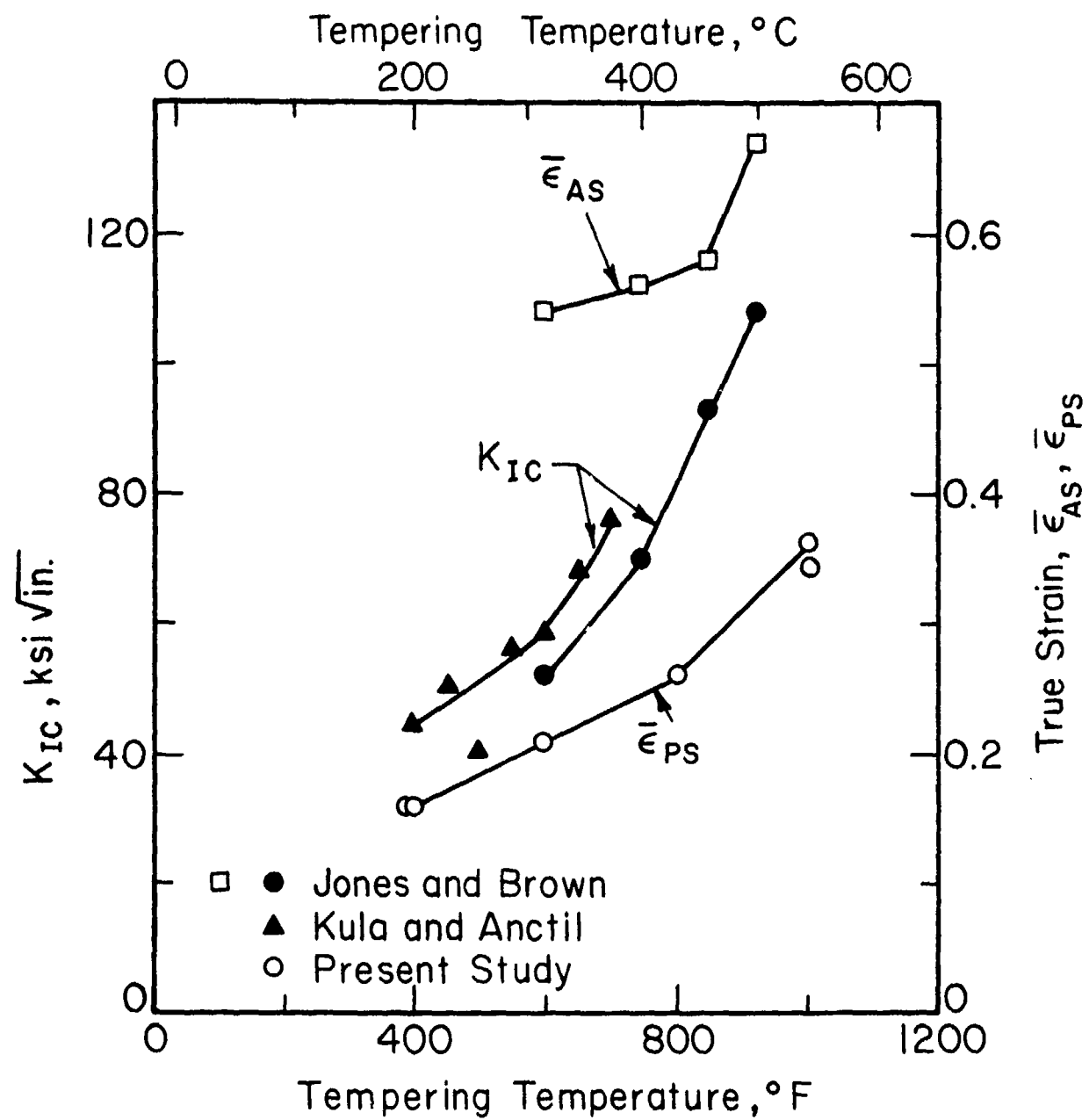
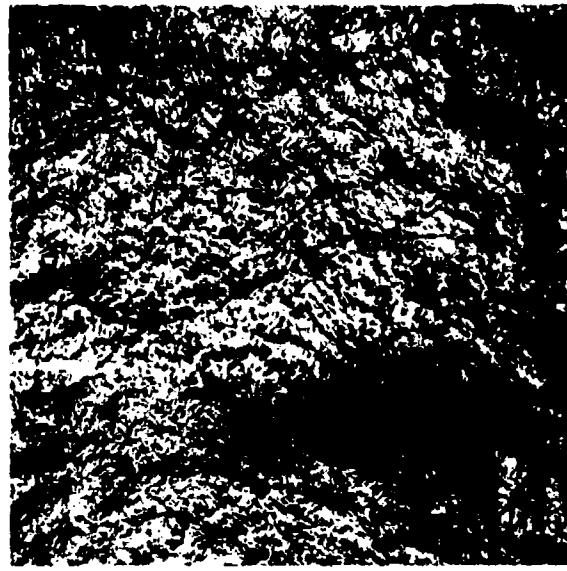


FIGURE 11. VARIATION OF DUCTILITY AND TOUGHNESS OF 4340 STEEL WITH TEMPERING TEMPERATURE. The plane strain ductility  $\bar{\epsilon}_{PS}$  is from the present study;  $K_{Ic}$  and conventional round bar ductility from Jones and Brown<sup>(28)</sup> and Kula and Anctil<sup>(29)</sup>

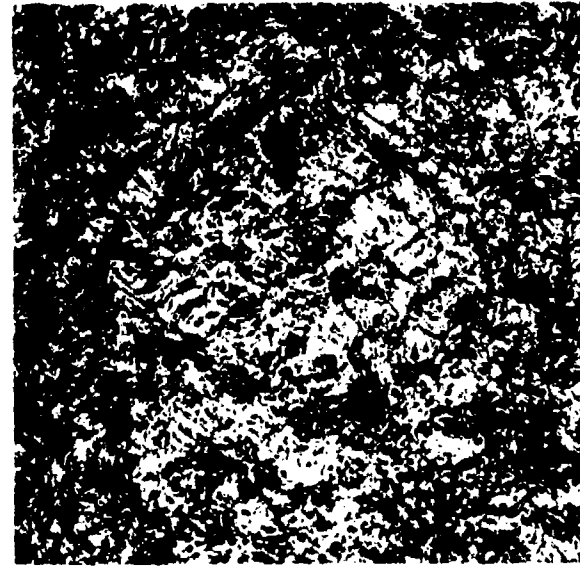
convention ductility values also tend to decrease with lower tempering temperatures, there appears to be a closer correlation between  $\bar{\epsilon}_{PS}$  and  $K_{Ic}$  in this case.

Surface observations of the mechanism of deformation and fracture of the various test pieces (the round bar, "plane strain" tension specimen, and bend specimen) provide an explanation for these results:

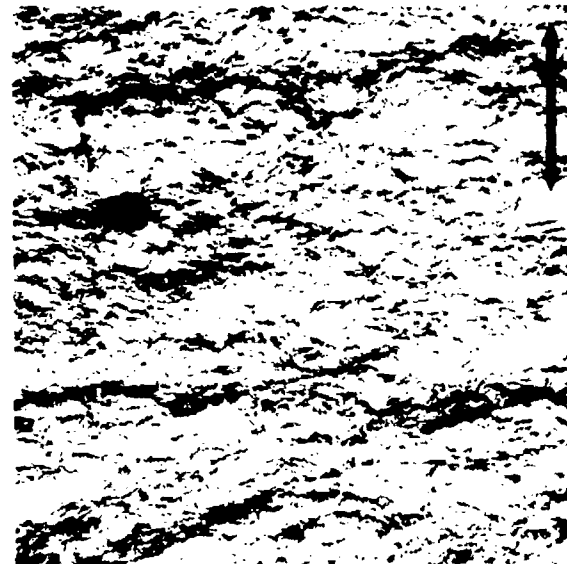
- As shown in Figure 12, slip bands on the surface of conventional round tensile bars are relatively short, limited in size by microstructural boundaries and uniformly distributed. In contrast, slip in Clausing "plane strain" tension specimens and in "plane strain" bend specimens tends to become concentrated in  $\sim 1000 \mu\text{m}$ -long bands. These bands are collections of slip bands with similar orientations, and are referred to as "superbands". The traces of the superbands on the surface are parallel to the zero strain z-axis and correspond with those of the  $\alpha, \beta$  characteristics (see Figure 4). There appear to be no significant differences between the superbands observed on the surface of "plane strain" tension and bend specimens (compare Figures 12 and 13).
- Cracks initiate at the surface within the superbands. As shown in Figure 14, the crack nuclei are inclined at  $\sim 45^\circ$  to the free surface, again consistent with the traces of the  $\alpha, \beta$  characteristics.
- Crack nuclei join and grow in depth within the superbands. The dark lines evident on the surface of the specimen, reproduced in Figure 15 at  $\bar{\epsilon} = 0.10$  and  $0.15$ , are probably cracked superbands which are more easily distinguished in scanning micrographs of Figure 16. The dimples, characteristic of fibrous fracture, are visible on the crack surfaces as shown in Figure 17(a) and (b). One of these cracks ultimately becomes unstable, causing the specimen to break. The outline of the break on the surface corresponds with the outline of a preexisting superband. This was established by comparing the outline of the broken edge with the replica of the superband(s) that existed in that location prior to fracture. As shown in Figure 15(e), the two outlines coincide.



(a)  $\bar{\epsilon} = 0.10$



(b)  $\bar{\epsilon} = 0.20$



(c)  $\bar{\epsilon} = 0.12$



(d)  $\bar{\epsilon} = 0.22$

FIGURE 12. INFLUENCE OF STATE OF STRAIN ON THE DISTRIBUTION OF DEFORMATION ON THE SURFACE OF AISI 4340 STEEL: (a) and (b): axisymmetric (round) tensile bars, (c) and (d) Clausing "plane strain" tension specimens:

- (a) 204°C temper,  $\bar{\epsilon} = 0.10$
- (b) 538°C temper,  $\bar{\epsilon} = 0.20$
- (c) 204°C temper,  $\bar{\epsilon} = 0.12$
- (d) 538°C temper,  $\bar{\epsilon} = 0.22$

Arrows identify principle strain direction

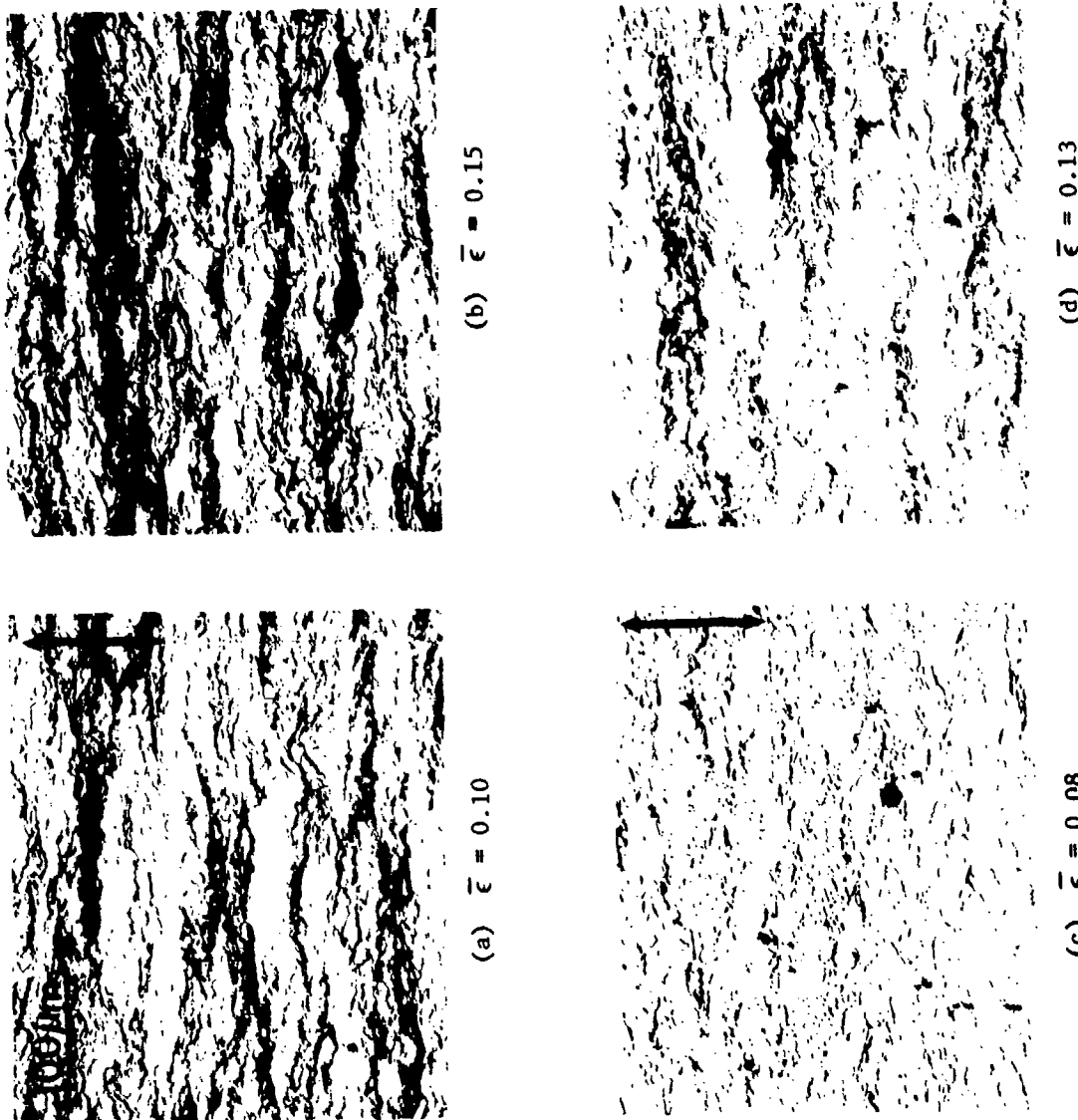


FIGURE 13. DEFORMATION BANDS ON THE SURFACE OF QUENCHED AND TEMPERED 4340 STEEL BEND COUPONS: (a) and (b) tempered at 204°C, and (c) and (d) tempered at 538°C. These bend coupons simulate the biaxial stress-plane strain state existing near the crack tip in the region of large plastic stretch. The micrographs show that slip tends to be more concentrated and less uniformly distributed in the higher strength 204°C-tempered conditions. Fractures are nucleated by cracks which form within the dark deformation bands

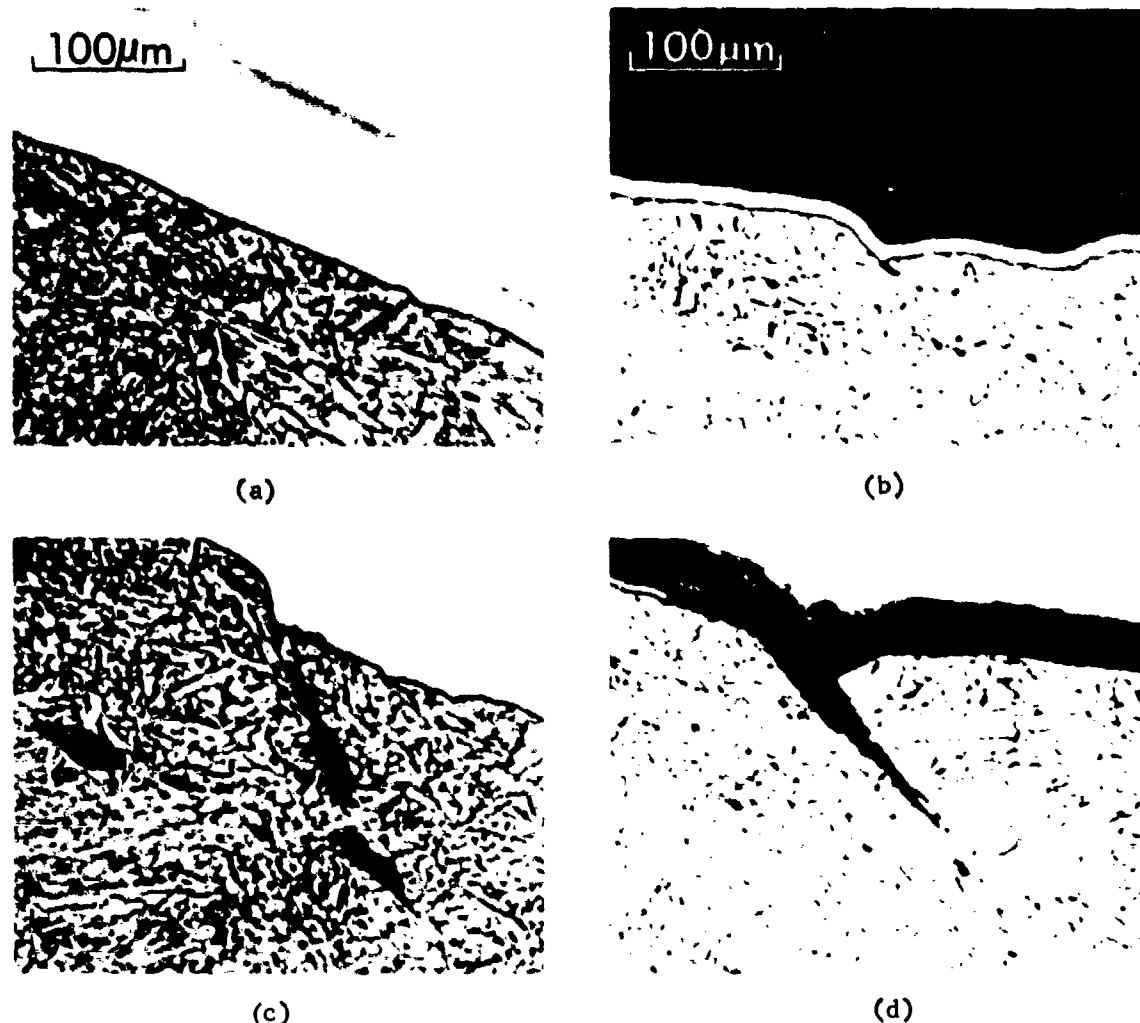
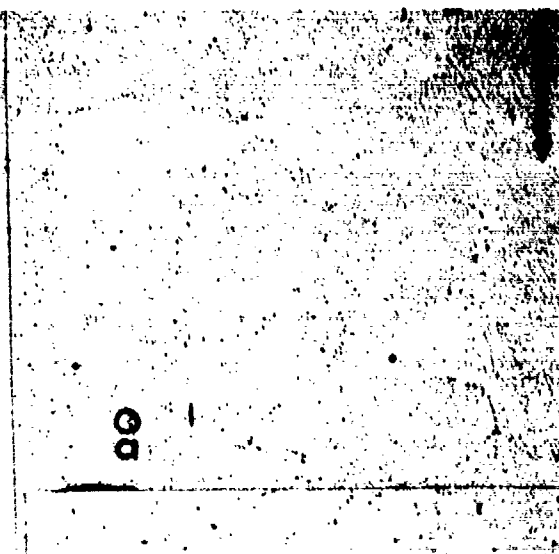


FIGURE 14. PROFILES OF SUPER BANDS NEAR THE 232°C TEMPERED 4340 STEEL BEND SPECIMENS: (a) and (b) show surface steps arising from slip bands inclined to the surface; (c) and (d) show microcracks formed in the plane of the slip band. The white layer is a protective nickel coating.

100um



(a)  $\bar{\epsilon} = 0$



(b)  $\bar{\epsilon} = 0.03$

FIGURE 15. DEFORMATION BANDS ON THE SURFACE OF A 204°C TEMPERED 4340 STEEL BEND COUPON. The photographs are of cellulose acetate replicas of the same region of the specimen after different amounts of strain: (a)  $\bar{\epsilon} = 0$ , (b)  $\bar{\epsilon} = 0.03$ , (c)  $\bar{\epsilon} = 0.05$ , (d)  $\bar{\epsilon} = 0.10$ , and (e)  $\bar{\epsilon} = 0.15$ . The quantity  $\bar{\epsilon}$  is the true strain in the longitudinal direction. The dashed line in (e) shows the location and path of the fracture which occurred after an additional strain of 0.01. The letter a identifies a prominent inclusion visible on all the photographs; the letters b and c and the small arrows point to 2 superbands already evident at 5% strain. The large arrow identifies the principal strain direction.

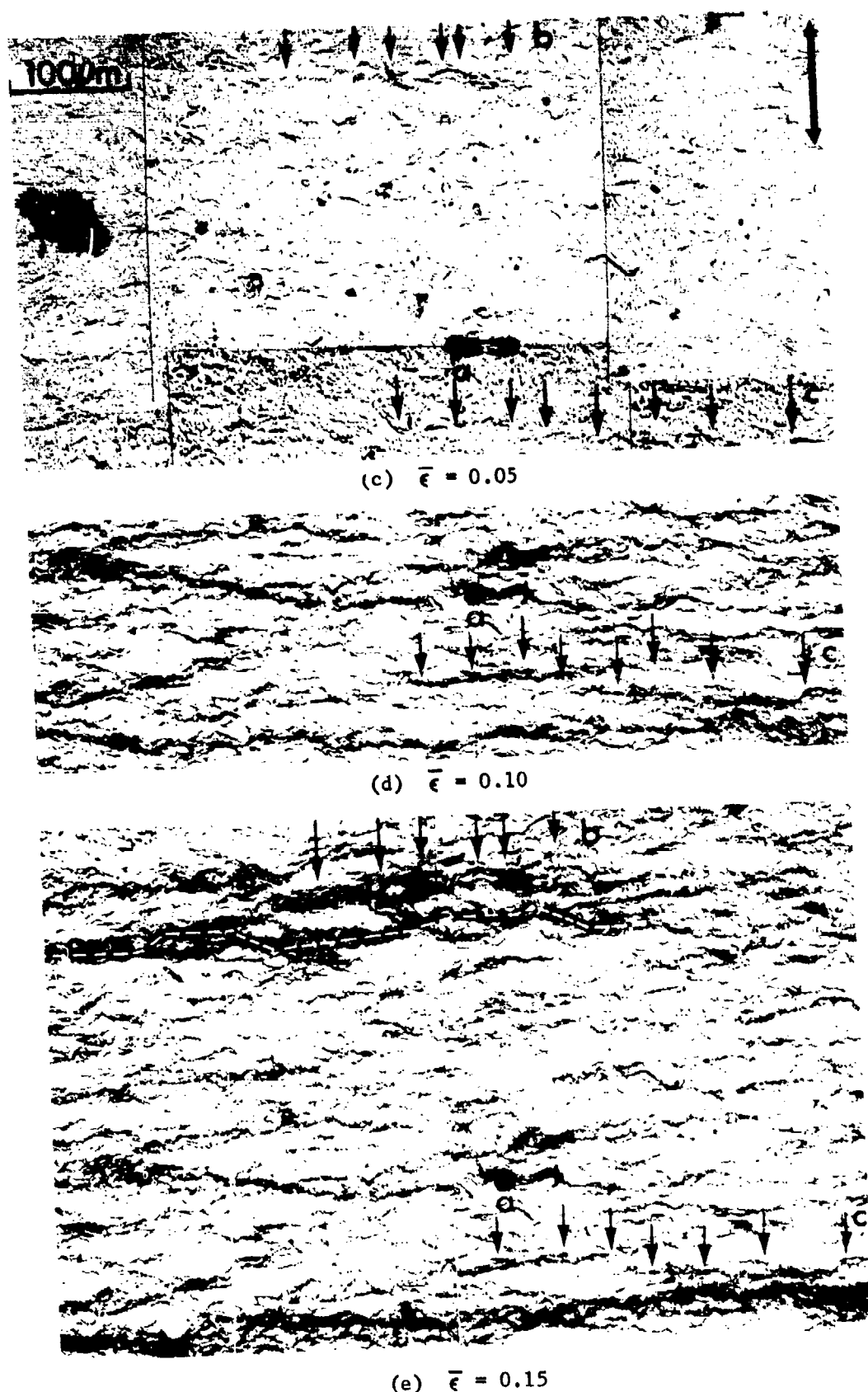


FIGURE 15. (Continued)

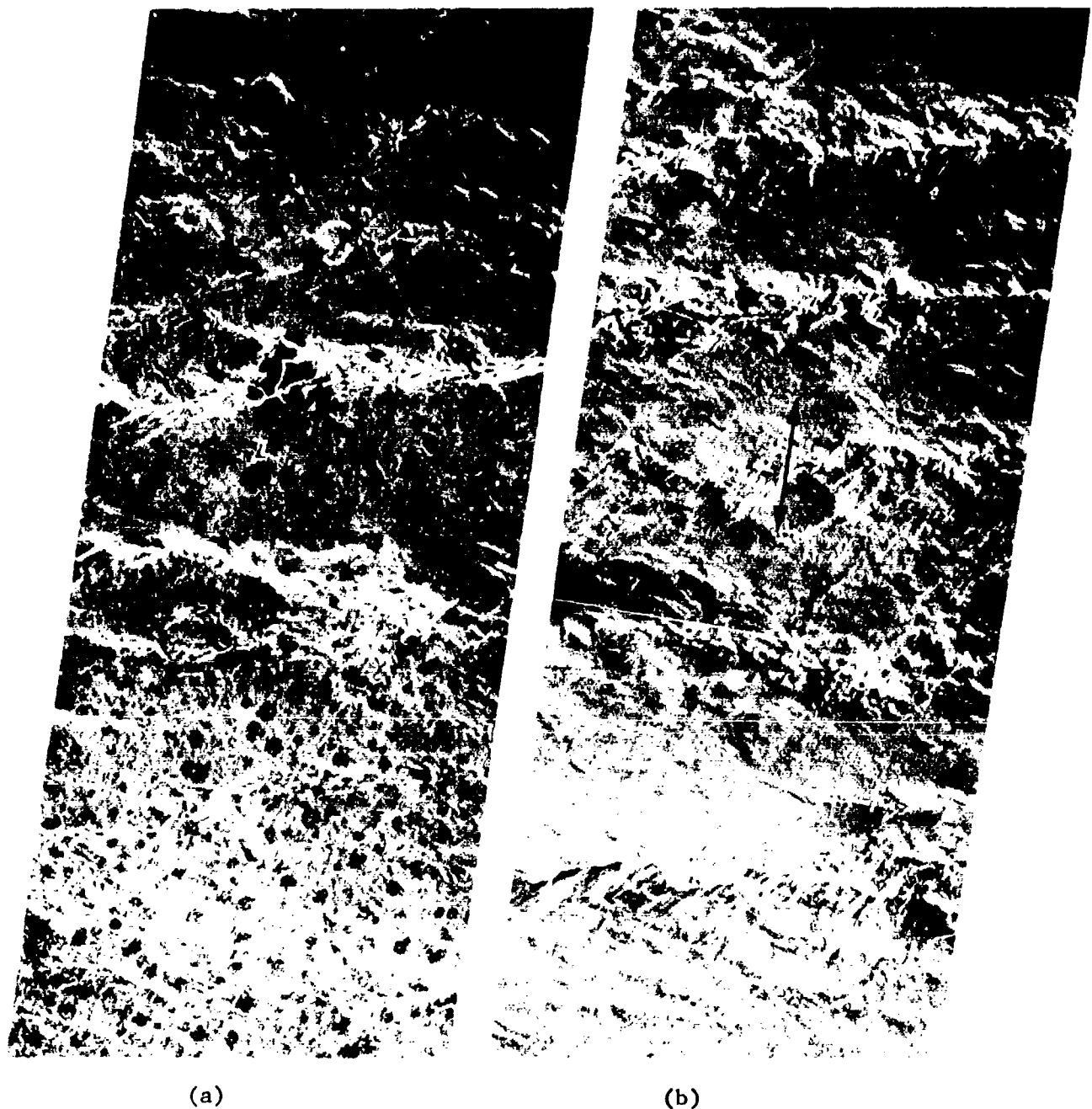
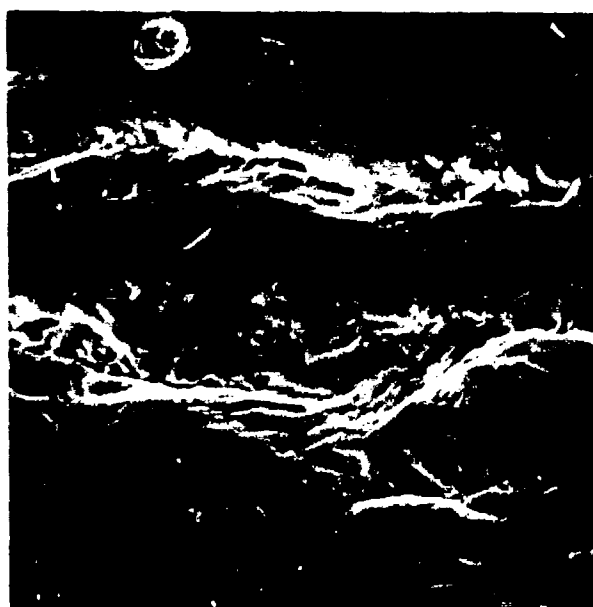
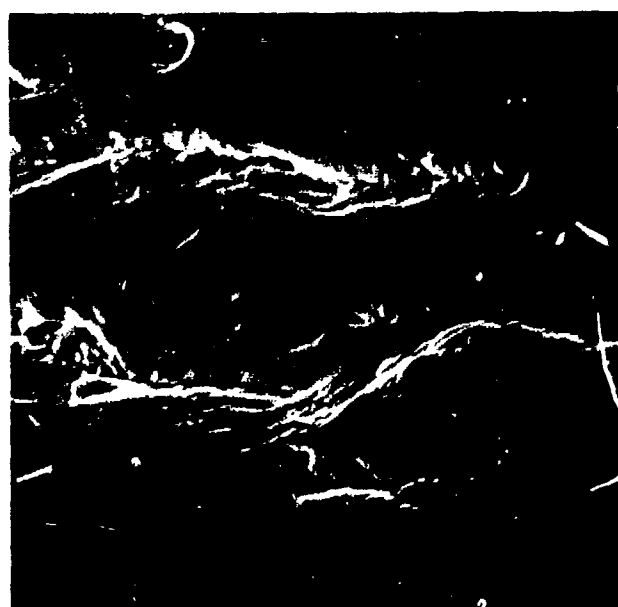


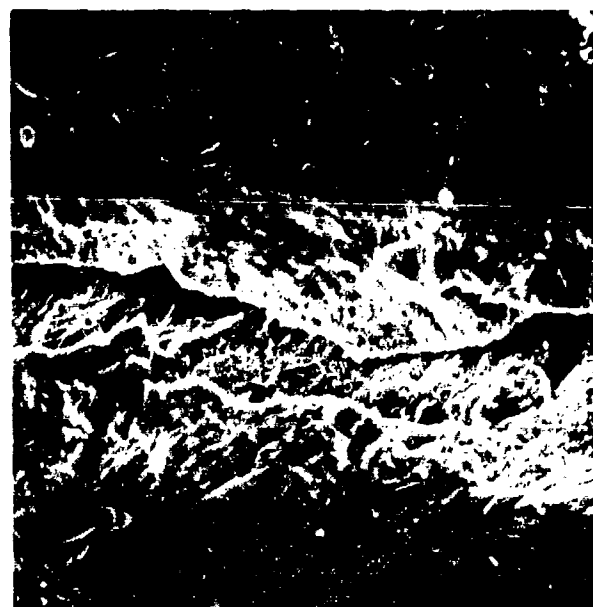
FIGURE 16. SCANNING ELECTRON MICROGRAPHS OF CRACKED SUPERBANDS ON THE SURFACE OF PLASTICALLY BENT 4340 STEEL STRIPS IN THE VICINITY OF THE FRACTURE: (a)  $204^{\circ}\text{C}$  tempered  $\bar{\epsilon} = 0.16$ , (b)  $538^{\circ}\text{C}$  tempered  $\bar{\epsilon} = 0.32$ . The black spots on the micrograph on the left are artifact (stains on the surface that occurred after deformation).



(c)



(d)



(a)



(b)

FIGURE 17. SEM STEREO PAIRS OF CRACKED SUPER BANDS ON THE SURFACE OF 538°C TEMPERED 4340 STEEL BEND SPECIMENS: (a) and (c) left-hand photograph 35°-tilt; (b) and (d) right-hand photograph 45°-tilt

- The tendency for forming superbands with intense strain concentrations is noticeably less pronounced at the higher tempering temperatures. Figures 12 and 13 reveal that superbands are broader and less sharply defined in the tougher 538°C tempered condition at a given strain level than in the material tempered at 204°C.
- Consistently with the greater uniformity of slip, cracks nucleate in the superbands at higher (average) strain in the tougher condition and are grown to a larger size before becoming unstable, as evidenced by the larger offsets displayed by the cracks in the 538°C tempered samples (compare Figure 16(a) with Figures 16(b) and 17(a)). The greater resistance to crack nucleation and growth is reflected by the larger average strain (plane strain ductility value) sustained by the specimen before fracture.

These observations show that the "plane strain" ductility of heat treated 4340 steel can be traced to the formation of superbands and the tendency for these to crack. The correlation between  $\bar{\epsilon}_{ps}$  and  $K_{Ic}$  implies that similar processes are at work at the crack tip. Several other features of these processes may aid in understanding the origins of toughness.

Figures 15, 18-21 show the progressive development of superbands and cracks by way of a series of replicas taken, of the same region of the surface. These replicas show that the superbands begin to form at relatively small strains. Traces of some of the bands are already evident on the replicas taken at 5% and 8% strain. Another unusual feature of the superbands is that they occasionally involve two orthogonal slip bands. This is evident in Figure 14(b), which shows that a trough has formed between the two slip bands. Such a trough is also apparent between the two prominent deformation bands in Figures 17(c) and 17(d) when these two photographs are viewed as a stereo pair.

It is also apparent that the larger, 5-10  $\mu\text{m}$ , inclusions play a role in the rupture process. This is more evident in the micrographs of the tougher, 538°C tempered condition (see Figures 20 and 21), which show that the ruptured inclusions

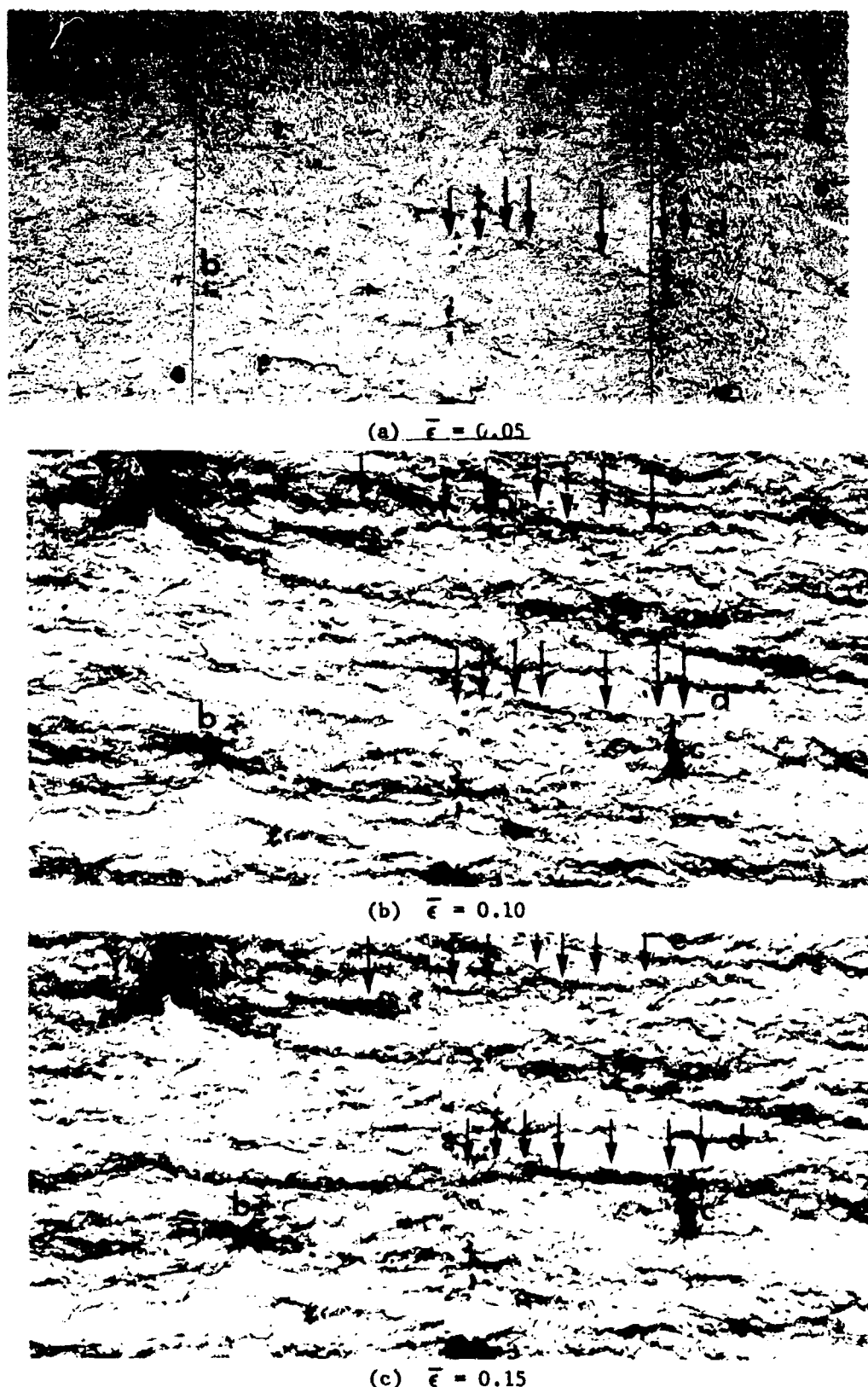
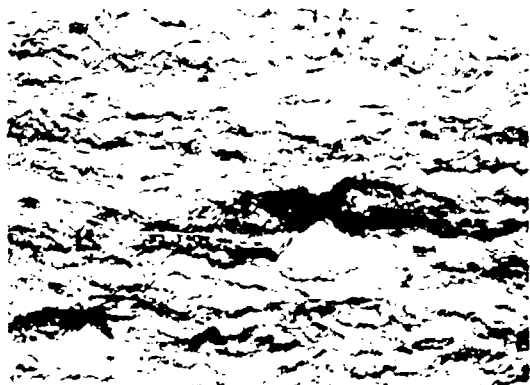


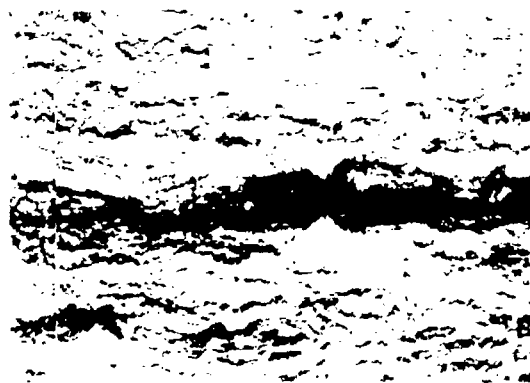
FIGURE 18. EXAMPLES OF DEFORMATION BANDS ON THE SURFACE OF A 204°C TEMPERED 4340 STEEL BEND COUPON. The photographs are of cellulose acetate replicas of the same region of the specimen after different amounts of strain: (a)  $\bar{\epsilon} = 0.05$ , (b)  $\bar{\epsilon} = 0.10$ , and (c)  $\bar{\epsilon} = 0.15$ . The vertical markings at a and c are inclusions strung out in the rolling direction. The letter b identifies a void associated with an inclusion just below the surface. The arrows at d and e identify 2 superbands which began to develop at small strains. The large arrow identifies the principal strain direction.



(a)  $\bar{\epsilon} = 0.09$



(b)  $\bar{\epsilon} = 0.12$



(c)  $\bar{\epsilon} = 0.15$

FIGURE 19. FORMATION OF A SUPERBAND AT A RUPTURED INCLUSION ON THE SURFACE OF 204°C TEMPERED 4340 STEEL BEND COUPON. The photographs show cellulose acetate replicas of the same region after different amounts of strain: (a)  $\bar{\epsilon} = 0.09$ , (b)  $\bar{\epsilon} = 0.12$ , and (c)  $\bar{\epsilon} = 0.15$

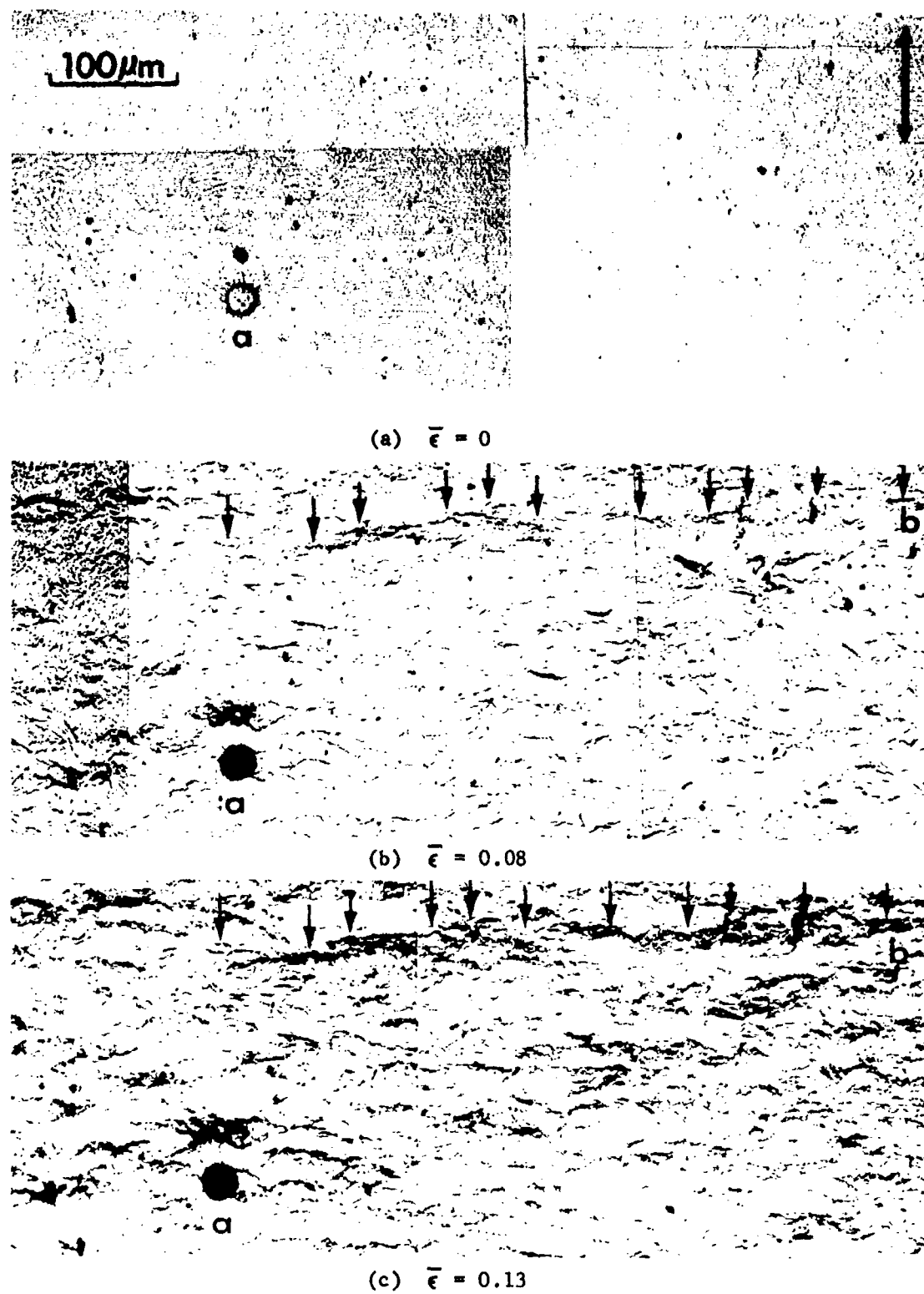


FIGURE 20. DEFORMATION BANDS ON THE SURFACE OF A 538°C TEMPERED 4340 STEEL BEND COUPON. The photographs are of cellulose acetate replicas of the same region of the specimen after different amounts of strain: (a)  $\bar{\epsilon} = 0$ , (b)  $\bar{\epsilon} = 0.08$ , (c)  $\bar{\epsilon} = 0.13$ , (d)  $\bar{\epsilon} = 0.19$ , (e)  $\bar{\epsilon} = 0.23$ , and (f)  $\bar{\epsilon} = 0.30$ . The letter a identifies a prominent inclusion visible on all of the photographs; the letter b and the arrows identify a developing superband.



FIGURE 20. (CONTINUED)

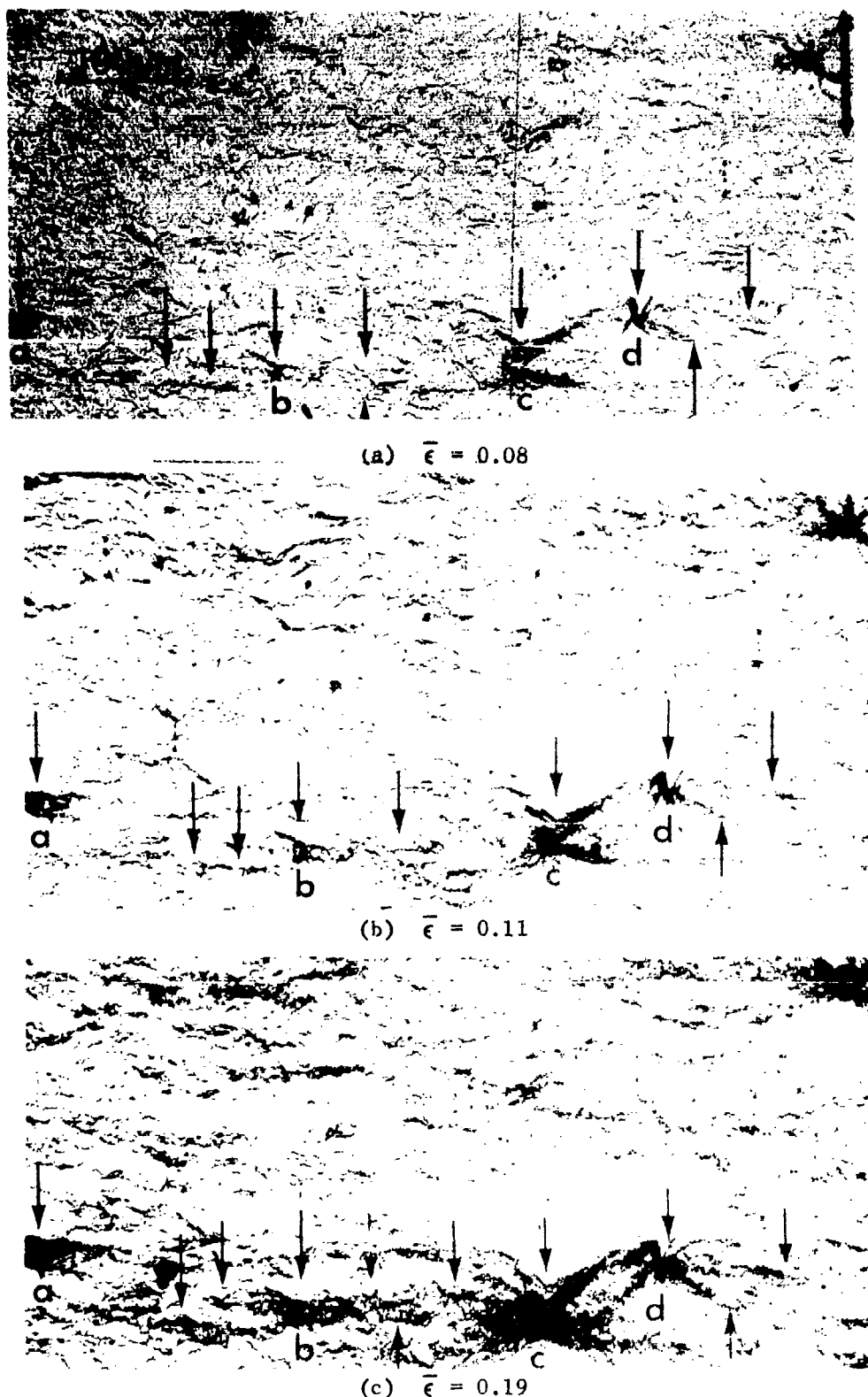
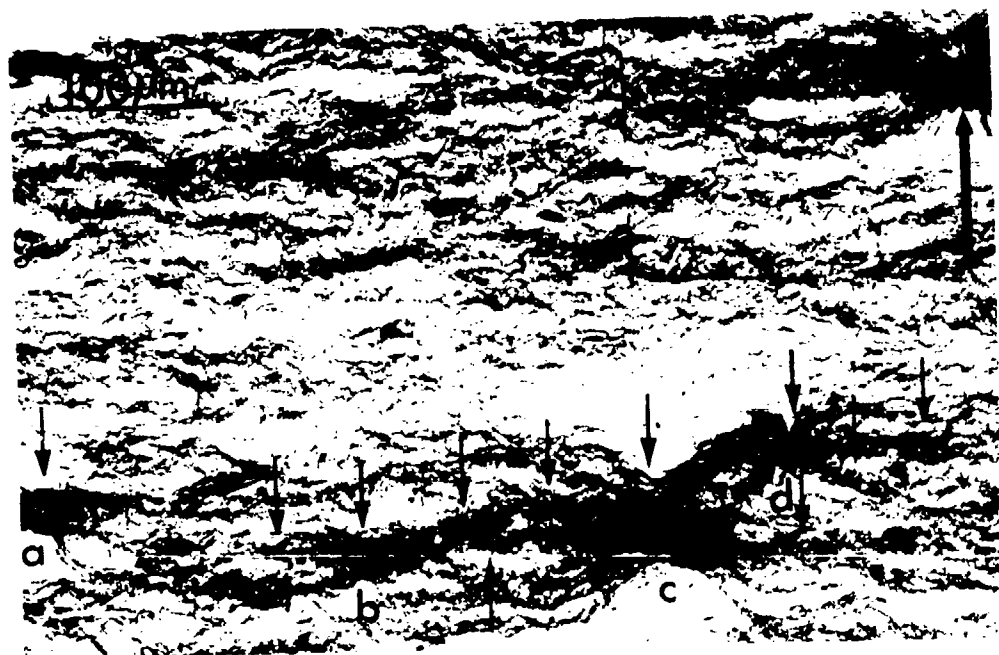
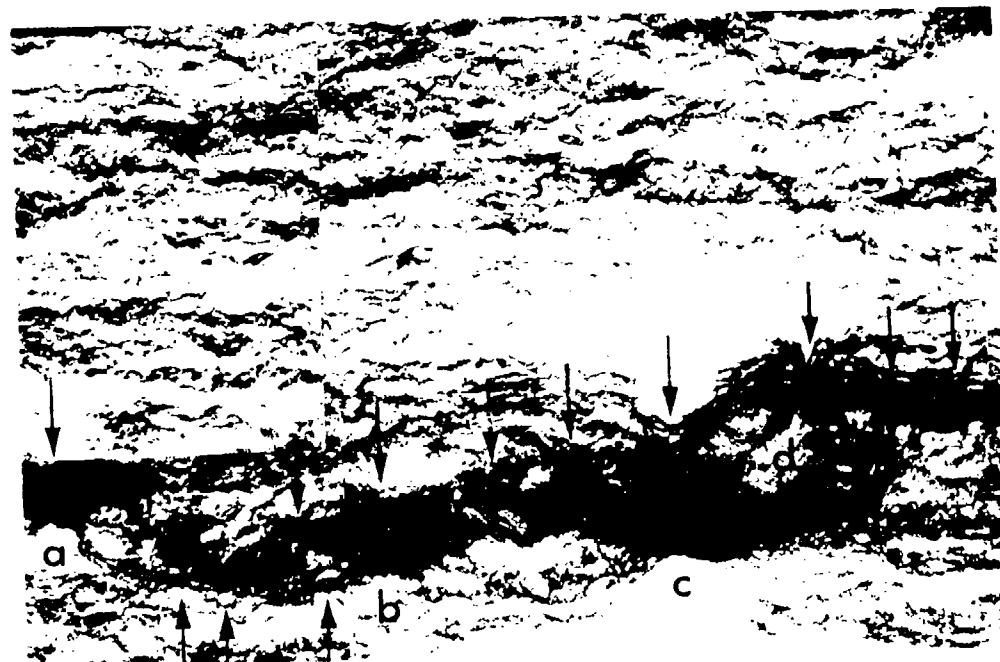


FIGURE 21. FORMATION OF SUPER BANDS AND CRACKS BY RUPTURED INCLUSIONS ON THE SURFACE OF A 538°C TEMPERED 4340 STEEL BEND COUPON. The photographs show cellulose acetate replicas of the same region after different amounts of strain: (a)  $\bar{\epsilon} = 0.08$ , (b)  $\bar{\epsilon} = 0.11$ , (c)  $\bar{\epsilon} = 0.19$ , (d)  $\bar{\epsilon} = 0.23$ , and (e)  $\bar{\epsilon} = 0.30$ . The letters a, b, c, and d identify inclusions which are involved in the developing superband and rupture shown by the small arrows. The large arrow shows the principal strain direction.



(d)  $\bar{\epsilon} = 0.23$



(e)  $\bar{\epsilon} = 0.30$

FIGURE 21. (CONTINUED)

tend to produce strain concentrations and superbands which ultimately form the path of the final rupture. While Figure 19 shows a similar event in progress in the 204°C tempered material, the involvement of visible inclusions with superbands is less apparent in this condition (see Figures 15 and 18).

Figures 22 and 23 show the appearance of individual slip bands at higher magnifications. These bands are typically 10  $\mu\text{m}$  to 20  $\mu\text{m}$  long and involve slip offsets as large as 2-3 microns. Figures 24 and 25 show that cracks tend to form at the base of large 2-3  $\mu$  slip offsets. Figure 26 shows the distribution of the size of slip offsets measured on the surface of samples tempered at different temperatures. In all cases, the bulk of the slip offsets is smaller than 1  $\mu\text{m}$ . However, there are indications that larger offsets are obtained for a given strain as the tempering temperature is reduced. There is also an indication (see Figure 27) that the slip band offsets at the various tempered conditions may be comparable when the comparison is made at  $\bar{\epsilon}_1 = \bar{\epsilon}_{ps}$ , the strain corresponding to the onset of fracture.

## 2. NI-MARAGING STEEL

Plane strain ductility values from double-bend tests of 250-grade and 300-grade maraging steel are presented in Figure 28 together with toughness values for 250-grade material reported by Srawley<sup>(28)</sup>. The heat treatments and tensile properties of the two lots of the 250-grade were essentially the same.<sup>†</sup> Toughness values of

<sup>†</sup> Heat treated by solution annealing at 816°C for 1 hr. and aging for 6 hrs. at the indicated temperatures:

### Mechanical Studies of 250-Grade Maraging Steel

PRESENT STUDY						SRAWLEY <sup>(28)</sup>					
Aging Treat't.	R <sub>c</sub>	$\sigma_Y$ MNm <sup>-2</sup> (Ksi)	$\sigma_{ULT}$ MNm <sup>-2</sup> (Ksi)	$\epsilon\%EL$	%RA	$\sigma_Y$ MNm <sup>-2</sup> (Ksi)	$\sigma_{ULT}$ MNm <sup>-2</sup> (Ksi)	$\epsilon\%EL$	%RA		
Underaged, 399°C	47	1469 (213)	1469 (213)	14	65	1400 (203)	1434 (208)	14	57		
Peak aged, 482°C	49	1841 (267)	1841 (267)	12	59	1786 (259)	1834 (266)	11	51		
Overaged, 566°C	47	1503 (218)	1572 (228)	15	61	1407 (204)	1503 (218)	15	50		

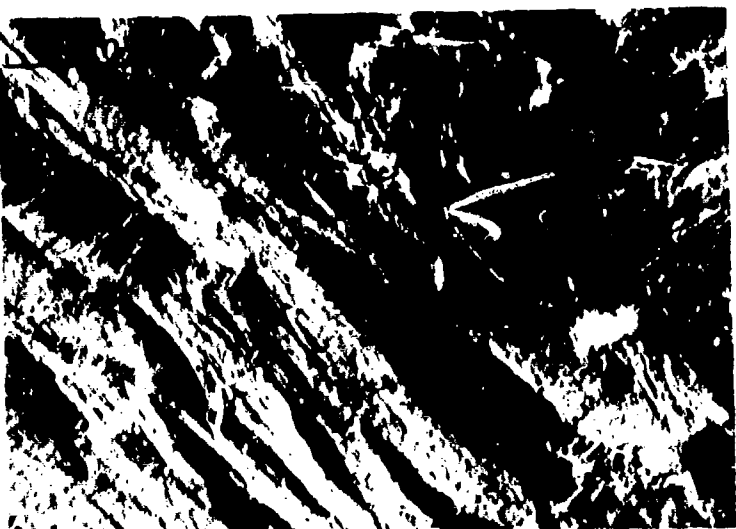


(b)  $\bar{\epsilon} = 28\%$

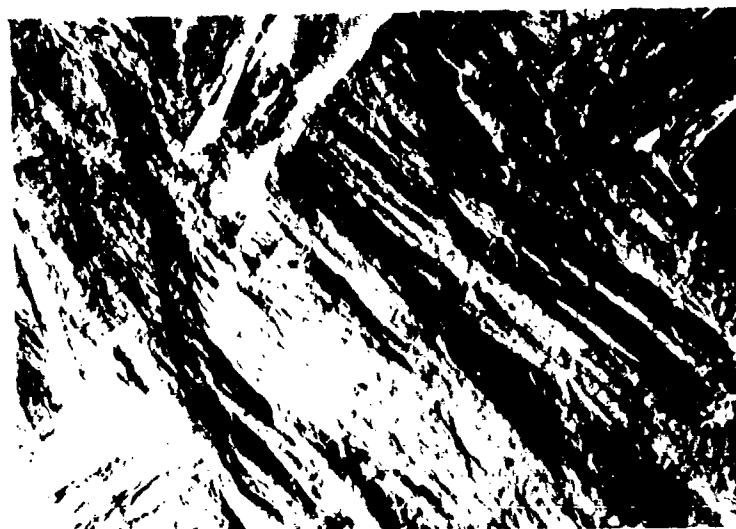


(a)  $\bar{\epsilon} = 30\%$

FIGURE 22. SLIP MARKINGS ON THE SURFACE OF 538°C TEMPERED AISI 4340 STEEL BEND SPECIMENS: (a) SEM micrograph, and (b) transmission micrograph of a cellulose acetate replica. The hole in (a) was probably associated with an inclusion particle



(a)  $\bar{\epsilon} = 28\%$



(b)  $\bar{\epsilon} = 28\%$



(c)  $\bar{\epsilon} = 23\%$

FIGURE 23. SLIP OFFSETS ON THE SURFACE OF 538°C TEMPERED AISI4340 STEEL BEND SPECIMENS OBSERVED ON TRANSMISSION MICROGRAPHS OF CELLULOSE ACETATE REPLICAS

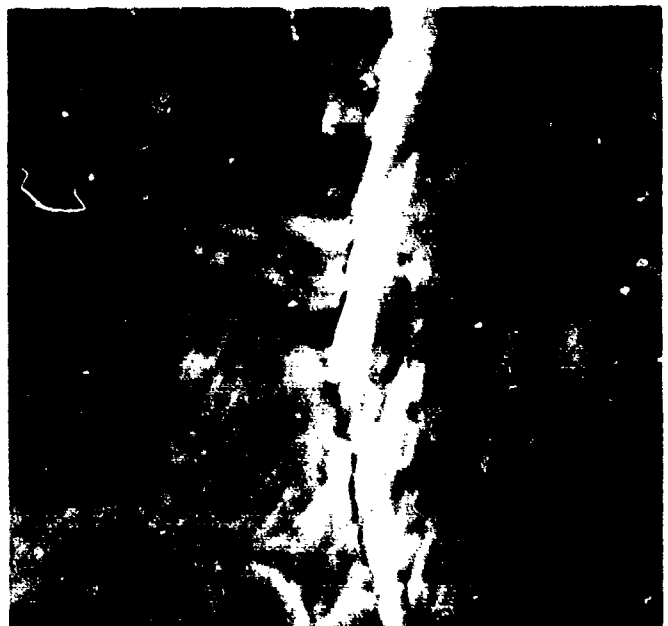
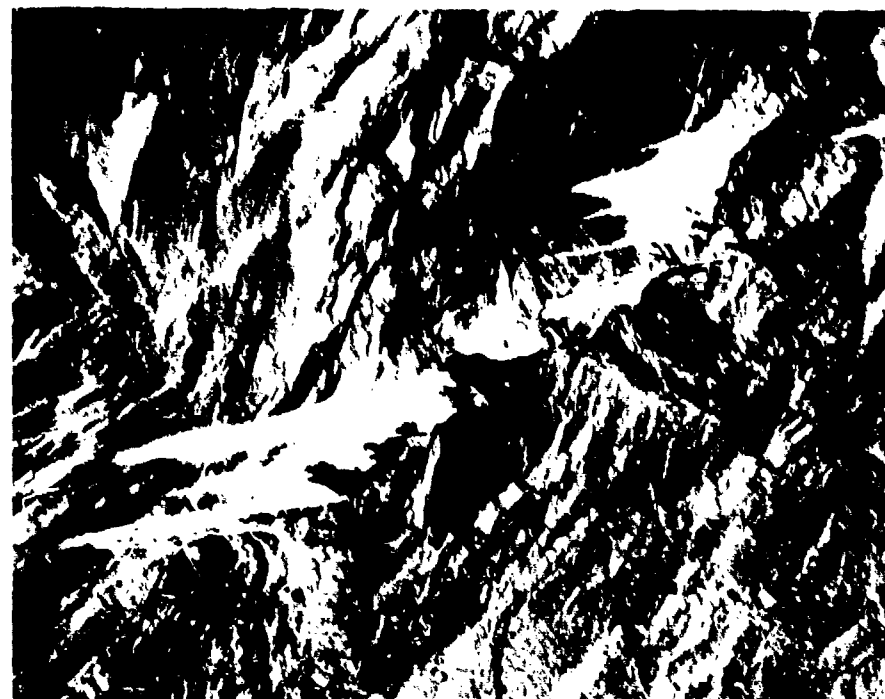
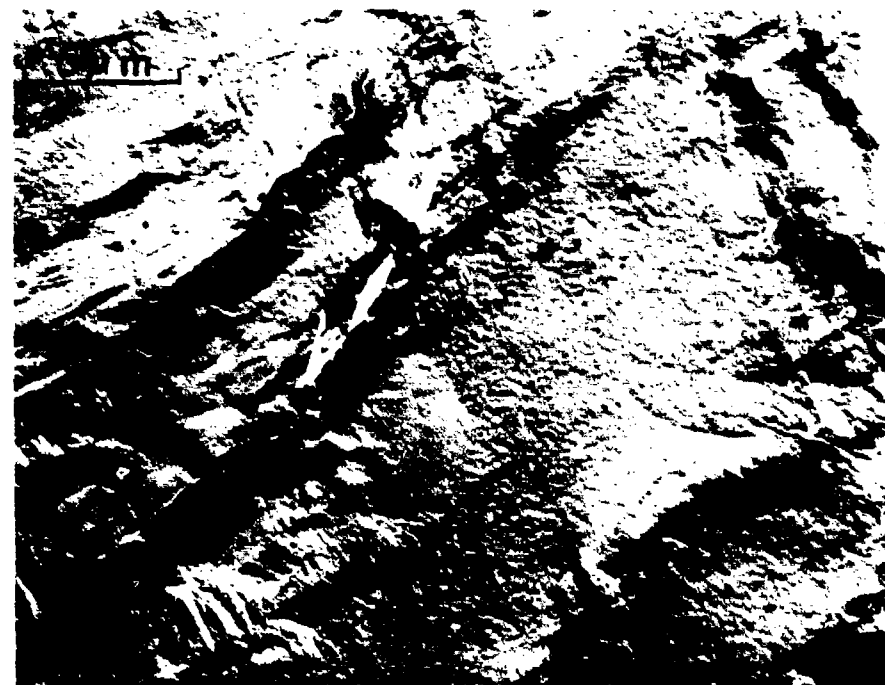


FIGURE 24. SEM STEREO PAIR OF A CRACKED SLIP BAND ON THE SURFACE OF A 204°C TEMPERED 4340 STEEL BEND SPECIMEN.



(a)  $\bar{\epsilon} = 23\%$



(b)  $\bar{\epsilon} = 23\%$

FIGURE 25. CRACKS AT THE BASE OF LARGE SLIP OFFSETS ON THE SURFACE 538°C TEMPERED AISI4340 STEEL BEND SPECIMENS. The cellulose acetate replicating medium which seeped into the crack cavity looks like a tongue on the stripped replica and cast a long shadow

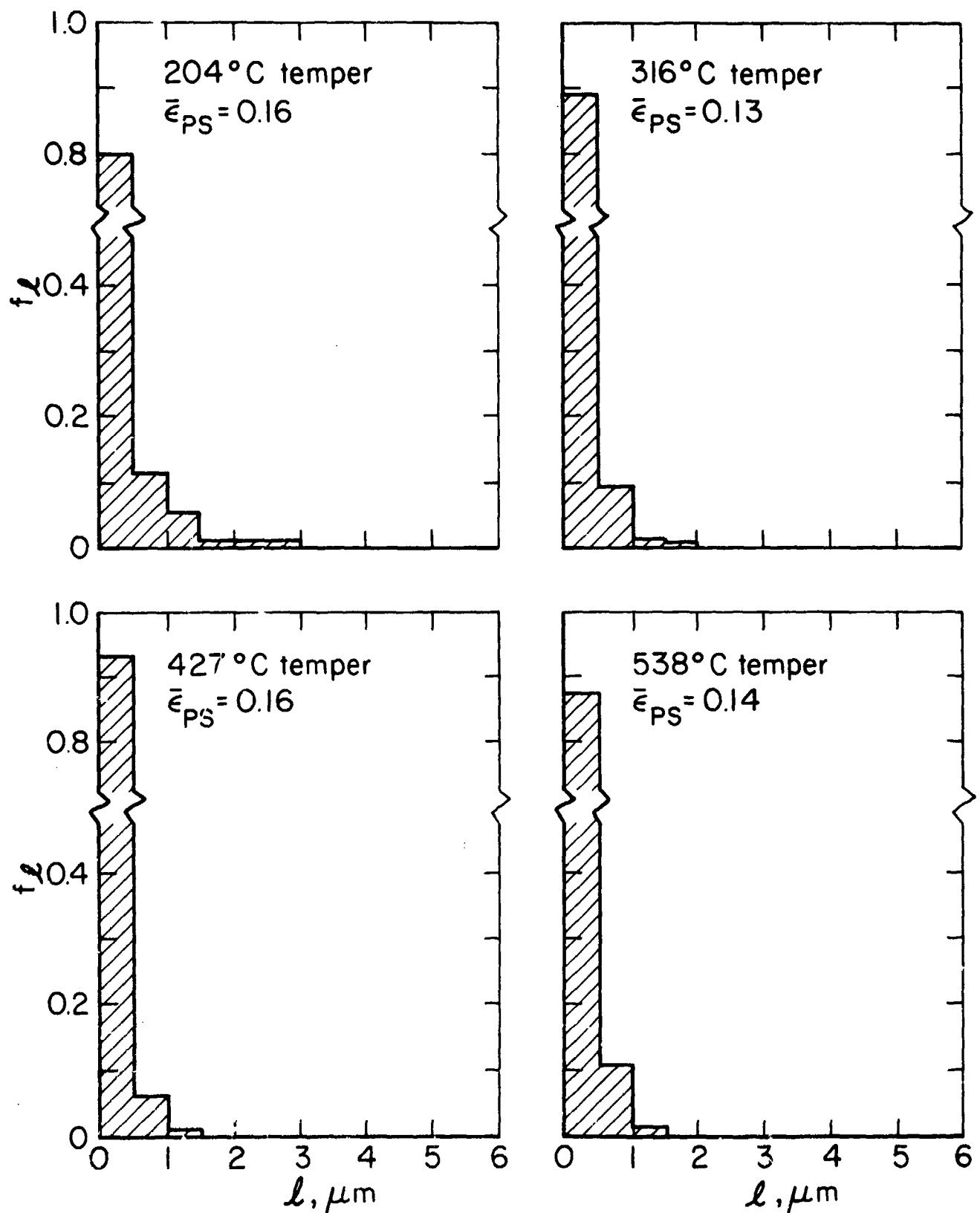


FIGURE 26. DISTRIBUTION OF SLIP OFFSETS ON ELECTRON MICROGRAPHS OF 4340 STEEL TEMPERED AT DIFFERENT TEMPERATURES. The measurements were made on replicas of regions of the surface of plane strain (double) bend specimens subjected to about the same plane strain ( $0.13 \leq \bar{\epsilon}_1 \leq 0.16$ )

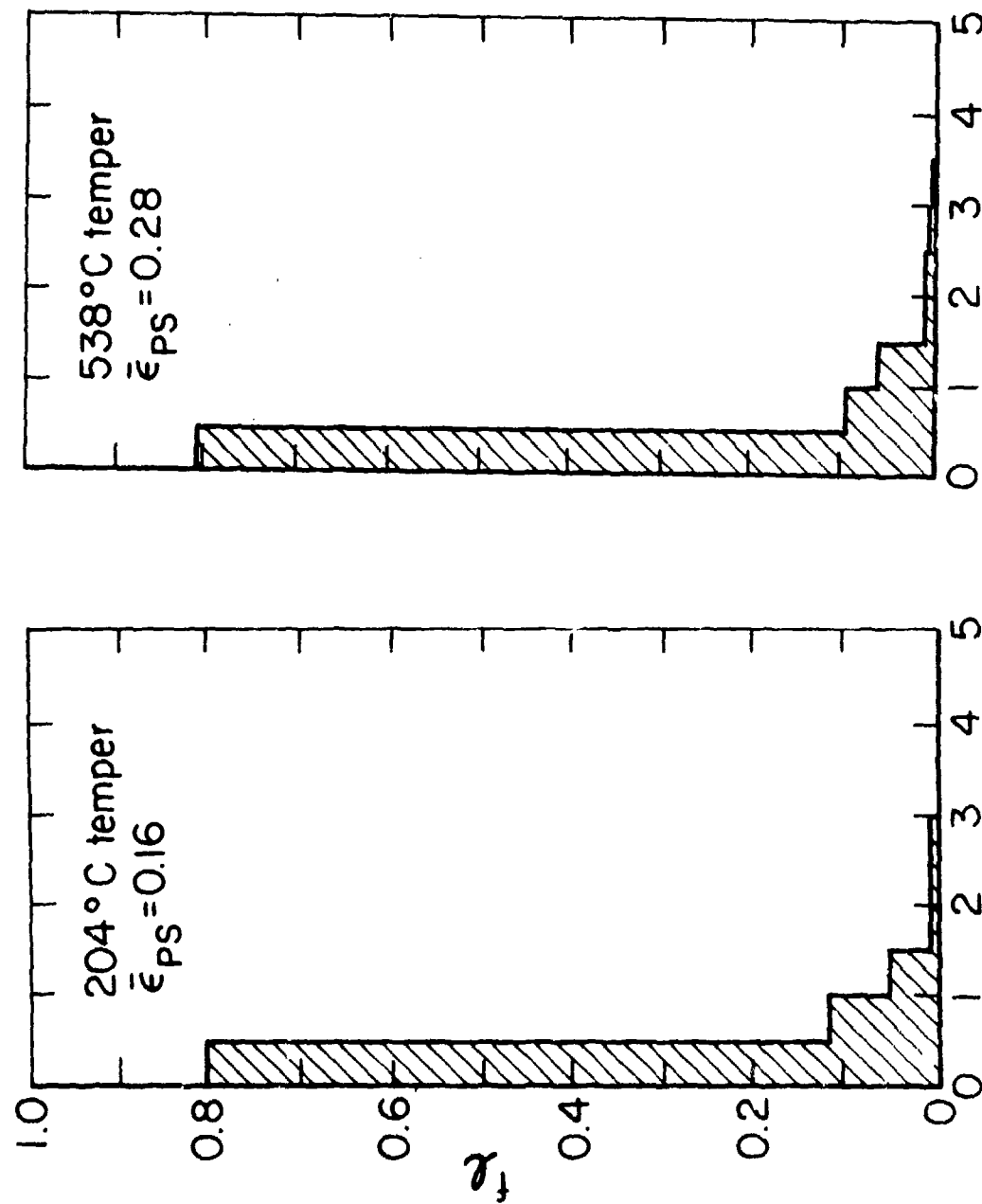


FIGURE 27. DISTRIBUTION OF SLIP OFFSETS ON ELECTRON MICROGRAPHS OF 4340 STEEL PLANE STRAIN (DOUBLE) BEND SPECIMENS AT THE ONSET OF FRACTURE

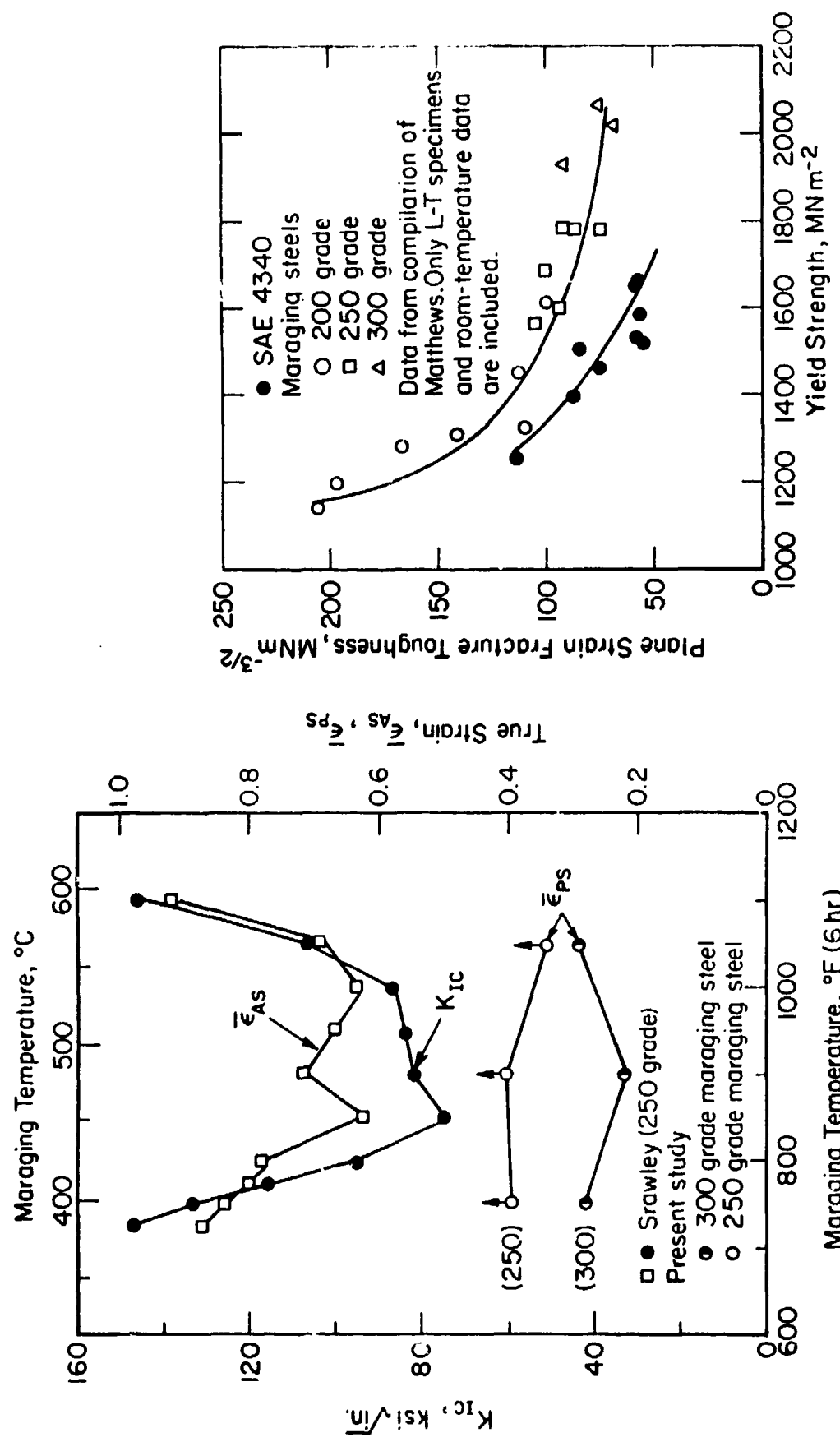


FIGURE 28. MECHANICAL PROPERTIES OF MARAGING STEELS: (a) influence of maraging temperature on  $K_{Ic}$  after Strawley (28) and the plane strain ductility  $\bar{\epsilon}_{PS}$  (present study) and (b) influence of strength level on  $K_{Ic}$  after Matthews (29)

the 250-grade and 300-grade maraging steel are also similar at comparable strength levels, as shown in Figure 28(b). The main features of the results may be summarized as follows:

- Plane strain ductility values displayed by the maraging grades are substantially greater than the values for the 4340 steel at the same strength level. This is also true of  $K_{Ic}$ -values (see Figure 28b). The  $\bar{\epsilon}_{PS}$ -values plotted for the 250 grade actually represent lower bounds because the specimens cracked but did not actually rupture.
- Unlike the results for the 4340 steel, the plane strain ductility values for the maraging steels do not seem to correlate with  $K_{Ic}$ -values.

Microstructural studies revealed that rupture of the maraging steels under "plane strain" biaxial tension also proceeds by the formation of superbands, as shown in Figures 29 and 30. However, two important differences are evident.

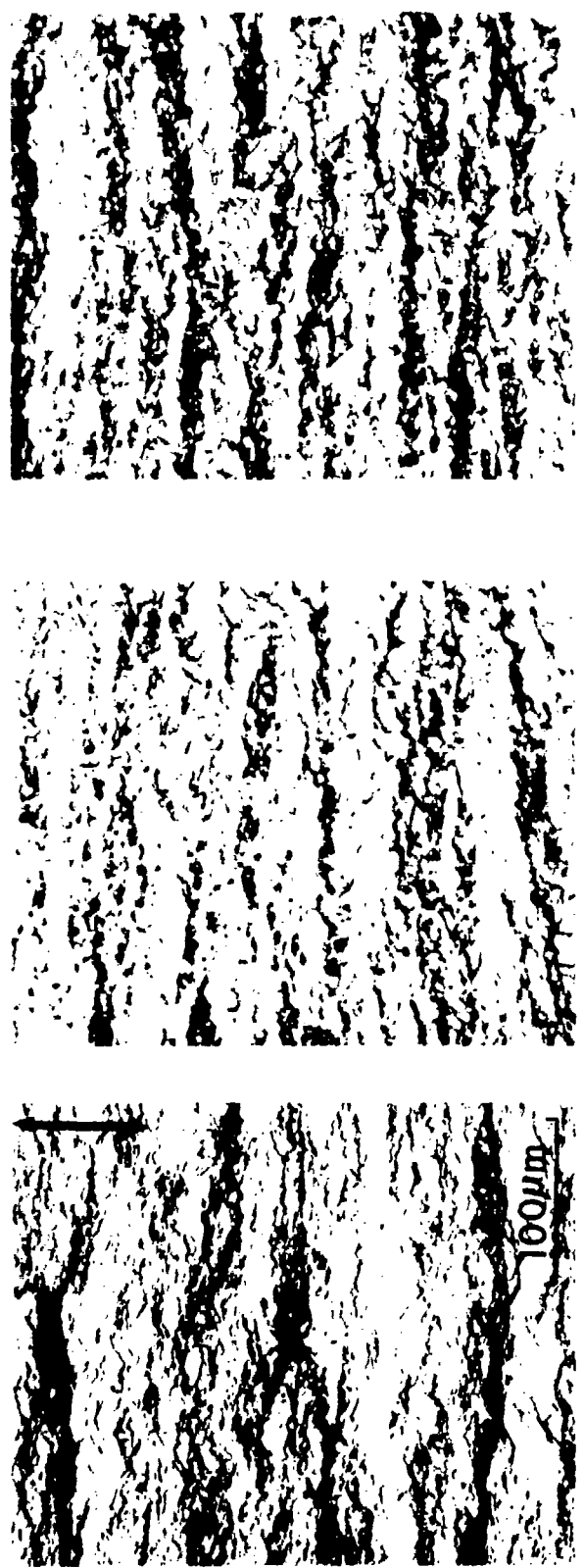
- (i) The large slip offsets that contribute to the nucleation of cracks occur at the grain boundaries. Evidence of this can be seen in higher magnification optical micrographs (Figures 30, 31) and in the scanning electron micrograph (Figure 32).
- (ii) In contrast, slip offsets within the grains are noticeably finer in the maraging grade than in the 4340 steel. This is shown in Figure 33, and more quantitatively by the slip offset measurements presented in Figures 34 and 35.

### 3. 6Al-4V-TITANIUM ALLOY

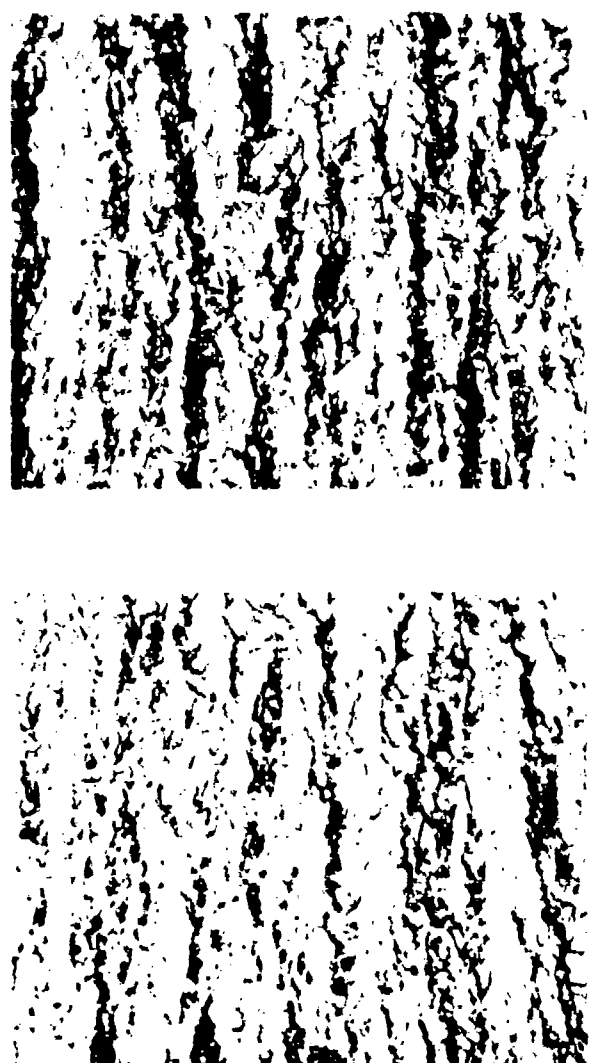
The fracture behavior and appearance of heat treated Ti-6Al-4V<sup>†</sup> plane-strain bend coupons<sup>††</sup> was similar to that of the maraging steels. Fracture proceeded

<sup>†</sup> Heat treatment mechanical properties:  $\sigma_y = 958 \text{ MNm}^{-2}$  (139 ksi),  $\sigma_{UTS} = 1055 \text{ MNm}^{-2}$  (153 ksi), uniform elongation 6.1%, El. 10%, R.A., 28%,  $\bar{\epsilon}_{PS}$  (ordinary bend specimens) = 0.36.

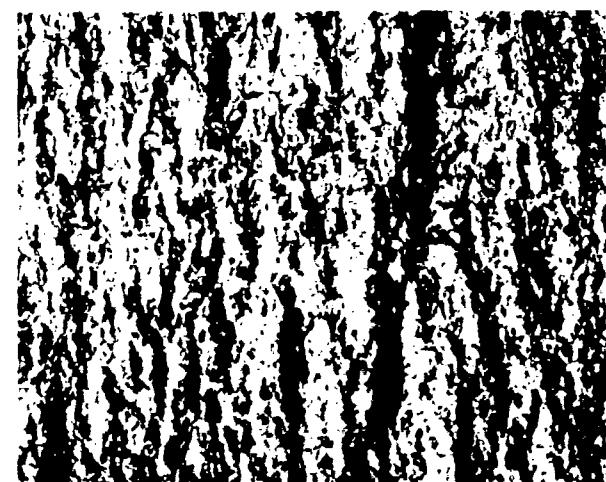
<sup>††</sup> Ordinary bend coupons rather than the double-bend coupons that evolved later in the program.



(a) 4340 steel,  $\dot{\epsilon}_{PS} = 0.15$



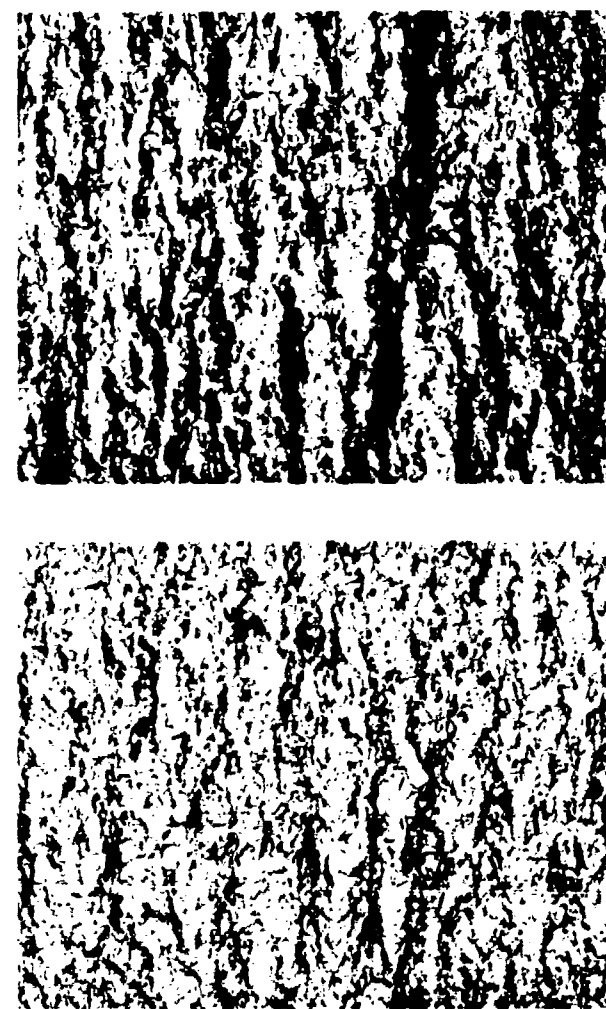
(b) 250 grade  $\dot{\epsilon}_1 = 0.15$



(c) 250 grade  $\dot{\epsilon}_{PS} \approx 0.40$



(d) 300 grade  $\dot{\epsilon}_1 = 0.15$



(e) 300 grade  $\dot{\epsilon}_{PS} = 0.29$

FIGURE 29. COMPARISON OF THE DEFLECTION BANDS ON THE SURFACE OF 250-GRADE AND 300-GRADE MARAGING STEEL AND 4340 STEEL "PLANE-STRAIN" (DOUBLE) BEND SPECIMENS: (a) 4340 Steel,  $\sigma_Y = 1430 \text{ MNm}^{-2}$  (214 ksi), (b) and (c) 250-grade maraging steel, peak aged,  $\sigma_Y = 1424 \text{ MNm}^{-2}$  (211 ksi), (d) and (e) 300-grade maraging steel, overaged.

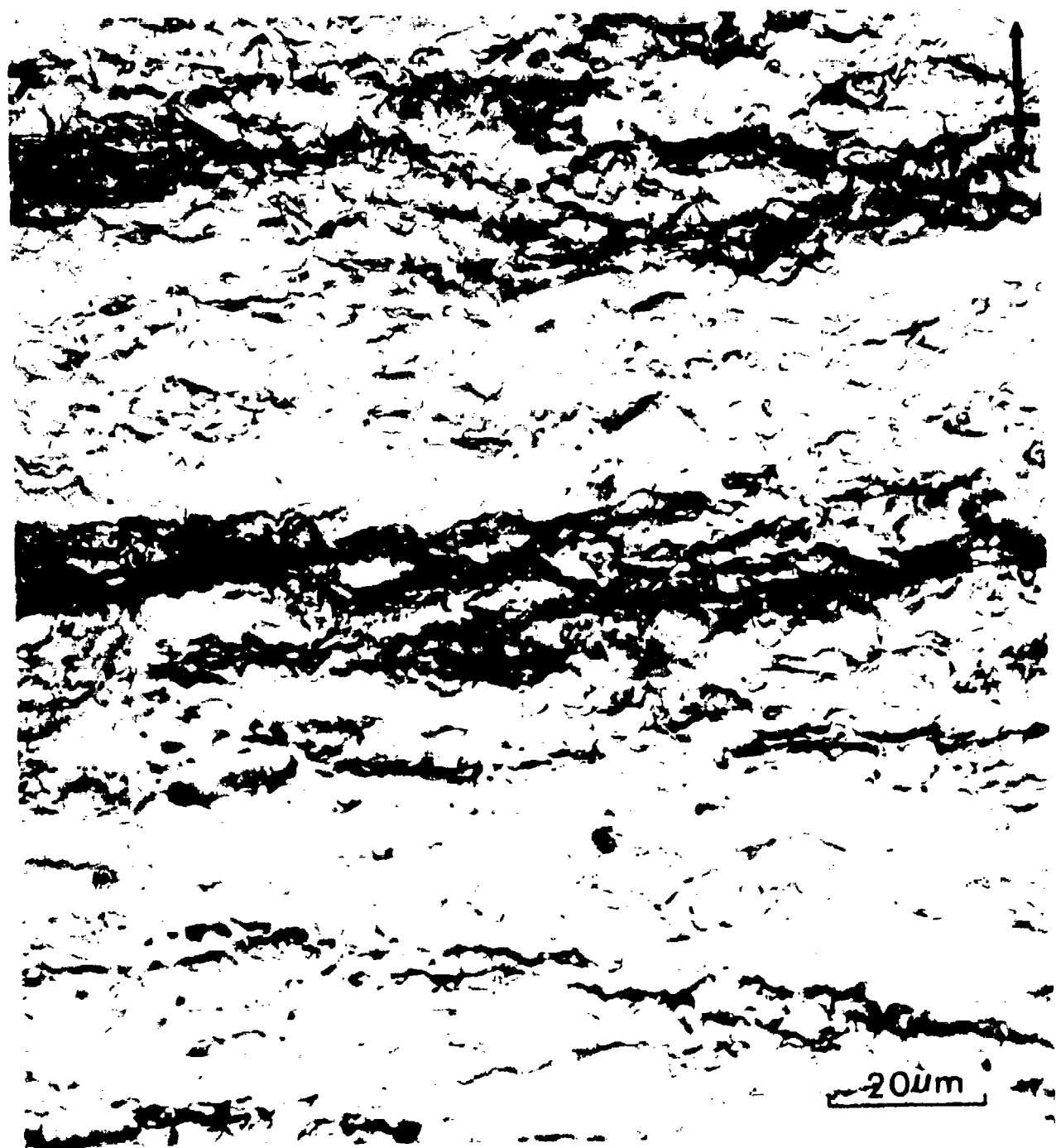


FIGURE 30. APPEARANCE OF SUPERBANDS ON THE SURFACE OF 250-GRADE MARAGING STEEL "PLANE-STRAIN" (DOUBLE) BEND SPECIMEN: (a) superband and (b) example of a cracked band. Material in the peak aged condition;  $\bar{\epsilon}_{ps} \geq 0.40$



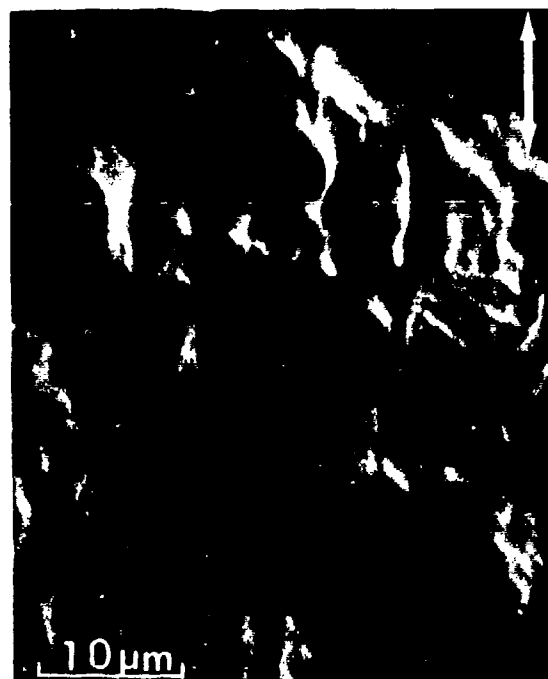
FIGURE 31. EXAMPLE OF A CRACKED SUPERBAND ON THE SURFACE OF 250-GRADE MARAGING STEEL "PLANE STRAIN" (DOUBLE-BEND SPECIMEN. Material in peak-aged condition;  $\bar{\epsilon}_{PS} \geq 0.40$



(a)



(b)

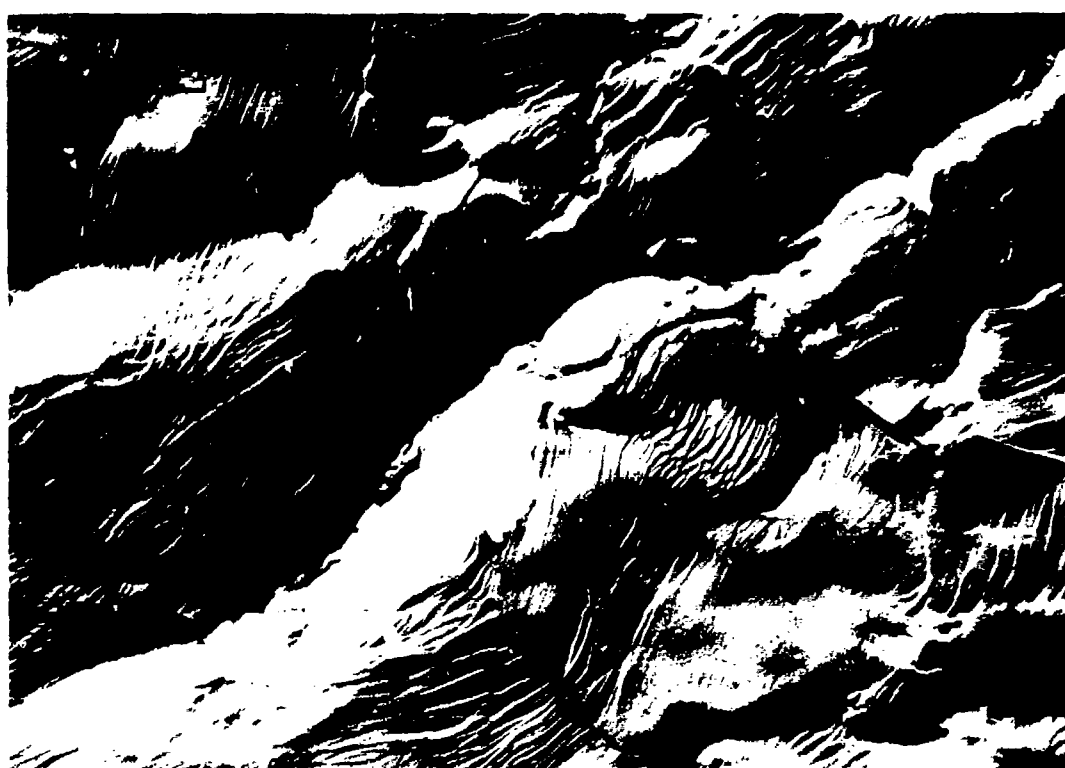


(c)



(d)

FIGURE 32. SCANNING ELECTRON MICROGRAPHS OF SURFACE OF 250-GRADE MARAGING STEEL PLANE STRAIN (DOUBLE) BEND SPECIMEN: (a) superbands, (b) cracked band, (c) and (d) stereo pair of deformed surface showing grain boundary offsets



(a)



(b)

FIGURE 33. SLIP MARKINGS ON THE SURFACE OF 300-GRADE MARAGING STEEL IN THE PEAK-AGED CONDITIONS SHOWING SLIP BANDS AND GRAIN BOUNDARY OFFSETS: (a) cracked superband and (b) grain boundary offsets in the vicinity of the band

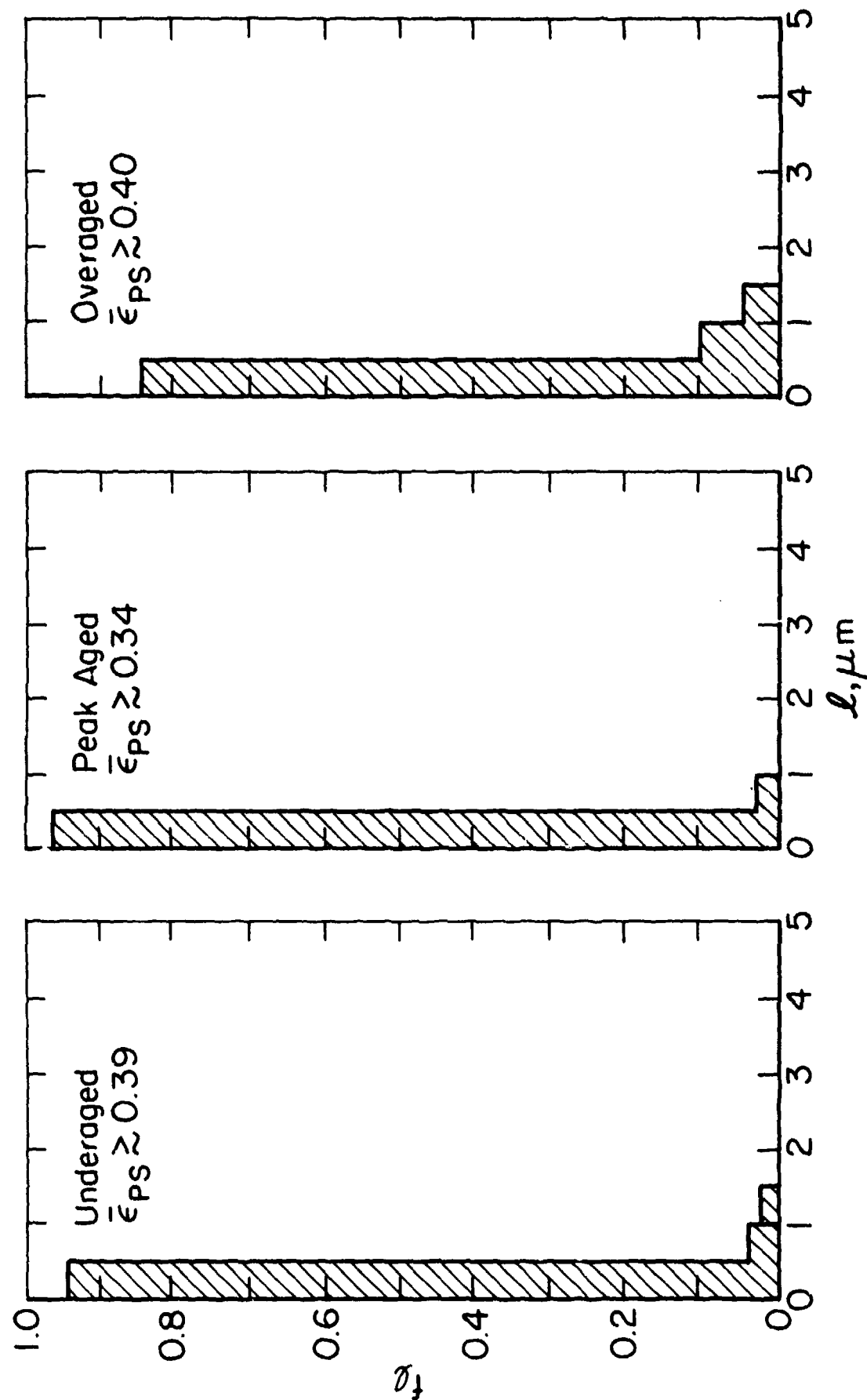


FIGURE 34. DISTRIBUTION OF SLIP OFFSETS ON ELECTRON MICROGRAPHS OF 250-GRADE MARAGING STEEL, "PLANE STRAIN" (DOUBLE) BEND SPECIMENS AT THE ONSET OF FRACTURE

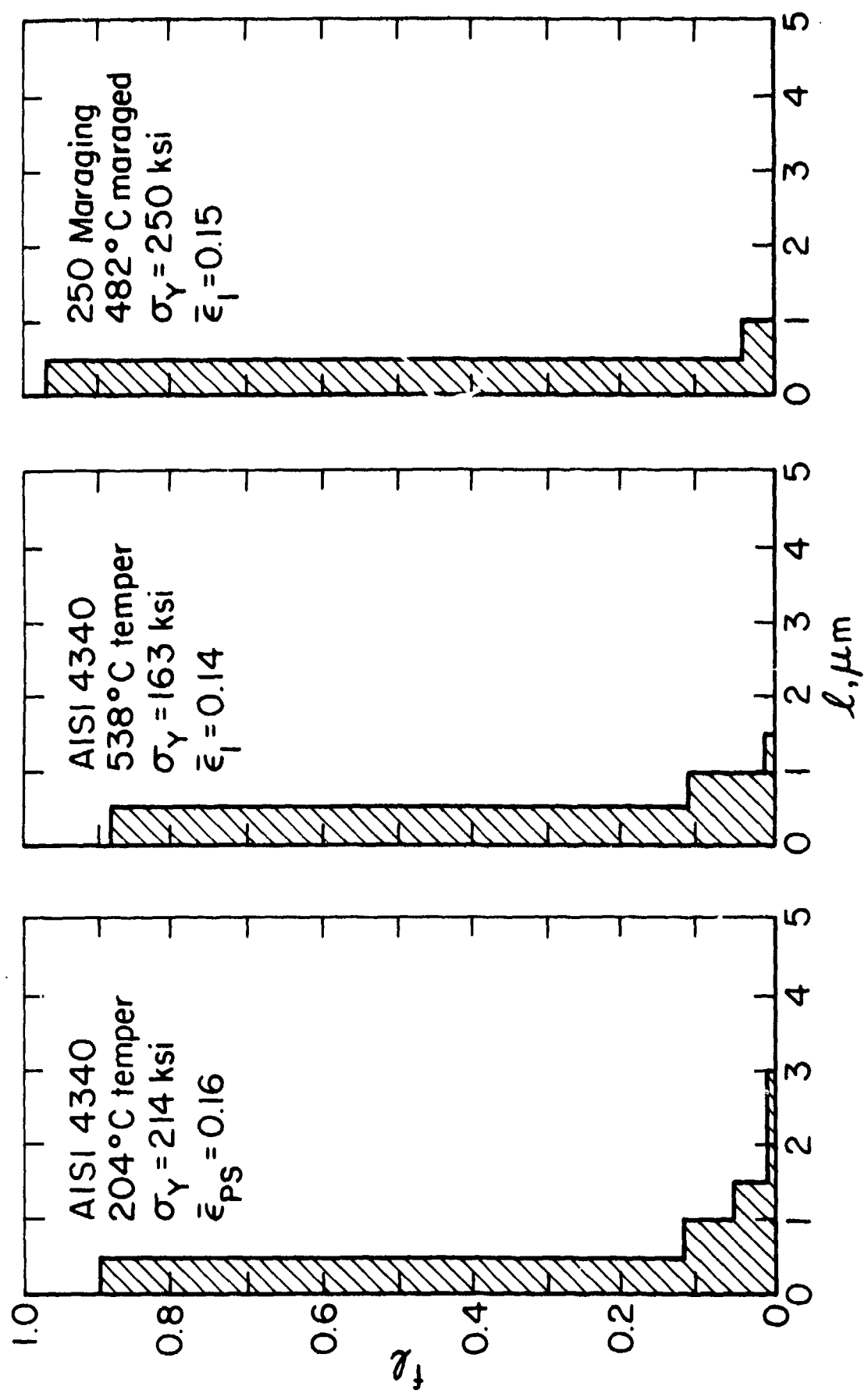


FIGURE 35. MEASUREMENTS OF SLIP BAND OFFSETS ON THE SURFACE OF TWO HIGH STRENGTH STEELS

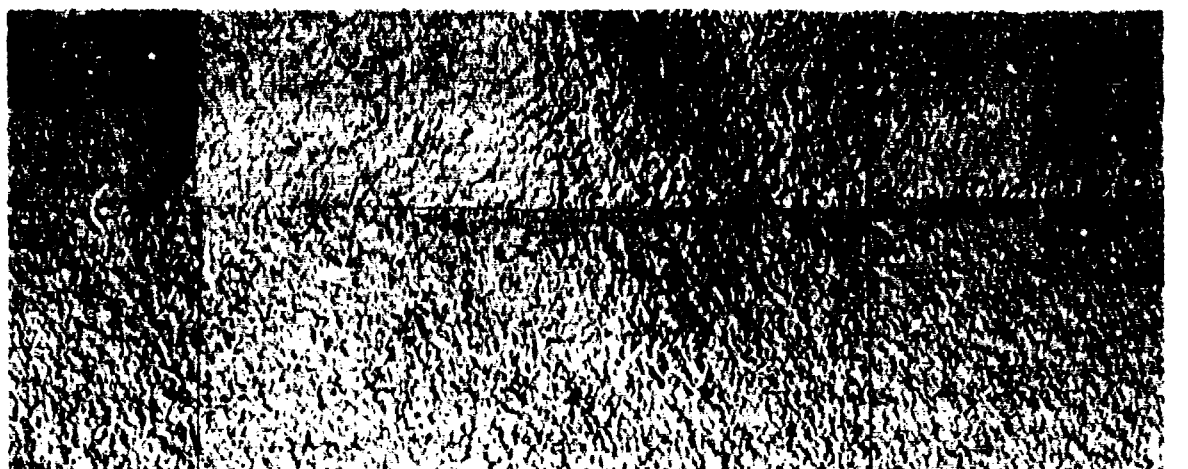
by the formation of superbands which crack, and this is shown in Figures 36 and 37. Figure 36(f) illustrates that the path of the final fracture corresponds with smaller cracks and bands present before the break occurred. Although relatively large  $\sim 2 \mu\text{m}$  slip offsets could be observed within the grains (Figure 38), the cracks responsible for fracture appear to be associated with large slip offsets at the grain boundaries. These offsets, which outline the grains on the initially smooth prepolished surface, and nucleate cracks are evident in Figure 37(b) and Figure 39.

#### 4. 7000-SERIES ALUMINUM ALLOYS

Results of plane strain ductility measurements derived mainly from double-bend tests are summarized in Figure 40 and Tables 3 and 4, together with yield strength and toughness values. The 7075-aluminum plate is one of three described by Kaufman, Nelson, and Holt<sup>(30)</sup> and has been studied by Ronald and Voss<sup>(31)</sup>. The bend specimens cut from this plate had the orientations shown in Figure 41. The 7075-aluminum alloy sheet is a standard commercial product. Alloy X was designed to have a small volume fraction of inclusions and intermediate particles, but its hardening behavior is otherwise similar to the 7075-alloy sheet and plate (see Figure 40). Alloy X did display a substantially larger grain size, and this facilitated the metallographic observations.

Taken together, Figure 40 and Tables 3 and 4 indicate a close connection between "plane strain" ductility and fracture toughness values, although an exact 1:1 correlation cannot be supported. Three of the four orientations of strips cut from the plate displayed variations of  $\bar{\epsilon}_{\text{PS}}$  with aging similar to the  $K_{\text{Ic}}$ -values<sup>†</sup> reported by Ronald and Voss<sup>(31)</sup>. The variations in  $\bar{\epsilon}_{\text{PS}}$ -values with orientation are not unlike the variations of the  $K_{\text{Ic}}$ -values obtained for the different orientations

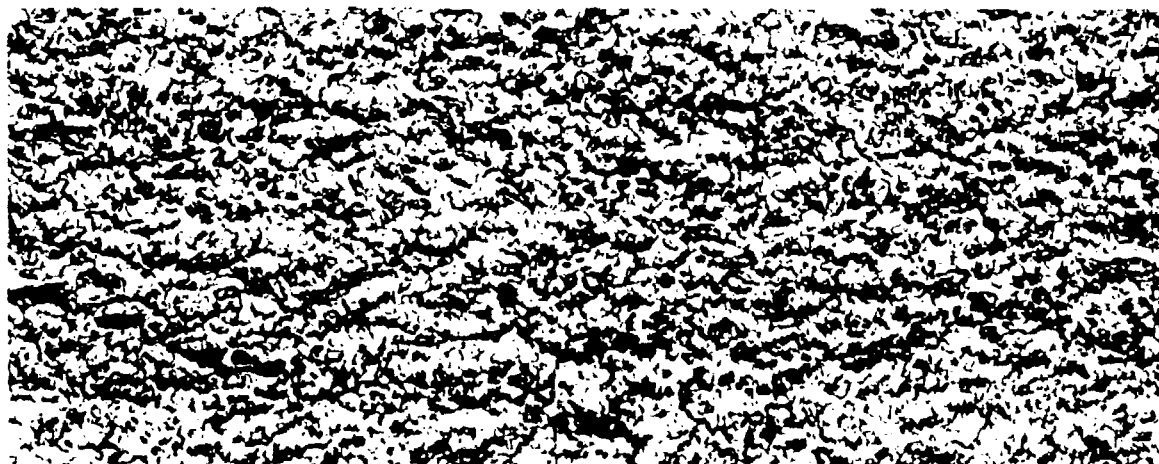
<sup>†</sup> Obtained from DCB specimens loaded in the weak, sheet transverse direction (load normal to the rolling plane and the crack in the rolling plane).



(a)  $\bar{\epsilon} = 0$



(b)  $\bar{\epsilon} = 0.04$

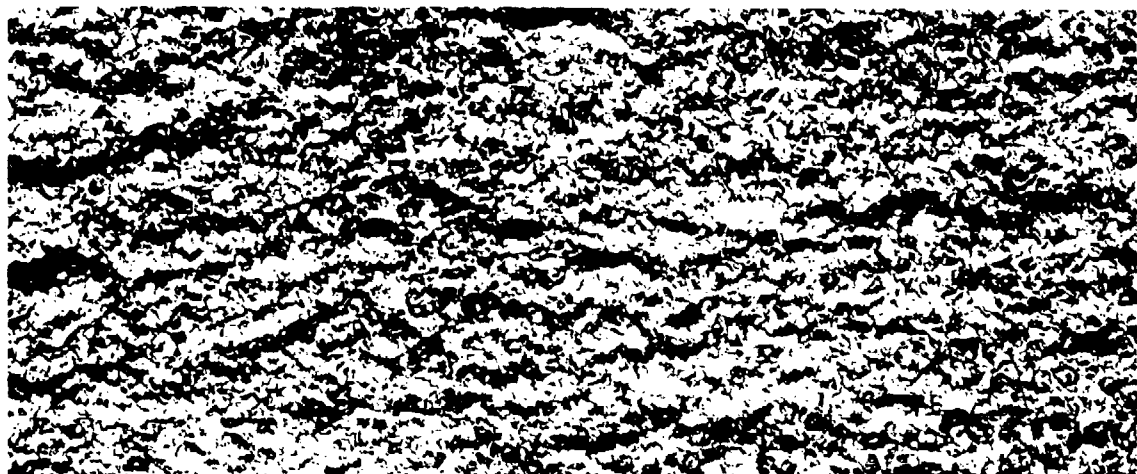


(c)  $\bar{\epsilon} = 0.12$

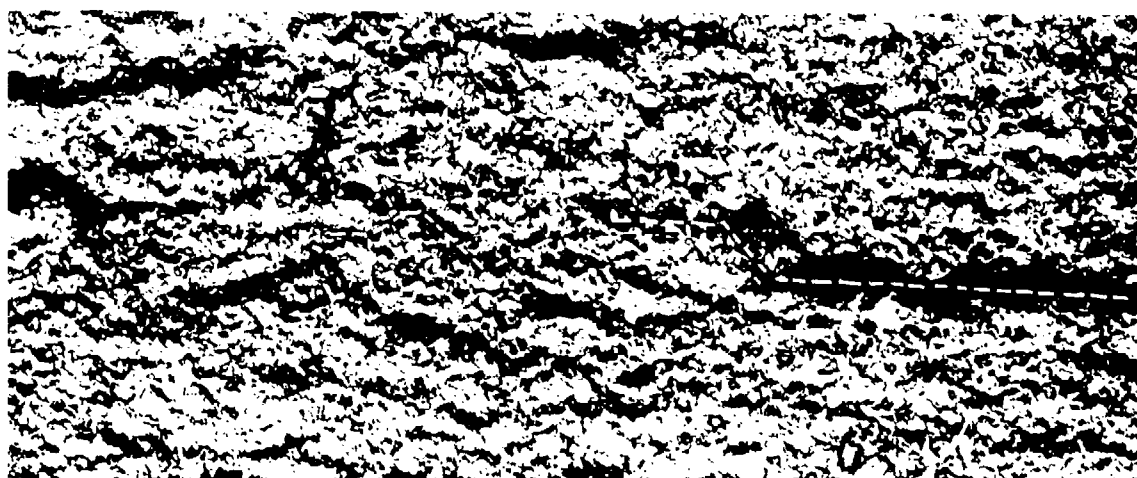
FIGURE 36. DEFORMATION MARKINGS ON THE SURFACE OF THE AGED Ti-6Al-4V BEND SPECIMEN. The photographs are of cellulose acetate replicas of the same region of the specimen after different amounts of strain: (a)  $\bar{\epsilon} = 0$ , (b)  $\bar{\epsilon} = 0.04$ , (c)  $\bar{\epsilon} = 0.12$ , (d)  $\bar{\epsilon} = 0.19$ , (e)  $\bar{\epsilon} = 0.24$ , and (f)  $\bar{\epsilon} = 0.30$ . The dashed line in (f) shows the location of the final rupture



(d)  $\bar{\epsilon} = 0.19$



(e)  $\bar{\epsilon} = 0.24$

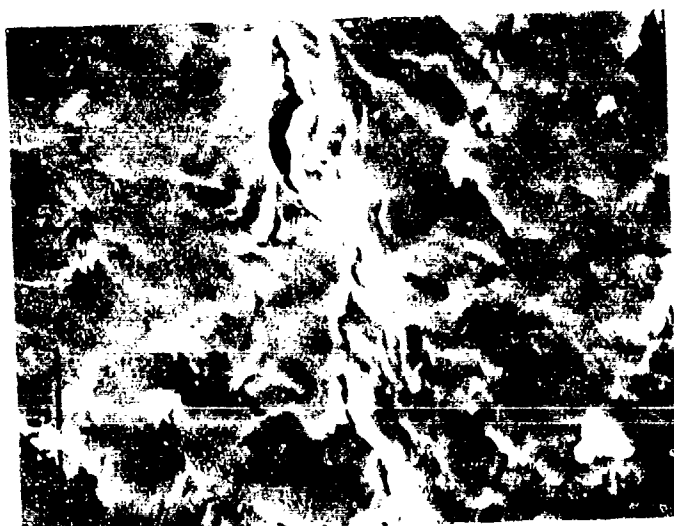


(f)  $\bar{\epsilon} = 0.30$

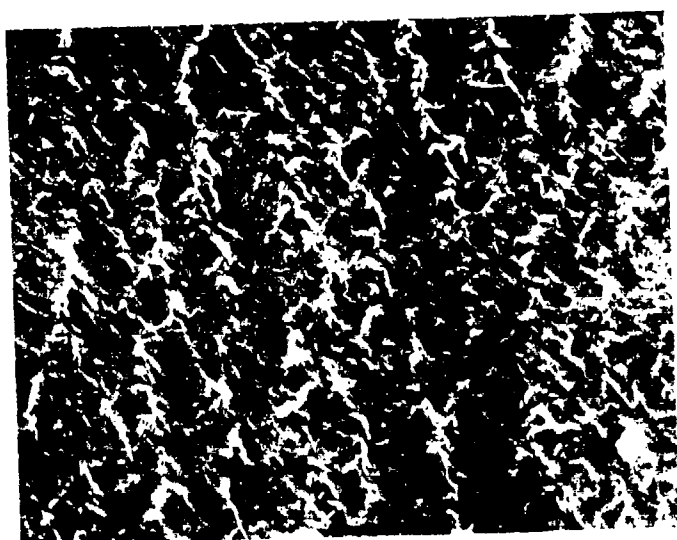
FIGURE 36. (Continued)



(a)

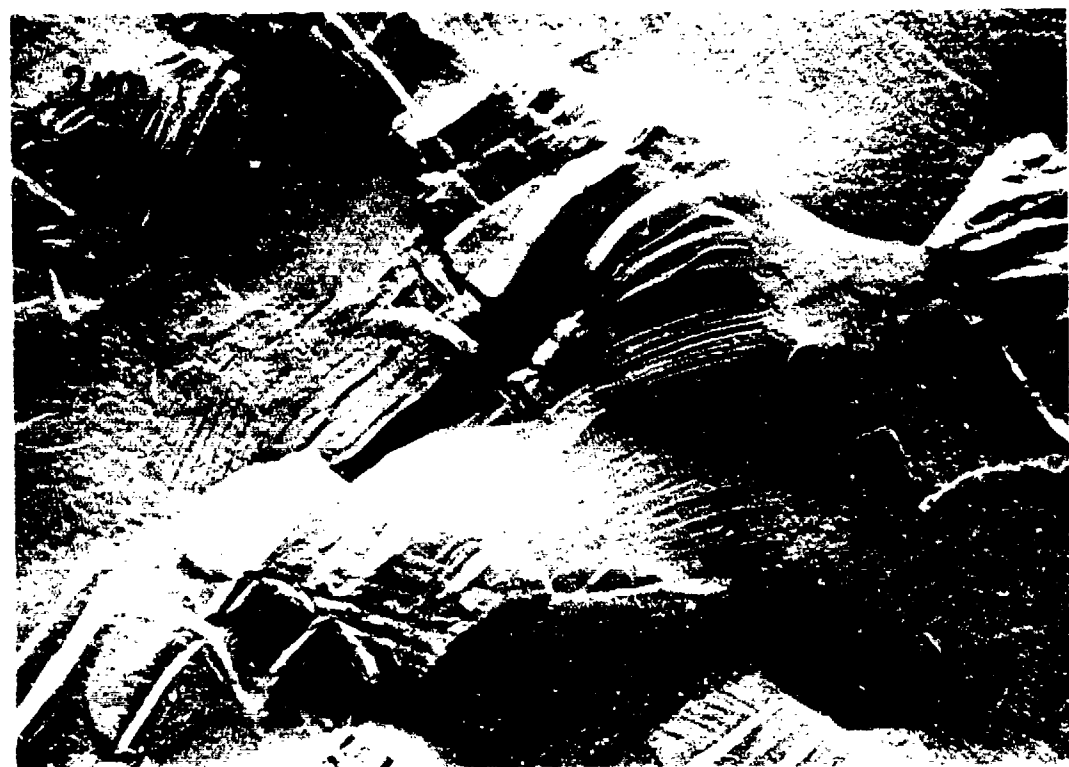


(b)



(c)

FIGURE 37. SEM MICROGRAPHS OF THE Ti-6Al-4V BEND SPECIMEN SURFACE  $\bar{\epsilon} = 0.36$ , SHOWING SLIP OFFSETS AND CRACKS AT THE BASE OF THE SLIP BANDS



(a)  $\bar{\epsilon}_1 = 23\%$



(b)  $\bar{\epsilon}_1 = 23\%$

FIGURE 38. SLIF MARKINGS ON THE SURFACE OF AGED Ti-6Al-4V BEND SPECIMENS,  $\bar{\epsilon}_1 = 0.23$  OBSERVED ON TRANSMISSION MICROGRAPHS OF CELLULOSE ACETATE REPLICAS



(c)  $\bar{\epsilon} = 29\%$



(b)  $\bar{\epsilon} = 29\%$



(a)  $\bar{\epsilon} = 29\%$

FIGURE 39. TRANSMISSION MICROGRAPHS OF CELLULOSE ACETATE REPLICAS OF THE SURFACE OF AGED Ti-6Al-4V BEND SPECIMENS.  
The photographs show slip offsets and fissures developing at the grain boundaries

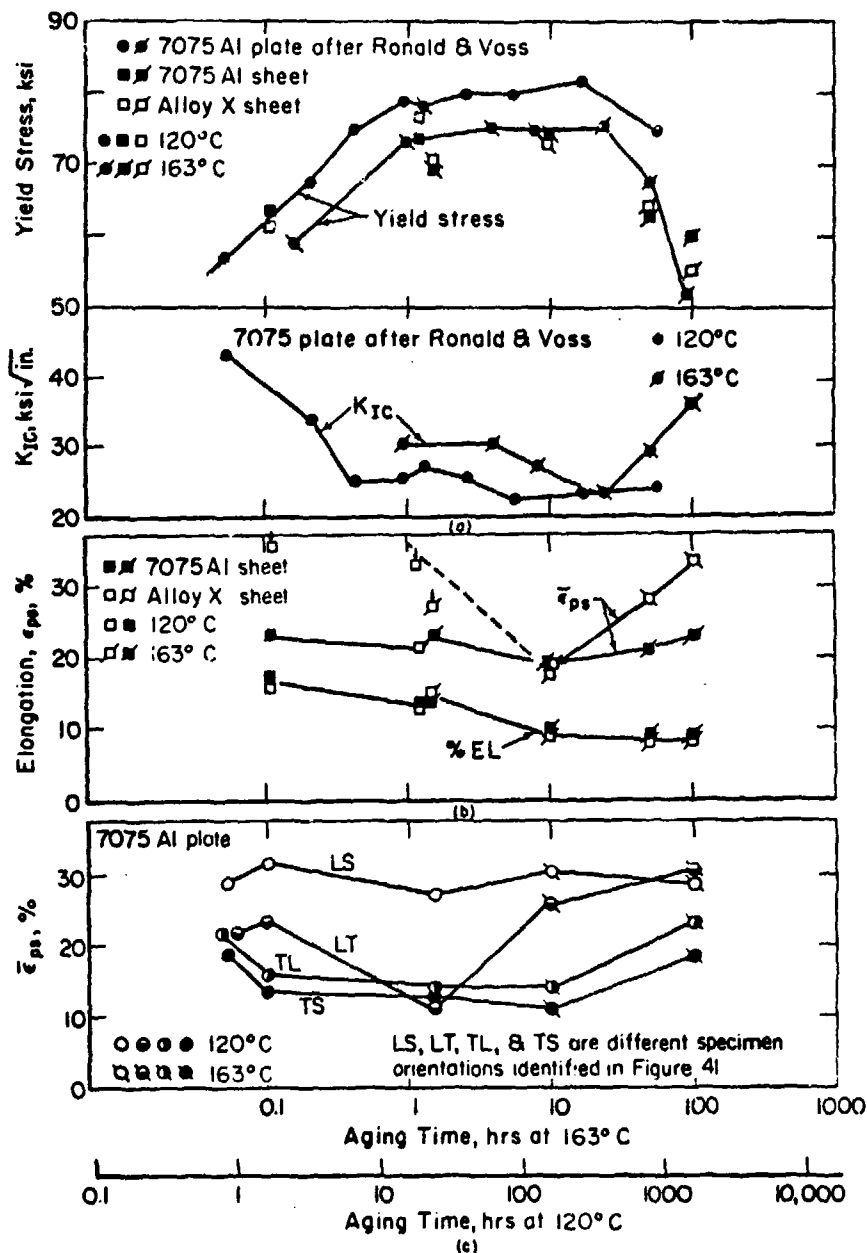


FIGURE 40. INFLUENCE OF AGING ON THE YIELD STRENGTH, FRACTURE TOUGHNESS, CONVENTIONAL AND "PLANE STRAIN" DUCTILITY VALUES FOR 7000-SERIES ALUMINUM ALLOYS. Double-bend specimens of the 7075 aluminum sheet and Alloy X sheet were cut with the long axis parallel to the rolling direction and a width/thickness ratio of 16.6. The double-bend specimens cut from the plate had the orientations shown in Figure 41, and a width to thickness ratio of 8.3. The orientation of the fracture toughness specimens of the 7075 Al alloy plate is SL

TABLE 3. ORDINARY TENSILE PROPERTIES, PLANE STRAIN DUCTILITY AND FRACTURE TOUGHNESS VALUES FOR 7075 ALUMINUM SHEET

Condition	$\sigma_Y$ $\text{MN/m}^{-2}$ (ksi)	$\sigma_{ULT}$ $\text{MN/m}^{-2}$ (ksi)	Uniform Elongation, %	$\bar{\epsilon}_{PS}$	$K_C$ , $\text{MN/m}^{-3/2}$
Undraged (a)	340 (50)	500 (73)	18.1	19.6	~0.23
Aged (b)	470 (67)	540 (78)	11.0	13.5	0.22
Peak Aged (c)	520 (75)	565 (82)	9.3	9.9	0.16

- (a) Solution treated at 485°C for 15 minutes, water quenched, and aged 1.5 hours at 120°C.
- (b) Solution treated at 485°C for 15 minutes, water quenched, and aged 24 hours at 120°C.
- (c) As received condition.
- (d) Load applied parallel to rolling direction; crack growth parallel to long transverse direction.
- (e) Load applied in the long transverse direction; crack growth parallel to rolling direction.

TABLE 4. FRACTURE TOUGHNESS AND "PLANE STRAIN" DUCTILITY VALUES FOR 7075 Al PLATE IN THE PEAK AGED CONDITION

SPECIMEN ORIENTATION		$K_{Ic}$ $MNm^{-3/2}$ (Ksi $\sqrt{in}$ )	$\bar{\epsilon}_{ps}$
Toughness (a)	Bend (b)		
Longitudinal (LT)	A	(d) (26.3) <sup>(d)</sup>	0.26
Transverse (TL)	B	(d) (22.6) <sup>(d)</sup>	0.14
Short Transverse (ST)	D <sup>(c)</sup>	(d) (23.0) <sup>(e)</sup>	0.12

- (a) Longitudinal: crack plane normal to plate rolling direction, crack growth parallel to plate-width direction; Transverse: crack plane and direction parallel to rolling direction; Short transverse: crack plane parallel to plane of the plate, crack direction parallel to width direction.
- (b) Orientations identified in Figure 41.
- (c) The orientation of the slip planes activated in D are comparable to those of the short transverse direction.
- (d) Kaufman, Nelson and Holt<sup>(30)</sup>.
- (e) Ronald and Voss<sup>(31)</sup>.

(see Table 4). The  $\bar{\epsilon}_{PS}$ -values for the 7075-sheet vary with aging like the  $K_c$ -values for the material (Figure 41, and Table 3). In contrast, elongation values for the 7075 and Alloy X sheet do not recover after overaging as the  $K_{Ic}$ -values do.

The distribution of slip on the surface of Alloy X bend specimens in various heat treated conditions is illustrated in Figures 42-47. The results of measurements of the distribution of plane strain deformation on the microscale are shown in Figure 48. Additional mechanical property data for these conditions are given in the footnote<sup>†</sup>. The microstructural observations may be summarized as follows:

- 1) The rupture of the aluminum Alloy X bend specimens proceeds in essentially the same manner as those of the 4340 and maraging steel. Deformation tends to become concentrated in superbands--collections of slip bands whose traces on the surface are normal to the principal stress axis--that extend over  $\sim 2000 \mu\text{m}$  ( $\sim 20$  grains). Cracks initiate at heavily slipped regions (coarse slip bands or sheared grain boundaries in the overaged samples of Alloy X) within the superbands. These cracks join, grow, and ultimately rupture the specimen. Figure 42 illustrates the main features of this process.
- 2) Figures 43 and 44 show the progressive development of superbands on replicas of the aged condition taken of the same region of the surface after different amounts of strain. Quantitative measurements taken from these replicas (see Figure 48b) indicate that the pattern of heterogeneous deformation is already apparent at a strain of 3%, which is less than the 9% necking strain in simple tension. These measurements show that the deformation is very unevenly distributed in the high strength, aged condition, but is essentially uniform when the same material is in the soft, as-solution treated condition (see Figures 45 and 48) or in the heavily overaged condition (see Figure 48).
- 3) Figures 44(e) and 44(f) illustrate that the fracture path is transgranular and roughly parallel to the pattern of coarse slip bands within

<sup>†</sup>

PROPERTIES OF ALLOY X-SHEET							
Condition	Yield Stress MNm <sup>-2</sup> (Ksi)	Ultimate Stress MNm <sup>-2</sup> (Ksi)	Uniform Elonga- tion %	7 <sub>EL</sub>	7 <sub>RA</sub>	Plane Strain <sup>(a)</sup>	Ductility
Solution treated 15 min at 485°C and WQ	50 (7)	170 (24)	43	45	-	-	-
Aged 24 hrs. at 120°C	500 (73)	560 (81)	9	15	49	0.15	
Overaged 24 hrs. at 350°C	170 (25)	370 (53)	17	19	34	0.22	

(a) Measured with the Clausing "plane strain" tension specimen.

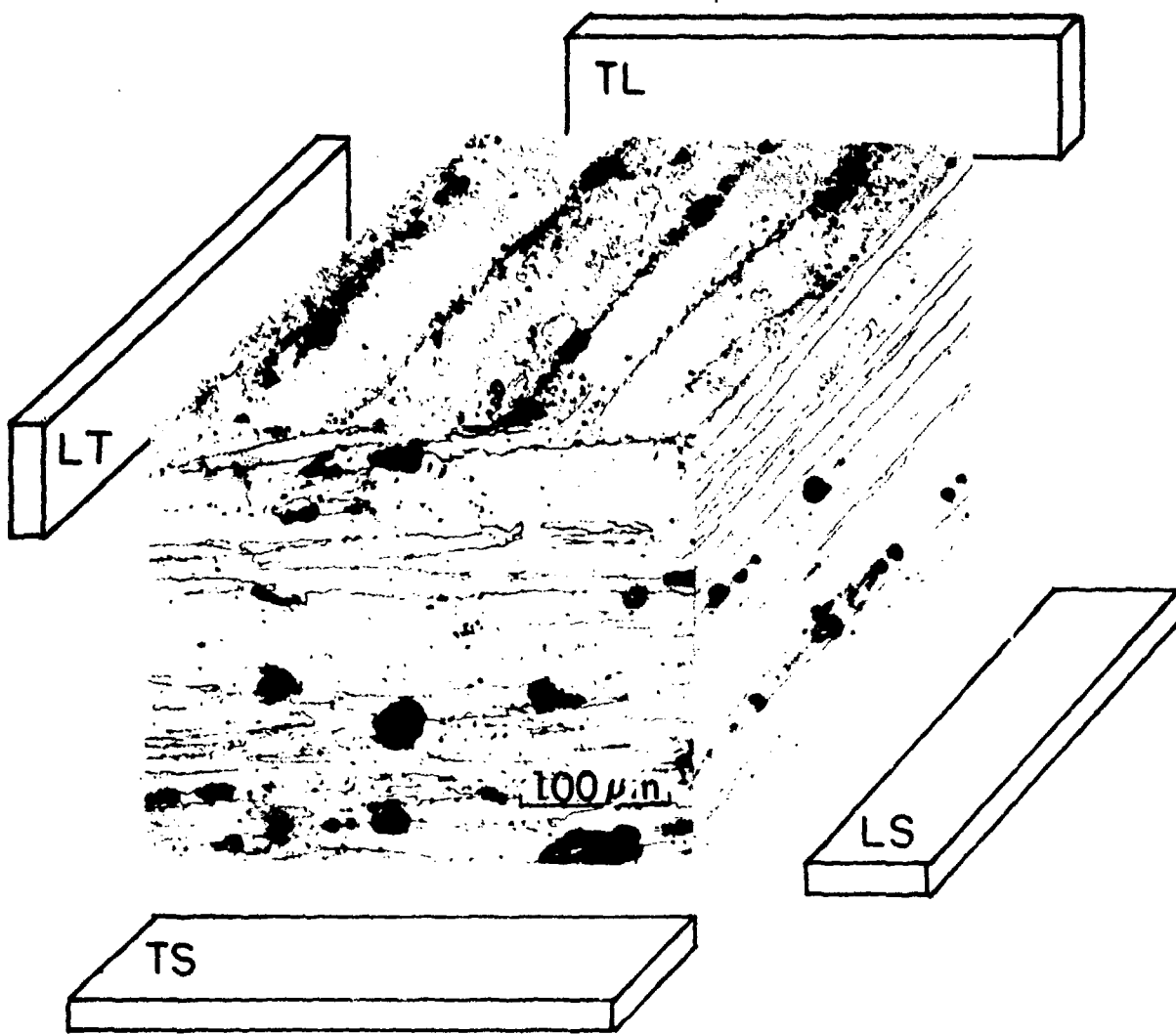
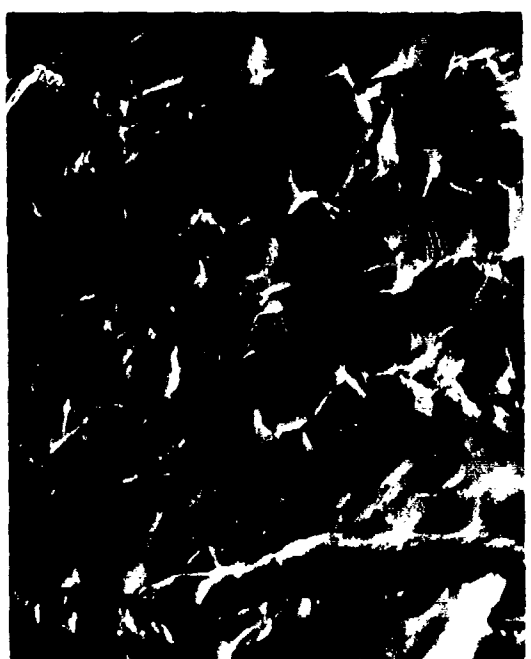


FIGURE 41. ORIENTATION OF "PLANE STRAIN" DOUBLE-BEND SPECIMENS CUT FROM THE 7075-ALUMINUM ALLOY PLATE. The letters L, T and S stand for longitudinal- (or rolling-), transverse- and short transverse- (or thickness-) direction, respectively. The first letter identifies the direction of the maximum tension stress axis of the bend specimen, the second the direction of crack extension in the bend specimen.



(a)



(b)



(c)



(d)

FIGURE 42. SCANNING IN ELECTRON MICROGRAPHS OF "PLANE STRAIN" DEFORMATION OBSERVED ON THE SURFACE OF A PLASTICALLY BENT STRIP OF ALUMINUM ALLOY X IN THE PEAK AGED CONDITION: (a) example of super band (arrows), (b) close-up of deformation within super band, (c) coarse slip band in the crack nuclei at its base, and (d) view of failure surface of sheared super band showing large and small dimples. The long direction of the bent strip is vertical.

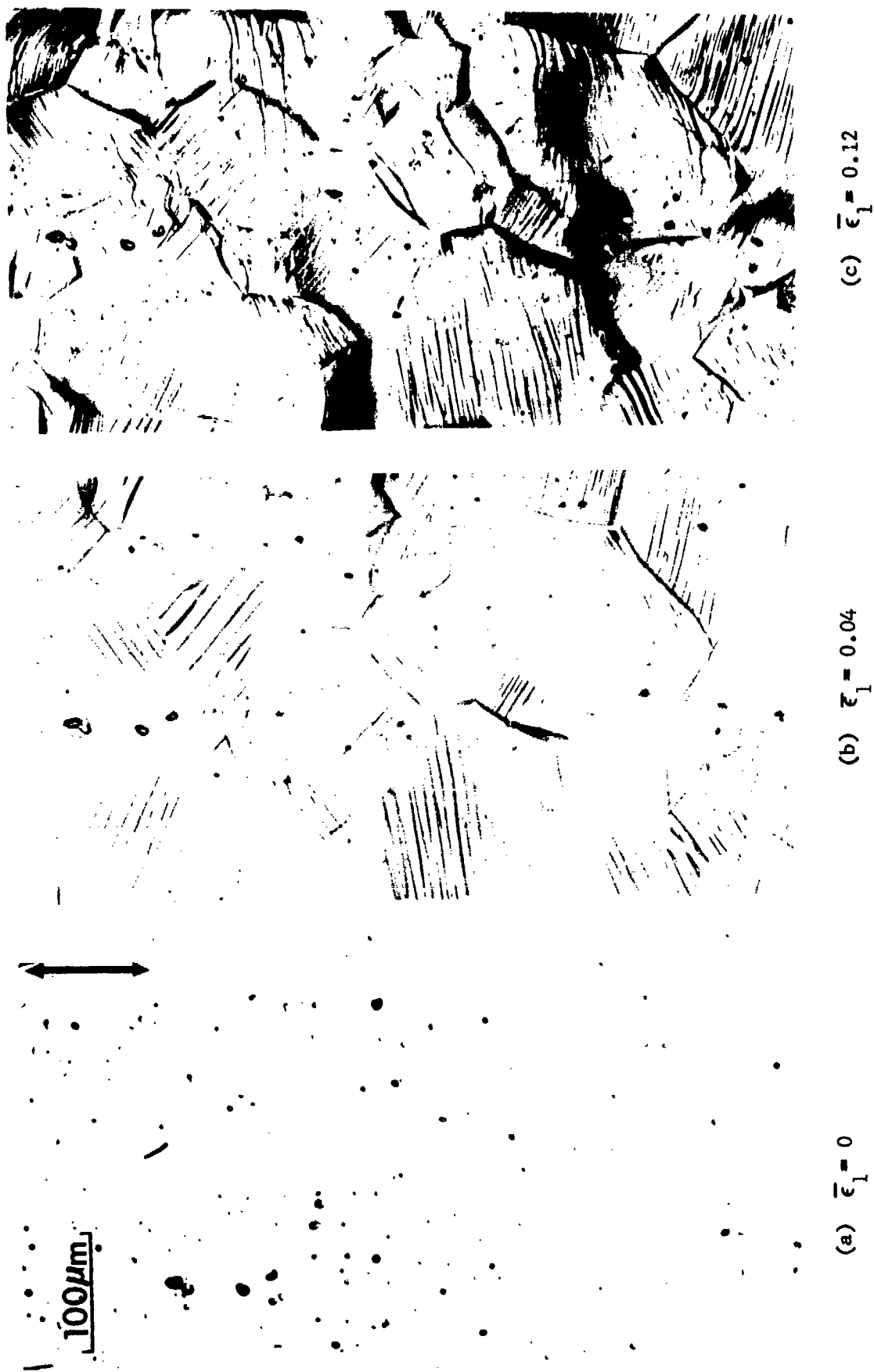


FIGURE 43. DEFORMATION MARKINGS ON THE SURFACE OF ALUMINUM ALLOY X "PLANE STRAIN" BEND SPECIMENS IN THE AGED CONDITION. The photographs are of cellulose acetate replicas of the same region after different amounts of strain: (a)  $\bar{\epsilon} = 0$ , (b)  $\bar{\epsilon}_1 = 0.04$ , (c)  $\bar{\epsilon}_1 = 0.12$ ,  $\bar{\epsilon}_1 = 0.23$ , (d)  $\bar{\epsilon}_1 = 0.26$ , and (e)  $\bar{\epsilon}_1 = 0.35$ . The arrow in Figure (a) shows the principal  $\{\bar{\epsilon}_1\}$  strain direction, width-to-thickness ratio = .

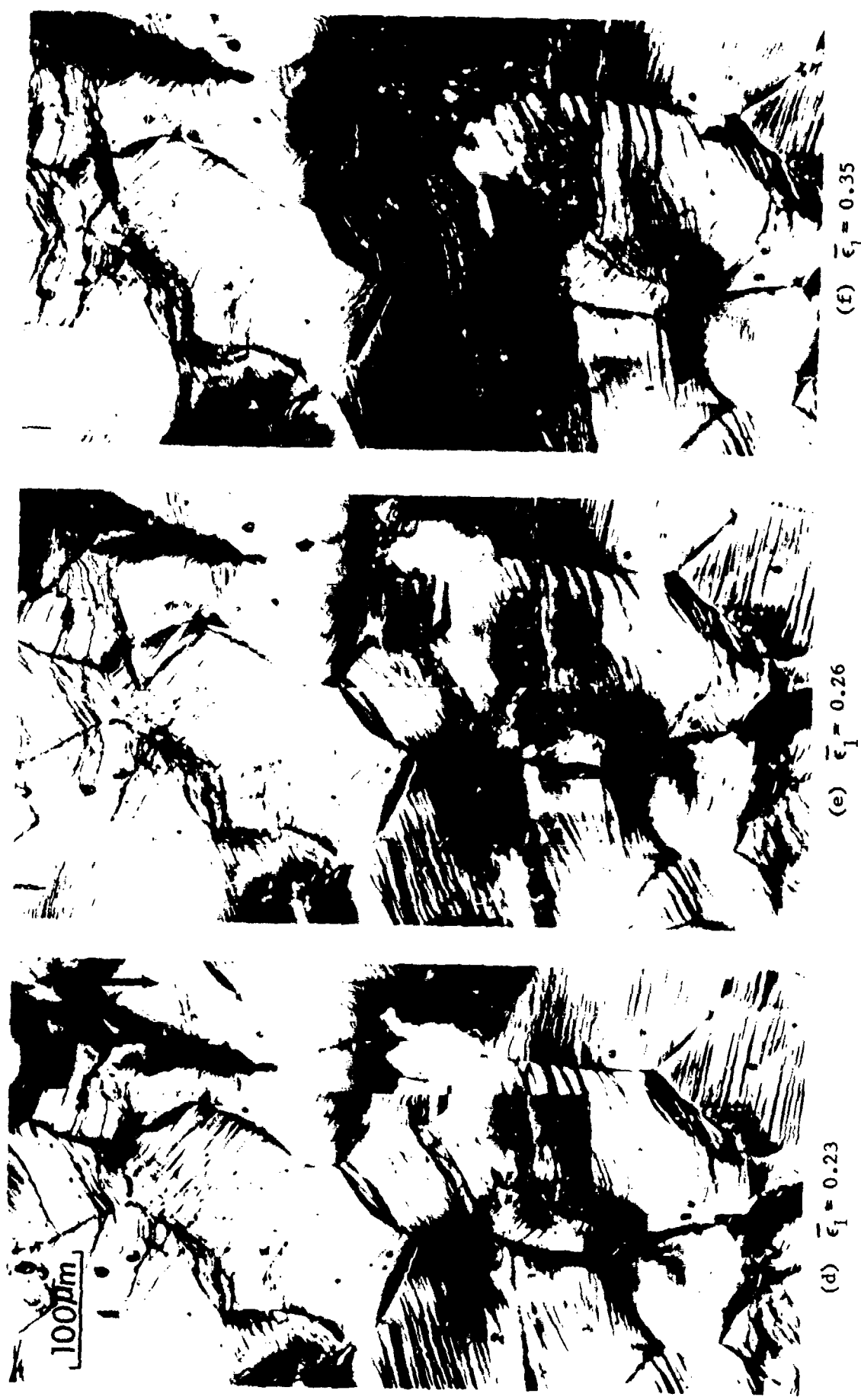


FIGURE 43. (Continued)



FIGURE 44. CLOSE-UP OF THE DEVELOPMENT OF A SUPER BAND ON THE SURFACE OF AN ALUMINUM ALLOY X BEND SPECIMEN IN THE PEAK AGED CONDITION: (a)  $\bar{\epsilon}_1 = 0.09\%$ , (b)  $\bar{\epsilon}_1 = 0.12\%$ , (c)  $\bar{\epsilon}_1 = 0.18\%$ , (d)  $\bar{\epsilon}_1 = 0.26\%$ , and (f)  $\bar{\epsilon}_1 = 0.35\%$ . The arrow in Figure (d) points to a feature that looked like an inclusion particle just below the surface. The letters in (e) and (f), which identify common features on the two photographs, provide a basis for locating the path of the fracture (see dashed line in (e)). The arrow in Figure (a) shows the principal  $\bar{\epsilon}_1$  - strain direction



(c)  $\bar{\epsilon}_1 = 0.18$



(d)  $\bar{\epsilon}_1 = 0.18$

FIGURE 44. (Continued)



(e)  $\bar{\epsilon}_1 = 0.26$



(f)  $\bar{\epsilon}_1 = 0.35$

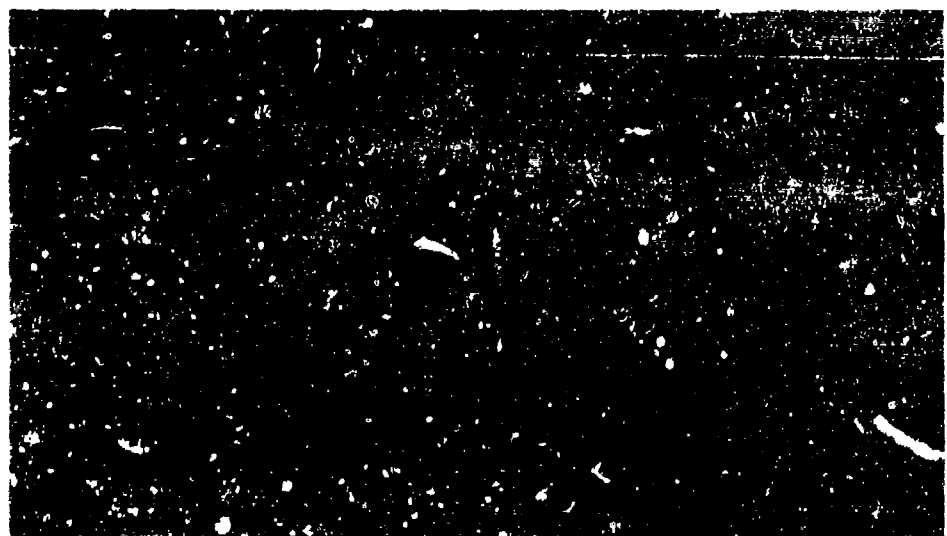
FIGURE 44. (Continued)



(a)  $\bar{\epsilon}_1 = 0$



(b)  $\bar{\epsilon}_1 = 0.22$



(c)  $\bar{\epsilon}_1 = 0.39$

FIGURE 45. DEFORMATION MARKINGS ON THE SURFACE OF ALUMINUM ALLOY X "PLANE STRAIN" BEND SPECIMENS IN THE AS-SOLUTION TREATED. The photographs are of cellulose acetate replicas of the same region after different amounts of strain: (a)  $\bar{\epsilon}_1 = 0$ , (b)  $\bar{\epsilon}_1 = 0.22$ , and (c)  $\bar{\epsilon}_1 = 0.39$ . The numbers on the photographs identify individual grains that appear on all three replicas. The arrow in Figure (a) shows the principal  $\bar{\epsilon}_1$ -strain direction



FIGURE 46. DEFORMATION MARKINGS ON THE SURFACE OF OVERAGED ALLOY Y "PLANE-STRAIN" DOUBLE-BEND SPECIMEN.  $\epsilon_{ps} = 0.19$ . The micrograph shows superbands and intergranular cracks. WQ and aged 4 hrs at  $120^\circ\text{C}$  and 10 hrs at  $163^\circ\text{C}$



(a)

FIGURE 47. OPTICAL MICROGRAPHS OF THE SURFACE OF A PLANE STRAIN BEND SPECIMEN OF A 7000-SERIES ALUMINUM ALLOY X) IN THE OVERAGED CONDITION;  
 $\bar{\epsilon}_{PS} = 0.22$ : (a) portion of a super-  
band showing grain boundary ruptures  
(arrows) and (b) other examples of  
grain boundary ruptures. WQ and aged  
4 hrs at 120°C and 10 hrs at 163°C



(b)

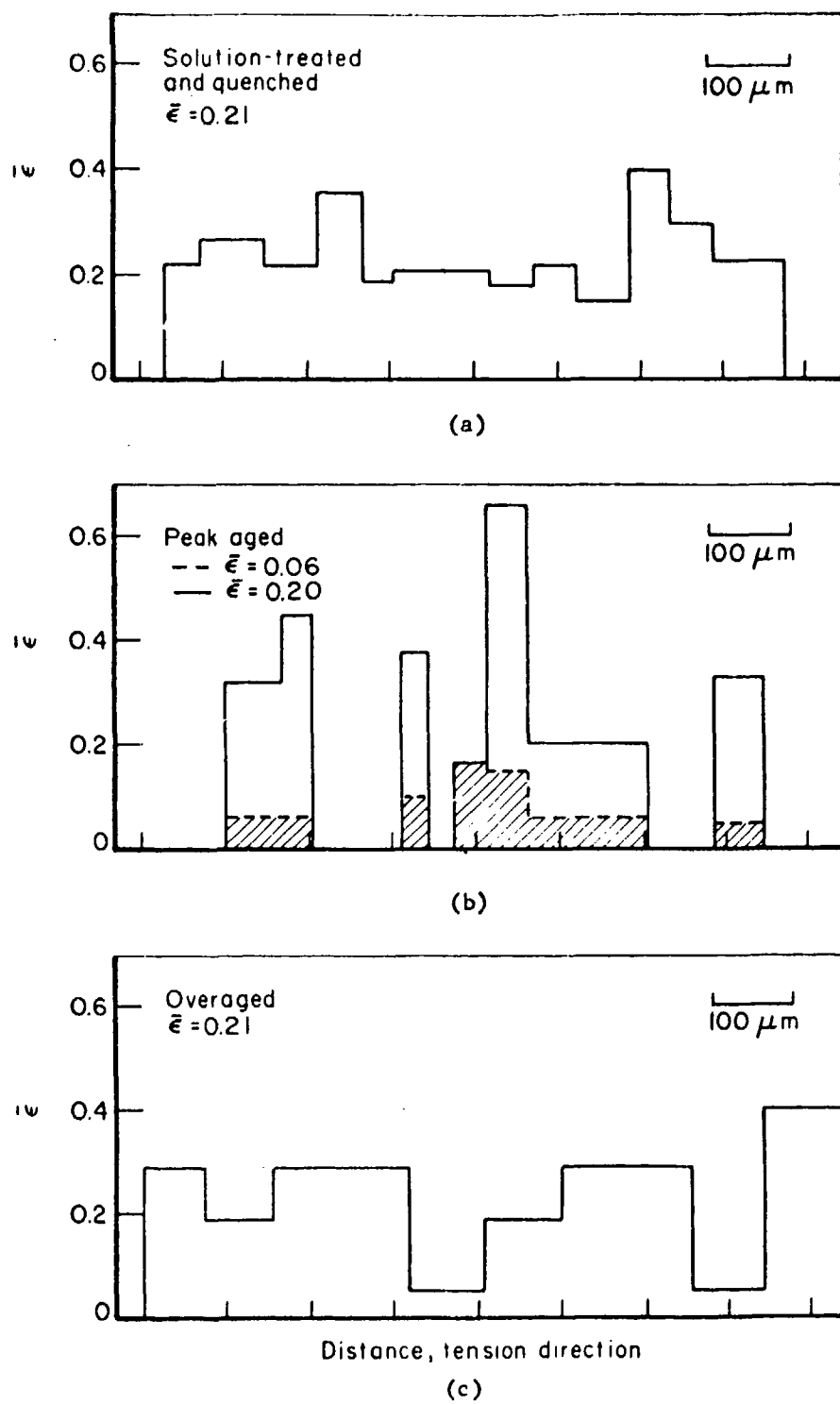


FIGURE 48. INFLUENCE OF HEAT TREATMENT ON THE PLASTIC STRAIN DISTRIBUTION ON THE MICROSCALE FOR "PLANE STRAIN" DEFORMATION. The true strain measurements were derived from replicas of the type shown in Figure 14, taken on the surface of plastically bent strips of a 7000-type alloy (Alloy X): (a) solution treated and quenched condition, (b) the peak aged condition shown in Figures 13 and 14, and (c) overaged. The average grain boundary intercept is 90  $\mu\text{m}$ . Mechanical properties of the 3 conditions are summarized in the Table in the footnote on p. 65.

the grains. Higher magnification electron micrographs showed that the deformation of the aged condition had two distinct components, (a) coarse slip and (b) fine slip, as shown in Figure 49. Cracks invariably initiated at the base of the coarse slip bands with  $\sim 2 \mu\text{m}$ - $4\mu\text{m}$  offsets (see Figures 50 and 51). Figure 44 provides little evidence that crack initiation in this alloy is assisted by inclusions visible on the surface. Figure 44(a) shows a feature near a triple point that may be subsurface inclusion.

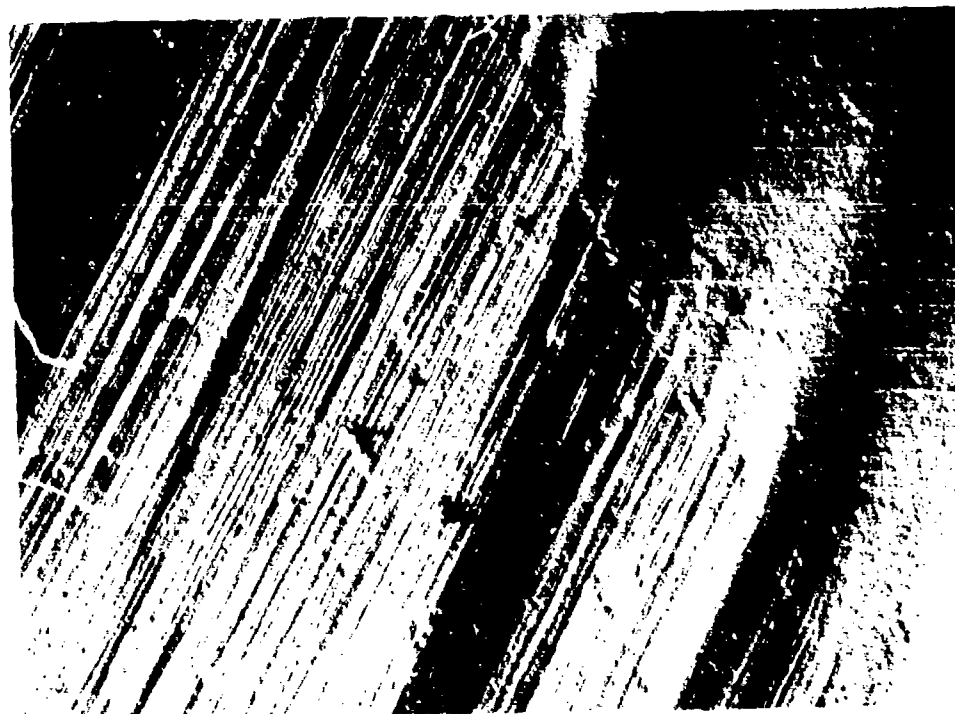
- 4) The large reduction in plane strain ductility that accompanies the over-aging of Alloy X (see Figure 40) is associated with a change in mechanism of cracking. As shown in Figures 45 and 46, prominent superbands are visible in the overaged material, but the cracks are mainly intergranular.

Micrographs of the surface "plane strain" bend specimens of the 7075-sheet alloy (see Figure 52(a), (d), and (e)) display prominent superbands. Compared with Alloy X (Figure 42), the commercial alloy displays a finer and indistinct grain structure and many more inclusion particles. Higher magnification pictures (Figures 51(a), 52(b), (c), (f), and (g)) reveal that the cracks are initiated at the base of prominent bands whose traces on the surface are normal to the maximum principal stress direction (the y-direction in Figure 4). Because the cracks are essentially straight, transgranular, and normal to the tensile axis, the cracked slip bands bear a superficial resemblance to cleavage microcracks in mild steel. (32) In contrast to Alloy X, the overaged 7075-sheet alloy specimens were not embrittled and did not display obvious grain boundary cracks (see Figures 52(f) and (g)). However, the slip bands were frequently associated with ruptured inclusions on the surface (see Figures 51(b), 52(c), and 52(f)).

The 7075-alloy plate material exhibited the characteristic lath-like grain structure shown in Figure 41 with average grain length, width, and thickness of  $540 \mu\text{m}$ ,  $122 \mu\text{m}$ , and  $15 \mu\text{m}$ . The "plane strain" ductility of the plate depended strongly on the orientation of the test coupons, as summarized



(a)  $\bar{\epsilon} = 23\%$

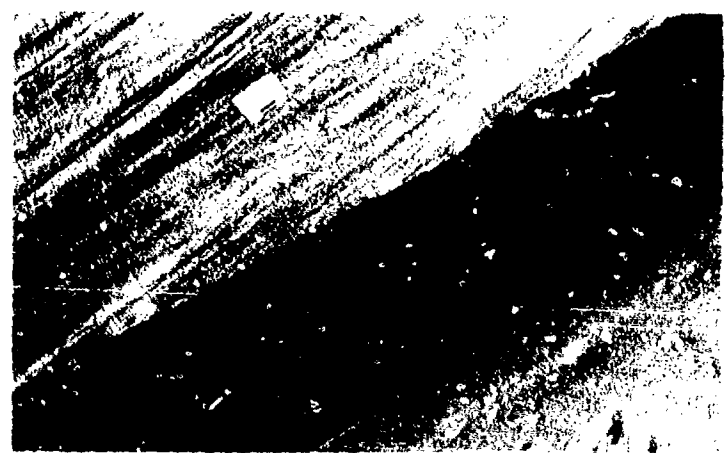


(b)  $\bar{\epsilon} = 23\%$

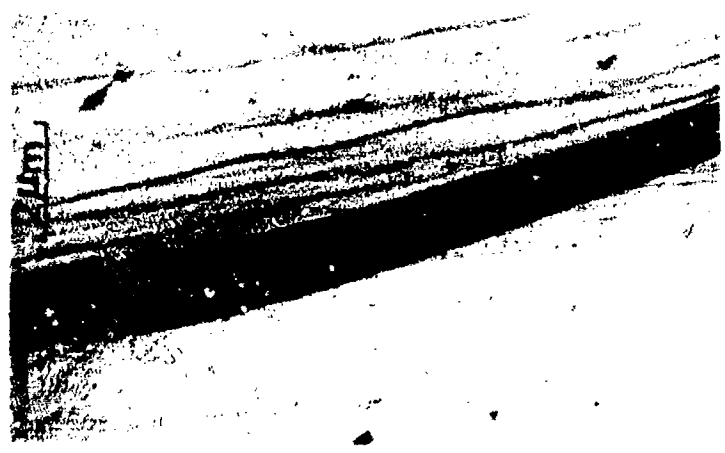
FIGURE 49. SLIP STEPS ON THE SURFACE OF THE AGED ALLOY X-BEND SPECIMENS, STRAINED  $\bar{\epsilon}_1 = 0.23$ , OBSERVED ON TRANSMISSION MICROGRAPHS OF 2-STAGE CELLULOSE ACETATE REPLICAS: (a) coarse slip offsets and (b) fine slip



(a)  $\bar{\epsilon}_1 = 23\%$



(b)  $\bar{\epsilon}_1 = 23\%$



(c)  $\bar{\epsilon}_1 = 23\%$

FIGURE 50. LARGE SLIP OFFSETS ON THE SURFACE OF AGED ALLOY X END SPECIMENS STRAINED  $\bar{\epsilon}_1 = 0.23$  OBSERVED ON TRANSMISSION MICROGRAPHS OF CELLULOSE ACETATE REPLICAS: (a) and (b) show slip offsets, and (c) shows a slip offset with a crack at its base



(b)



(a)

FIGURE 51. EXAMPLES OF COARSE SLIP BANDS: (a) Alloy X in the peak aged condition, and (b) 7075-T6 Alloy. The small tongue at the base of the slip band in (a) is a sign a crack nucleus has formed.

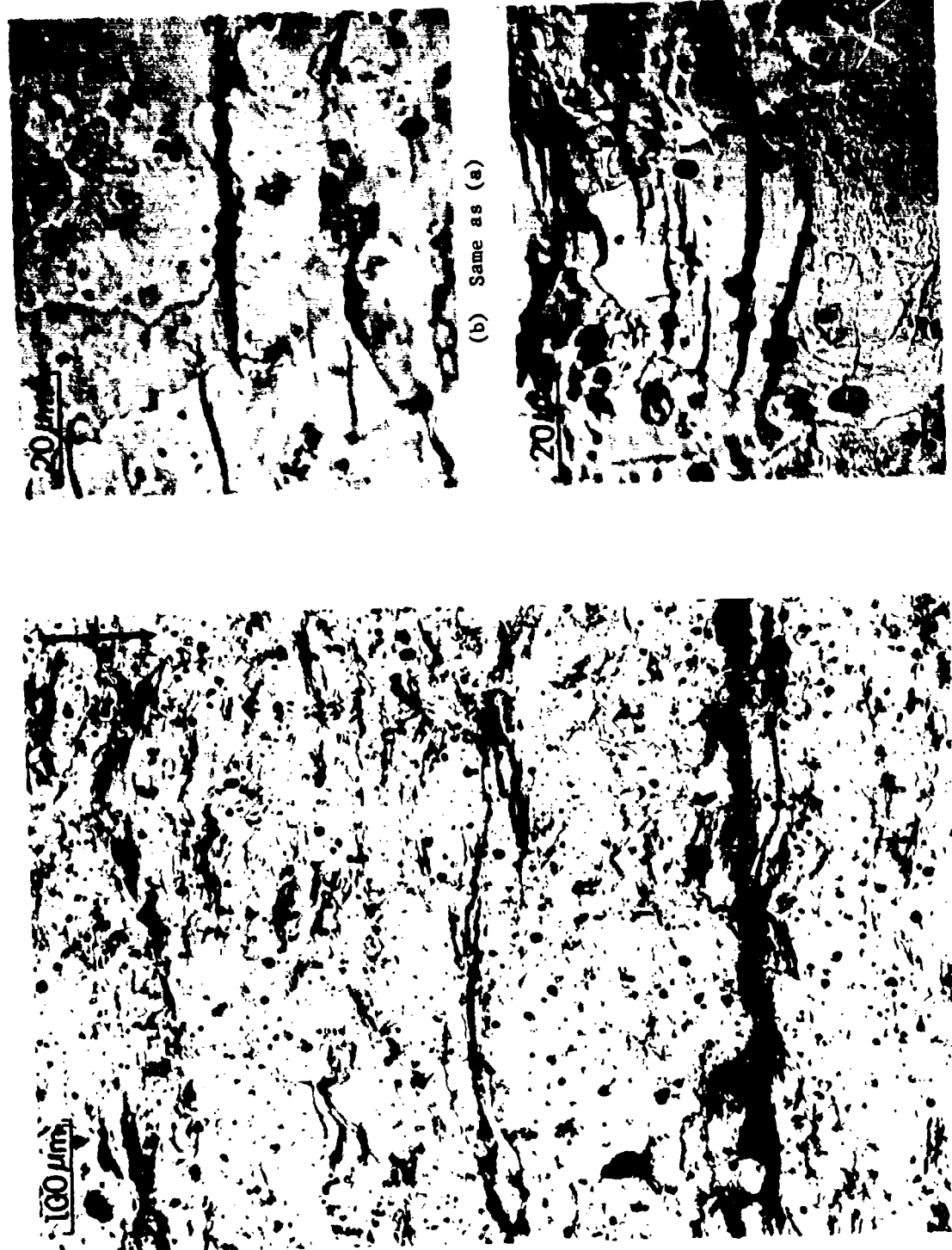
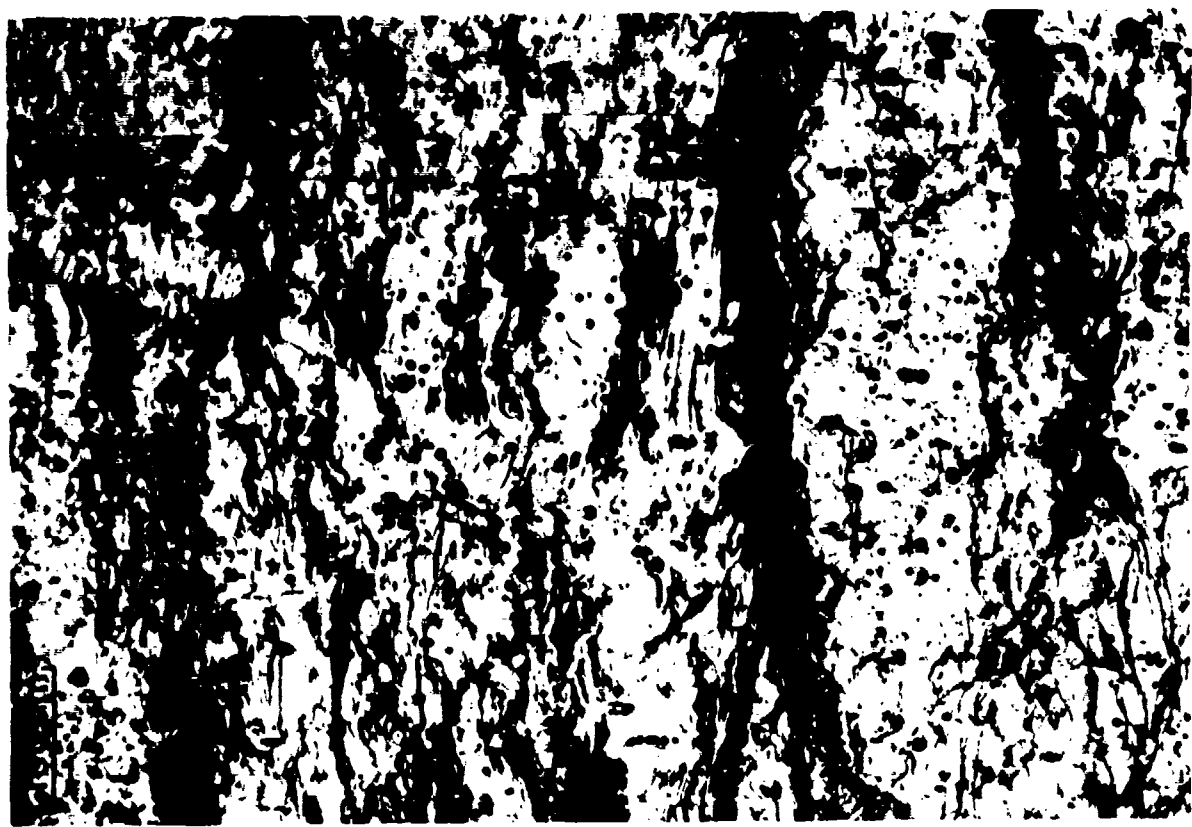


FIGURE 52. MICROGRAPHS OF THE SURFACE OF 7075 ALUMINUM ALLOY SHEET "PLANE-STRAIN" DOUBLE-BEND SPECIMENS:  
 (a) as received condition  $\bar{\epsilon}_{PS} = 0.16$ , (b) and (c) higher magnification of slip bands on (a);  
 (d) same material solution treated 20 min. at 485°C, WQ and aged 24 hrs at 120°C,  $\bar{\epsilon}_{PS} = 0.22$ ,  
 (e) same as (d) except WQ and overaged 4 hrs at 120°C and 10 hrs at 163°C;  $\bar{\epsilon}_{PS} = 0.19$ , (f) and  
 (g) show higher magnification of slip bands on (e). The arrows show the principal,  $\epsilon_1$ -strain  
 direction.



(d) Aged,  $\bar{\epsilon}_{PS} = 0.22$



(e) Overaged,  $\bar{\epsilon}_{PS} = 0.19$

FIGURE 52. (Continued)



(f) Same as (e)



(g) Same as (e)

FIGURE 52. (Continued)

in Figure 40(c). The micrographs of the fractured double-bend specimens reproduced in Figure 53 show there is a connection between the plane strain ductility values and the grain structure:

LT-Orientation. Coupons of the LT-orientation displayed the highest ductility values, and these were substantially independent of aging condition. The micrographs of the surface (Figures 53(a) and (b) show that the extent of the slip bands, which traverse the small, grain thickness dimension, is strongly limited by the grain boundaries. As a consequence, both the slip-band offsets and cracks produced by these slip bands remain relatively small compared with the slip bands of the sheet alloy (compare Figures 53(e) and (b) with Figures 51(b), 52(b), (c), (f), and (g), particularly in the light of the larger amount of strain imposed on the LT-condition). Ultimately, the bands do extend across the boundaries (see array #1 in Figure 53(b)), producing a superband-like array and large slip offsets. Figure 54 illustrates that the slip bands are similar in appearance to those in the Alloy X (see Figures 50 and 51). In both cases cracked bands with offsets of  $\sim 4\text{-}6 \mu\text{m}$  are evident. In the 7075 alloy plate, many of the individual slip bands are associated with ruptured inclusions.

TL-Orientation. Specimens of the TL-orientation with a grain structure very similar to the LT-orientation (see Figures 41, and 53(c) and (d)) displayed much lower ductility values. In this case the  $\bar{\epsilon}_{ps}$ -values vary with aging very much like the  $K_{Ic}$ -values for the plate. Here too, the extent of the slip bands is strongly limited by the longitudinal boundaries. However, much longer cracks are apparent at a much smaller strain. The reason for this may be connected with the inclusion particles which tend to be concentrated at the grain boundaries. A number of the slip bands in Figure 53(d) are clearly associated with ruptured particles in the longitudinal boundaries. There is also a hint that portions of the long cracks are ruptured transverse boundaries, whose frequency is



(a) LT, 25 hrs at 120°C,  $\bar{\epsilon}_{PS} = 0.26$



(b) Close-up of (a)

FIGURE 53. MICROGRAPHS OF THE SURFACE OF 7075-ALUMINUM ALLOY PLATE "PLANE-STRAIN" DOUBLE-BEND SPECIMENS:

(a) and (b) LT-orientation, aged 25 hrs at 120°C,  $\bar{\epsilon}_{PS} = 0.26$ , (c), and (d) TL-orientation aged 25 hrs at 120°C,  $\bar{\epsilon}_{PS} = 0.11$ , (f) LT-orientation aged 25 hrs at 120°C,  $\bar{\epsilon}_{PS} = 0.14$ , (e) LS-orientation, aged 25 hrs at 120°C,  $\bar{\epsilon}_{PS} = 0.11$ , (g) TS-orientation aged 25 hrs at 120°C,  $\bar{\epsilon}_{PS} = 0.12$ , and (h) TS-orientation aged 100 hrs at 163°C,  $\bar{\epsilon}_{PS} = 0.17$ . The principal,  $\bar{\epsilon}_1$ -strain direction is indicated in (a). Width-to-thickness ratio = 8.3. Arrows show principal,  $\bar{\epsilon}_1$ -strain direction.



FIGURE 53. (Continued)



FIGURE 53. (Continued)



(f) LS, 100 hrs at 163°C,  $\bar{\epsilon}_{PS} = 0.29$



(e) LS, 25 hrs at 120°C,  $\bar{\epsilon}_{PS} = 0.11$

FIGURE 53. (Continued)



(g) TS, 25 hrs at 120°C,  $\bar{\epsilon}_{\text{PS}} = 0.12$

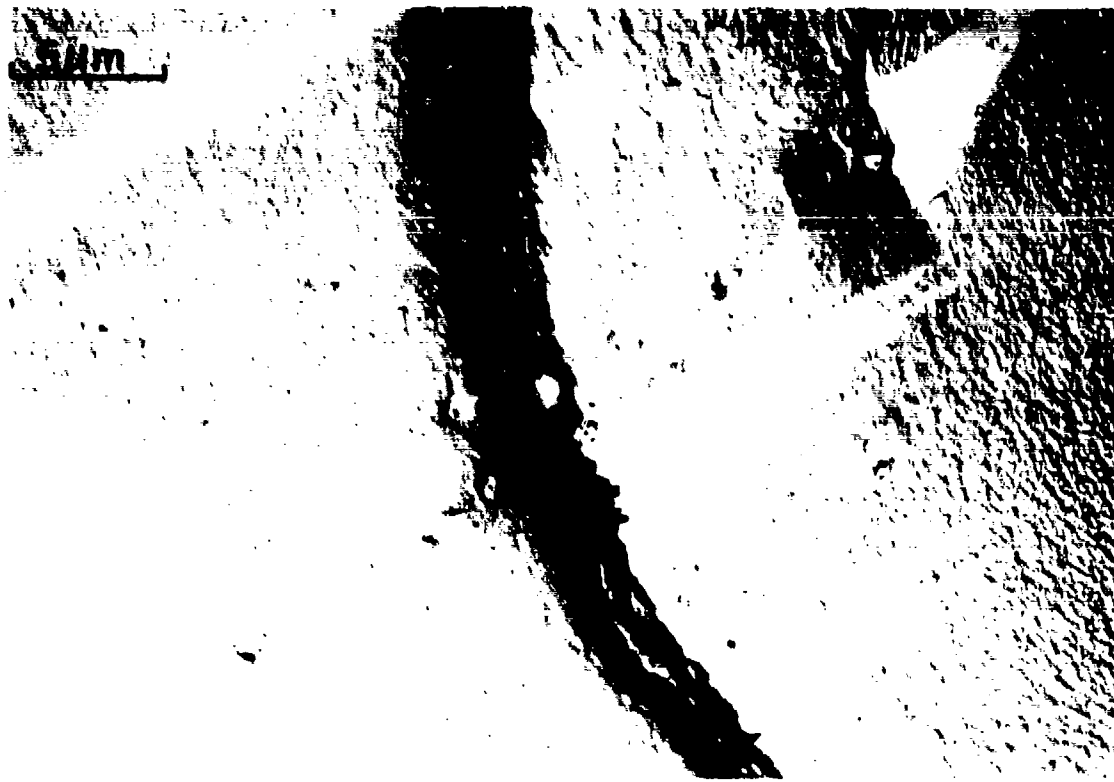


(h) TS, 100 hrs at 163°C,  $\bar{\epsilon}_{\text{PS}} = 0.17$

FIGURE 53. (Continued)



(a)



b)

FIGURE 54. LARGE SLIP OFFSETS ON THE SURFACE OF FRACTURED 7075-ALLOY PLATE LT-ORIENTATION BEND SPECIMENS  $\bar{\epsilon}_{ps} = 0.26$  OBSERVED ON CELLULOSE ACETATE REPLICAS: (a) slip bands and (b) slip offset with cracks at its base

twenty-four times as great\* in the TL-orientation as in the LT-orientation. It is therefore possible that the greater tendency for cracking is associated with the higher incidence, weak transverse boundaries. Other evidence of weak boundaries is discussed in paragraph on TS-orientation which follows.

LS-Orientation. The micrographs of the LS-orientation show superbands similar in appearance to those of sheet alloy (compare Figures 53(e) and (f) with Figures 52(a), (d), and (e)). In contrast to the LT-orientation, the slip bands traverse the grain width, which is twenty-eight times the thickness. The longitudinal boundaries do not appear to be effective obstacles to these longer slip bands. As a result, longer cracks are in evidence. Figures 3(e) and (f) illustrate the effect of overaging, which produces a threefold increase in  $\bar{\epsilon}_{ps}$  in this case. The nature of the slip bands does not seem to be altered by overaging; however, much more deformation is evident on the surface. It appears that the slip bands are more stable and more resistant to cracking in the overaged condition.

TS-Orientation. Micrographs of the TS orientation, which displayed the lowest  $\bar{\epsilon}_{ps}$ -values (see Figure 40), are reproduced in Figures 53(g) and (h). The slip bands appear "ragged" and are not as well defined as in the other orientation. The bands and cracks are "ragged" because they involve inclusion particles at the grain boundaries, and enforce the view that the slip and cracking in this orientation is intergranular. It appears that the longitudinal grain boundaries are relatively weak, and this tends to support the suggestion, made early, about weak transverse boundaries.

---

\* The grain length-to-width ratio.

## SECTION IV

### DISCUSSION

There is much common ground among high strength alloys. The  $\bar{\epsilon}_{ps}$ -measurements and metallographic studies of Clausing,<sup>(20,21)</sup> Spretnak, et al,<sup>(18,23)</sup> and the present study show a propensity for slip to become localized and concentrated and for cracks to form within the heavily sheared regions. These two features combine to curtail ductility.

#### 1. SIGNIFICANCE OF "PLANE-STRAIN" DUCTILITY

The "plane strain" ductility is an integrated measure of the rate with which the following three processes proceed with strain: 1) strain localization and concentration, 2) shear crack initiation, and 3) shear crack growth to the critical size. The signature of strain localization and shear rupture mode of separation is a fracture surface with "fine", closely spaced, submicron size dimple-like markings. This type of surface is situated between the relatively smooth, large, multimicron dimples associated with individual ruptured inclusion particles<sup>(14,32,33)</sup>. The fine dimples represent perturbations or ruptures produced by the strength giving precipitate particles in the matrix<sup>(14)</sup>, or possibly by intermediate particles<sup>(31)</sup> or void clusters.<sup>(19,34)</sup> The large, smooth dimples are the signature of the void nucleation and growth process which is competitive with strain localization and shear rupture. Consequently, the fracture of a material like AISI 4340 steel ( $\sigma_y \approx 1450 \text{ MNm}^{-2}$ ) with a small  $\bar{\epsilon}_{ps}$ -value corresponding to a low resistance to localization and shear rupture is expected to display more fine-dimpled regions on the surface than a material like the maraging steel ( $\sigma_y \approx 1300 \text{ MNm}^{-2}$ ) with a high  $\bar{\epsilon}_{ps}$ -value<sup>††</sup>. This is confirmed dramatically by the

<sup>†</sup> In the presence of a modest hydrostatic stress component, hydrostatic  $\approx 0.5 \sigma_y$ .

<sup>††</sup> Provided the resistance to void nucleation and growth are the same.

results summarized in Table 6, which indicates that the portion of fine-dimpled area varies inversely with  $\bar{\epsilon}_{ps}$ .

"Plane strain" ductility assumes special importance because notches and cracks enforce plane-strain flow and are therefore vulnerable to localization and shear rupture. Clausing<sup>(20)</sup> has shown convincingly that "plane strain" ductility values correlate closely with the toughness of notched bars. The present work, which indicates that Clausing's method significantly understates  $\bar{\epsilon}_{ps}$ -values, raises doubts about the idea that the "plane strain" ductility corresponds exactly with the critical notch root strain. But it does not alter the view that the processes governing ductility of "plane-strain" tension and bend specimens closely resemble the ones operating at the root of a notched bar. This is confirmed by metallographic studies of slip and cracking at the root of notched bars by Griffis and Spretnak<sup>(18)</sup> and McGarry<sup>(23)</sup> which show the same pattern of superbands and shear cracks as observed in "plane-strain" tension and bend specimens.<sup>†</sup> The important implication is that the surface of the "plane strain" tension or bend specimen can be regarded by the metallurgist as an accessible window for viewing the microscale processes governing the notch toughness.

## 2. CORRELATIONS BETWEEN $\bar{\epsilon}_{ps}$ AND $K_{Ic}$

There are reasons for anticipating that the correlation between "plane strain" ductility and toughness can extend to  $K_{Ic}$ -values. Sharp cracks also enforce "plane strain" flow. Further, Mohamed and Tetelman<sup>(22)</sup> find that the notch root

<sup>†</sup> McGarry's<sup>(23)</sup> value  $\bar{\epsilon}_{jr} = 0.27$ , the critical v-notch root strain for AISI 4340 steel ( $\sigma_y = 1103 \text{ MNm}^{-2} = 160 \text{ ksi}$ ) calculated from the bend angle, comes close to  $\bar{\epsilon}_{ps} = 0.35$ , the plane-strain ductility obtained here for this grade at a comparable strength level ( $\sigma_y = 1120 \text{ MNm}^{-2} = 165 \text{ ksi}$ ).

TABLE 6. RELATION BETWEEN FRACTURE MODE,  $\bar{\epsilon}_{PS}$  AND THE  $\bar{\epsilon}_{PS}$ -K<sub>IC</sub> CORRELATION

	$\sigma_Y$ MN/m <sup>2</sup>	$\sigma_Y$ Ksi	CONTRIBUTIONS OF SEPARATION MODES (%)			$\bar{\epsilon}_{PS}$	$\bar{\epsilon}_{PS}$ -K <sub>IC</sub> Correlation
			VOID NUCLEATION AND GROWTH	STRAIN LOCALIZATION AND SHEAR RUPTURE	$\bar{\epsilon}_{PS}$		
AISI 4340 (Cox & Low (14))	1410	(205)	3	97	-	0.16	-
AISI 4340 (present study)	1480	(214)	-	-	-	0.16	good
Aluminum Alloys 2014-T6, 2024-T851, 2124-T851 7079-T651 (Low, et al (13))	430-500 (63-73)		46-66	44-64	-	-	-
Aluminum Alloy 7075 Sheet and Plate (present study)	520-590 (75-85)		-	-	0.10-0.30	spotty	-
200 Grade 18 Ni-Maraging Steel (Cox & Low (14))	1330	(193)	-	~100	~0	-	-
250 Grade 18 Ni-Maraging Steel (present study)	1470-1840 (213-267)		-	-	$\geq 0.40$	no apparent correlation	-

strain is independent of root radius. In addition, there is evidence from the work of Rogers<sup>(19)</sup>, Yoder<sup>(5)</sup>, Beachem<sup>(36)</sup>, and Cox and Low<sup>(14)</sup> that the extension of cracks can proceed by concentrated shear and shear cracking along regions alternately inclined at +45° and -45° to the macroscopic crack plane. However, there are two reasons for believing, contrary to the views of Weiss and coworkers<sup>(37-39)</sup>, that the relation between  $\bar{\epsilon}_{ps}$  and  $K_{Ic}$  is not simple and direct or the same for all materials:

- 1) The applicability of a critical notch root strain concept to sharp cracks must be questioned. The gage length associated with the heavily deformed region adjacent to the crack tip is approximately equal to the crack (tip) opening displacement COD  $\approx 0.5 \frac{K_{Ic}^2}{\sigma_Y E}$  (40) or about 3  $\mu\text{m}$  to 10  $\mu\text{m}$  for high strength steels and aluminum alloys, respectively. These dimensions are of the same order as the width and offsets of individual slip bands. On this scale, the strain distribution is highly nonuniform and bears little relation to  $\bar{\epsilon}_{ps}$  --the average span for a gage section 100 x larger.
- 2) The state of stress is another important consideration. "Plane strain" tension and bend specimens support a modest hydrostatic stress ( $\sigma_{\text{hydrostatic}} \approx 0.5 \sigma_Y$ ), while the hydrostatic tension ahead of the crack tip under plane strain conditions is four times as large. Analyses and experiments by McClintock<sup>(16)</sup>, Argon, et al<sup>(41)</sup>, Rice and Johnson<sup>(8)</sup>, and Cox and Low<sup>(14)</sup> all show that the rates of void nucleation at inclusions and their growth are sensitive functions of the hydrostatic tension. In other words, void nucleation and growth can proceed much more rapidly in advance of a crack tip under plane strain than in the "plane strain" tension or bend specimen<sup>†</sup>. It

---

<sup>†</sup> The hydrostatic stress state should also affect microvoid nucleation and growth that contributes to the rupture stage of the strain localization and shear rupture process. However, shear rupturing at the crack tip probably occurs in the presence of voids and the heavily strained region adjacent to the crack root, and consequently under conditions where the "macroscale" hydrostatic stresses have been relieved. A large slip offset or partially cracked slip band can generate its own "microscale" hydrostatic stress state which will assist shear rupture, but the microscale hydrostatic stresses will be present in the "plane strain" tension or bend specimen as well as in the cracked specimen. For this reason, the "plane strain" tension specimen is expected to give an accurate representation of strain localization and shear rupture tendency at the crack tip.

follows that  $\bar{\epsilon}_{ps}$  values can give a good representation of  $K_{Ic}$  only when the contributions of void nucleation and growth to crack extension are small relative to those of localization and shear rupture. This is confirmed by the results of Table 6, which show that the degree with which  $\bar{\epsilon}_{ps}$  values correlate with  $K_{Ic}$  varies directly with the relative contribution made by the localization-shear rupture process. A different  $\bar{\epsilon}_{ps}$ - $K_{Ic}$  correlation is also to be expected when crack extension proceeds by cleavage (40,41).

### 3. FACTORS CONTRIBUTING TO THE STRAIN LOCALIZATION AND SHEAR INSTABILITY

The process of strain localization and shear rupture is accentuated by "plane strain" deformation. Micrographs of deformed surfaces of conventional and "plane strain" tension specimens suggest that the suppression of flow on the alternate  $\alpha'$ ,  $\beta'$  system (see Figure 4) favors a more coordinated slipping of neighboring grains. This rather subtle change sets the stage for an instability:

- (1) The coordinated slipping of grains produces an approximately coplanar array of slip bands and/or slipping grain boundaries referred to here as a "superband". Further deformation in the vicinity of the superband tends to proceed by the growth of the band in length and depth, rather than by the initiation of new bands. This is because the superband generates self-perpetuating stress concentrations at its extremities like a shear crack or dislocation pile-up.
- (2) By virtue of its size, the superband accommodates large shear strains which damage slip bands and/or boundaries and nucleate microcracks.
- (3) The coplanar nature of the array facilitates the linking up of microcracks, speeding up the development of a large unstable microcrack.

The degree of instability is related to the tendency for slip to concentrate in bands, and, while this is connected with strain hardening, it is not a direct

consequence of  $\frac{d\bar{\sigma}}{d\bar{\epsilon}}$ , the macroscopic hardening rate of the alloy. For example, the results obtained here for aluminum Alloy X show that the pattern of superbands is already established in the aged condition at  $\bar{\epsilon}_1 = 0.06$ , before the condition for macroscopic instability,  $\bar{\epsilon}_1 > \bar{\epsilon}_1$  (uniform) = 0.09, is obtained. Early stages of superband formation are also evident in the micrographs of the AISI 4340 steel at such a small strain  $\beta_1 = 0.05$ , and on a scale such that this cannot have any relation to the onset of the macroscopic instability. Note that the uniform elongation of this material,  $\bar{\epsilon}_1(u)$ ,--equivalent to the strain hardening index at this strain--is about the same for the 204°C and 538°C tempered condition in spite of ~ two-fold difference in  $\bar{\epsilon}_{ps}$ , and greater than the value for the 250-grade maraging steel,  $\bar{\epsilon}_{ps} = 0.40$ . Further evidence that the absolute magnitude of the strain hardening rate is not a reliable index of instability can be derived from observations of low strength steels.<sup>(42)</sup> These materials display prominent slip bands and strain concentrations long before the onset of necking in spite of high macroscopic rates of hardening.

The connection between the macroscopic strain hardening rate and the tendency for strain localization on the microscale becomes clearer by treating the high-strength alloy as a two-phase system consisting of heavily deformed bands (slip bands or grain boundaries) imbedded in a more lightly deformed matrix. To a first approximation (which ignores compatibility requirements) the macroscopic, or average, strain hardening rate can be expressed in terms of the hardening rates and volume fractions of the individual phases:

$$\frac{d\bar{\sigma}}{d\bar{\epsilon}} \approx f_M \frac{d\sigma}{d\epsilon} \Big|_M + f_B \frac{d\bar{\sigma}}{d\bar{\epsilon}} \Big|_B \quad (2)$$

where the subscripts M and B refer to the matrix and the bands. The mechanical stability requirement leads to a second expression relating the local strains, flow stresses, and hardening rates,

$$\bar{\sigma}_M + \frac{\partial \bar{\sigma}}{\partial \bar{\epsilon}} M d\bar{\epsilon}_M \approx \bar{\sigma}_B + \frac{\partial \bar{\sigma}}{\partial \bar{\epsilon}} B d\bar{\epsilon}_B \quad (3)$$

The implications of such a model are generally consistent with observations of the preceding paragraph:

- 1) Strain localization--slip bands and slipping grain boundaries--arises when the matrix is initially harder or is hardening at a greater rate than the more heavily deformed slip bands, independently of the average strain or macroscopic hardening rate.
- 2) Large differences in strain between the matrix and the bands reflect large differences in the local hardening rates or in the initial flow stress or both.
- 3) The macroscopic strain hardening rate--the value ordinarily derived from tensile tests--depends on the hardening rates and the volume fractions of the individual constituents. While the macroscopic rate is between those of the matrix and the bands, it will not reflect the behavior of the bands if their volume fraction is small and their hardening rate is substantially different from the matrix. In this simplified model the macroscopic rate, by itself, offers no insight to the tendency for strain localization on the microscale. The absolute value of the macroscopic hardening rate enters only in the following way: A given absolute change in the flow strength of one of the constituents has a larger effect on  $\frac{\bar{\epsilon}_B}{\bar{\epsilon}_M}$  (the ratio of the strain of the band to that of the matrix) the smaller the macroscopic hardening rate of the alloy.

#### 4. MICROSTRUCTURAL CONTRIBUTIONS TO STRAIN LOCALIZATION AND SHEAR RUPTURE

Strain localization is caused by a relative softness or softening on the part of the slipping regions compared to the matrix. The present studies indicate this can be traced to a number of microstructural processes.

Dislocation Cutting of Coherent Precipitate Particles. The cutting-through of small, coherent precipitates by dislocations--as opposed to bypassing--undermines the hardening process and leads to a relative softening of the slip band. Detailed analyses by Rau and Cook<sup>(43)</sup> show that the stress concentrations produced by an array of dislocations cutting through a series of particles quickly lead to a nonhardening steady state. In addition, each dislocation passing through a particle reduces the shear-resisting cross section of the particle. Recent experimental studies by Klein<sup>(44)</sup> and by Hornbogen and Gahr<sup>(45)</sup> demonstrate the connection between cutting and the formation of coarse slip bands with large offsets. Consistent with this, the  $\epsilon$ -carbide particles, which are formed in the as-quenched carbon steel-like AISI 4340, in the first stage of tempering (120°C-200°C) appear to be relatively thin, coherent laths, ~10-25 Å thick<sup>(46)</sup>, which will be vulnerable to cutting. The  $\epsilon$ -particles are gradually replaced by more massive, partially coherent cementite particles in the range 200°C-400°C and are accompanied by a ~two-fold improvement in "plane strain" ductility. In contrast, there is evidence that dislocations in the 250-grade maraging steel bypass particles<sup>(47,48)</sup>. Since the resistance of particles to cutting diminishes with decreasing coherent particle size<sup>(44)</sup>, the finer particle distributions, which are required for high strength, also tend to be more vulnerable to slip localization.

Rupture of Inclusion Particles. Slip bands in the AISI 4340 steel and the 7075 aluminum alloy sheet and plate were frequently associated with ruptured inclusions visible on the surface. It therefore seems likely that the bands were involved with broken inclusions below the surface. The strain concentrations produced by these voids help nucleate the slip bands and may represent "easy" shear paths, which, in effect, lower the hardening rate attributed to a band as envisioned by McClintock<sup>(16)</sup>. Broek<sup>(49)</sup> has offered some evidence that the final stages of the rupture of aluminum alloys are nucleated in this way by the failure of the inter-

mediate particles. It is also interesting to note that Parker and Zackay<sup>(49)</sup> find that austenitize to temperatures above 1000°C improve the toughness of low alloy steels. Since the principle effect of these treatments is to dissolve the more stable carbide particles, one may speculate that the rupture of such particles promotes the formation of slip bands.

Grain Boundary Phenomena. Both segregation and altered transport kinetics in the locale of grain boundaries can alter the nature and distribution of alloying constituents and precipitates, thereby reducing the strength of the regions adjacent to the boundary relative to the matrix. Studies by Dahmen and Hornbogen<sup>(50)</sup> reveal that this can lead to a significant amount of grain boundary sliding--offsets  $\sim 1 \mu\text{m}$  at room temperature--for an aged, 4% Fe-aluminum alloy. The present study provides evidence of marked room temperature grain boundary sliding and rupture in the 7000-type aluminum Alloy X in the slightly overaged condition, in specimens of the 7075-plate in the TS orientation, and in the 250 grade maraging steel and the Ti-6Al-4V alloy.

Cut or fractured precipitate particles can be the nuclei of the microvoids whose growth and coalescence lead to the shear rupture of slip bands--Rogers'<sup>(19)</sup> "void sheets", Griffis and Spretnak's<sup>(18)</sup> "slip decohesion", and Beachem and Yoder's<sup>(36)</sup> "homogeneous microvoid coalescence"--or to the failure of slipping grain boundaries. Recent work by Wilsdorf<sup>(34)</sup> on high purity silver contains evidence that voids can also be nucleated in strained regions even the absence of particles. The present slip offset measurements for the AISI 4340 steel seem to show that the maximum slip band offsets--the ones observed at the failure strain,  $\bar{\epsilon}_{ps}$ --are independent of tempering temperature. It appears that the strain does not concentrate as readily at the higher tempering temperatures, but the shear rupture resistance of the bands is not enhanced. The offsets displayed by cracked slip

bands of the 7075 alloy sheet and plate, ~ 2-4 even in the fully aged condition, are also essentially invariant. This is important, because the length of the superbands is strongly influenced by the grain structure. For example, the extent of the superbands of the LS-orientation is limited by the closely spaced, transverse boundaries, and this limits the slip band offsets accommodated with the band. As a result this orientation displays an  $\bar{\epsilon}_{ps}$  value two to three times as large as the other orientations. These findings, which point to a grain size dependence of "plane strain" ductility and account for the procurement grain size dependence of fracture toughness of aluminum alloys, are shown in Figure 55. (33,51)

## 5. GENERAL GUIDELINES FOR CONTROLLING THE $K_{Ic}$ VALUES OF HIGH STRENGTH ALLOYS

The present study supports the view that the crack extension of high strength alloys proceeds by one mode or a combination of two competitive modes of separation,

- 1) void nucleation and growth on the scale of the micron-size inclusions and
- 2) strain localization and shear rupture, wherein the void nucleation and growth process are shifted to the scale of the fine, strengthening precipitate particles.

The factors regulating the first mode are identified in the introductory sections.

To these can be added the following factors which affect the strain localization shear rupture mode.

Plane-Strain Ductility. The plane strain ductility is a measure of a material's resistance to strain localization and shear rupture. It also reflects the value of  $K_{Ic}$  in those cases where the contribution of the competing void nucleation and growth mode is relatively small.

Size and Character of Precipitate Particles. Small, coherent, precipitate particles which are vulnerable to cutting by dislocations will promote strain localization and reduce the toughness.

Grain Size and Character. Grain boundaries act as barriers to slip bands and tend to resist the growth of superbands, and the development of large, damaging slip offsets. However, alterations in the locale of grain boundaries that promote grain boundary sliding can provide an "easy" path for strain localization and shear rupture.

Inclusion Particles. Broken inclusion particles nucleate slip bands and provide easy shear paths. It seems likely that the elimination of extraneous particles will enhance the toughness contributed by the strain localization-shear rupture mode.

Yield Stress and Strain Hardening Index. To the extent that high yield stress and low strain hardening rate values reflect the presence of small, cuttable precipitate particles, these flow properties will be indicative of poor toughness. However, neither the yield stress nor the strain hardening index are by themselves reliable measures of the strain localization and shear rupture tendency.

## SECTION V

### CONCLUSIONS

1. Measurements of the distribution of strain along the tensile axis show that the "plane strain" (double) bend specimen and the Clausing "plane strain" tensile specimen display the same peak value of principle tensile strain at fracture--a strain which has been termed the "plane strain" ductility. However, the strain derived from the reduction in thickness at the center of the Clausing test piece--the previous method for evaluating this quantity--underestimates the "plane strain" ductility. Even so, the present studies confirm that "plane strain" flow curtails the ductility of high strength alloys significantly relative to that obtained with conventional, round tensile bars.
2. Metallographic studies of the AISI 4340 steel, maraging steels, Ti-6Al-4V and 7000-series type aluminum alloys, show that "plane strain" flow favors a more coordinated slipping of neighboring grains in high strength alloys. This leads to the formation of coplanar arrays of slip bands or sliding grain boundaries extending over many grains, which are referred to here as "superbands".
3. The superbands curtail ductility in a number of ways. Superbands tend to grow at the expense of isolated slipping regions because they produce self perpetuating stress concentrations at their extremities. The large bands accommodate slip bands or boundaries with large shear strains that damage slip bands and sliding grain boundaries. Microshear cracks are initiated within the slipping regions. Finally, the coplanar nature of the superbands facilitate the linking up of microcracks into an unstable macrocrack.

4. Slip in quenched and tempered AISI 4340 steel and in the aged 7075 aluminum alloy tends to be localized in transgranular slip bands. Microshear cracks are observed at the base of slip bands with 2-4  $\mu\text{m}$  offsets. The maraging steels and the Ti-6Al-4V alloy display transgranular slip bands, but the superbands and microshear cracks in these alloys, are associated mainly with grain boundary sliding and rupture, were also prominent in coarse grained, high purity and overaged 7000 series aluminum alloy and in aged specimens of the 7075 alloy of the TS-orientation which have vulnerable grain boundaries.

5. Measurements of the distribution of the size of slip band offsets also correlated with "plane strain" ductility values. At comparable plane strain levels, the low toughness 204°C tempered condition of the AISI 4340 steel displayed larger slip offsets than the tougher 538°C tempered condition; at fracture, the slip offsets for these two conditions were very similar. Consistent with this, the 250-grade and 300-grade maraging steels exhibited higher plane strain ductility values and a more nearly uniform distribution of slip bands with noticeably smaller offsets.

7. The "plane strain" ductility,  $\bar{\epsilon}_{ps}$ , is a measure of a material's resistance to strain localization and shear rupture (shear microcrack nucleation, linking up, and growth to critical size) under "plane strain" flow conditions.

8. Metallographic studies of the surfaces of "plane strain" tension and bend specimens provide insights to the microstructural features controlling the strain localization and shear rupture instability. They also provide access to microstructural features affecting notch toughness and  $K_{Ic}$  in cases where strain localization and shear rupture contributed to crack extension.

9. The relation between  $\bar{\epsilon}_{ps}$  and related metallographic studies, on the one hand, and  $K_{Ic}$  values, on the other, depends on the contribution of the strain localization-shear rupture mode relative to the void nucleation and growth mode of separation in the case of AISI 4340 strain localization, and shear rupture is the dominant mode. In 200-grade maraging steel crack extension proceeds exclusively by nucleation and growth of voids at micron size inclusions. In aluminum alloys the contributions of the two modes are comparable. Consistent with this,  $\bar{\epsilon}_{ps}$  values of AISI 4340 steel in different tempering conditions correlate with  $K_{Ic}$ . The variation of  $\bar{\epsilon}_{ps}$  values with aging of 7000-series type aluminum sheet and plate is similar to that displayed by  $K_{Ic}$ . Finally, the  $\bar{\epsilon}_{ps}$  values for the maraging steel do not reflect the large changes in toughness that accompany maraging.

10. Strain localization is caused by a relative softness or softening on the part of the slipping regions compared to the matrix. The macroscopic strain hardening rate--the value ordinarily derived from tensile tests--does not reflect the difference between the hardening rate of the matrix and the slip band and is therefore not a reliable indicator of the tendency for strain localization.

11. There are a number of metallurgical factors that promote strain localization and shear rupture, thereby degrading the fracture toughness of high strength alloys vulnerable to localization. Small, coherent precipitate particles, which are cut by dislocations promote strain localization and shear rupture. Grain boundaries act as barriers to slip bands and tend to resist the growth of superbands and large damaging slip offsets. For this reason, a large grain size can be detrimental to fracture toughness. Grain boundary segregation phenomena that soften the boundary with respect to sliding can reduce toughness. Finally, there are indications that broken particles and inclusions, which nucleate slip bands and provide easy shear paths, may reduce toughness.

### REFERENCES

1. R. Develay: Metals and Materials, 6, 404 (1972).
2. W. S. Pellini: "Integration of Analytical Procedures for Fracture-Safe Design of Metal Structures", NRL Report 7251, March 26, 1971.
3. A. R. Rosenfield: Met. Rev. No. 121 (1968).
4. G. T. Hahn, M. F. Kanninen, and A. R. Rosenfield: Ann. Rev. Mat. Sci., 2, 381 (1972).
5. J. M. Krafft: Rep. NRL Progr. (1963) p. 4.
6. F. A. McClintock: Ductility, Ed. H. W. Paxton, p. 255, American Society for Metals, Metals Park, Ohio, 1968.
7. P. F. Thomasson: Int. J. Fract. Met., 7, 409 (1971).
8. J. R. Rice and M. A. Johnson: Inelastic Behavior of Solids, eds., M. F. Kanninen, et al., McGraw-Hill, N.Y., p. 641 (1970).
9. G. T. Hahn and A. R. Rosenfield: "Relations Between Microstructure and the Fracture Toughness of Metals", Proc. Third Int. Conf. Fracture, Munich, 1973.
10. A. J. Birkle, R. P. Wei, and G. E. Pellesier: Trans ASM, 59, 981 (1966).
11. J. J. Hauser and M. G. Wells: Tech. Rep. AFML-TR-69-339, Wright-Patterson AFB, Ohio (1969).
12. J. P. Tanaka, C. A. Pampillo, and J. R. Low, Jr.: ASTM-STP 463, 191 (1970).
13. R. H. Stone, R. H. Merchant and J. R. Low, ASTM STP 556, p. 93 (1974).
14. T. B. Cox and J. R. Low, Jr.: NASA Tech. Rep. No. 5 on Research Grant NGR-39-087-003, Carnegie-Mellon University (May, 1973).
15. J. H. Mulherin and H. Rosenthal: Met. Trans., 2, 427 (1971).
16. F. A. McClintock, S. M. Kaplan, and C. A. Berg: Int. J. Fract. Mech., 2, 615 (1966).
17. C. A. Berg: Inelastic Behavior of Solids, M. F. Kanninen, et al, eds. (McGraw-Hill, New York) (1970), p. 171.
18. C. A. Griffis and J. W. Spretnak: J. Iron Steel Inst. Japan, 9, 372 (1969).
19. H. C. Rogers, Trans. AIME: 216, p. 498 (1960).

D. P. Clausing: Int. J. Fract. Mech., 6, 71 (1970).

D. P. Clausing: Tech. Rep. on Project No. 35.066-001(2), U. S. Steel Corp., Research Lab. (1972).

S. A. Mohamed and A. S. Tetelman: Third Int. Conf. on Fracture, Munich, 1973, Paper II-511.

D. L. McGarry: M. S. Thesis, The Ohio State University (1972).

A. S. Tetelman: Univ. of Cal. at L.A., private communication (1973).

V. Weiss and N. Sengupta: Third Int. Conf. on Fracture, Munich, 1973, paper III-341.

M. H. Jones and W. F. Brown, Jr.: "Review of Developments in Plane Strain Fracture Toughness Testing", ASTM STP 463, 1970, pp. 63-101.

E. B. Kula and A. A. Anctil: J. Matls., 4, No. 4, pp. 817-841, (December 1969).

J. E. Srawley: Fracture 1969, Ed. P. L. Pratt, p. 131, Chapman and Hall, London, 1969.

W. T. Matthews: AMMRC MS 73-6 (1973).

J. G. Kaufman, F. G. Nelson, and M. Holt: Engineering Fract. Mech., 1, 259 (1968).

T.M.F. Ronald and D. P. Voss: AFML/LLS, Wright-Patterson AFB, Ohio (unpublished research).

D. Broek: Report NLR-TR-72029-u; Nat. Aerospace Lab, The Netherlands (n.d.).

G. T. Hahn and A. R. Rosenfield: "Metallurgical Factors Affecting Fracture Toughness of Aluminum Alloys", Met. Trans. (to be published).

R. W. Bauer and H.G.F. Wilsdorf: Scripta Met., 7, 1213 (1973).

G. R. Yoder: Met. Trans., 3, 1851 (1972).

C. D. Beachem and G. R. Yoder: Met. Trans., 4, 1145 (1973).

Volker Weiss, M. Sengupta, and W. Sanford: "The Significance of Material Ductility to the Reliability and Load Carrying Capacity of Peak Performance Structures (U)", Final Report, Contract No. N00019-72-C-0214, NASC (1973).

N. Levy, P. V. Marcal, W. J. Ostergren, and J. R. Rice: Int. J. Fract. Mech., 7, 143 (1971).

A. S. Argon, J. Iin, and R. Safoglu: "Cavity Formation From Inclusions in Ductile Fracture", Met. Trans. (to be published).

40. J. M. Barsom and J. V. Pellegrino: Eng'g. Fract. Mech., 5, 209 (1973).
41. V. Weiss, K. Schroder, W. Sanford, H. Chandan, T. Kunio, D. Lal, and M. Sengupta: "The Relationships Between the Transformation Characteristics and the Fracture and Fatigue Properties of Trip Steels", AMMRC CTR 73-50, December, 1973.
42. A. R. Rosenfield and G. T. Hahn: Met. Trans., 1, 1080 (1970).
43. C. A. Rau, Jr. and T. S. Cook: "Solid Mechanics of Flow Fracture Creep and Fatigue", PWA-4868, November, 1973.
44. H. P. Klein: Z. Metallkde, 61, 564 (1970).
45. E. Hornbogen and K. H. Zum Gahr: "Distribution of Plastic Strain in Alloys Containing Small Particles (to be published).
46. B. N. Ranganathan and H. E. Grenga: Phil. Mag., 30, 161 (1974).
47. S. Floreen: Met. Reviews (Review 126), 115 (1968).
48. B. G. Reisdorf and A. J. Baker: AFML TR 64-390, 1965.
49. E. R. Parker and V. F. Zackay: Eng'g. Fract. Mech., 5, 147 (1973).
50. U. Damen and E. Hornbogen: "Grain Boundary Sliding in Polycrystalline Aluminum" (to be published).
51. A. R. Rosenfield, C. W. Price, C. J. Martin, D. S. Thompson, and R. E. Zincham: "Research on Synthesis of High Strength Aluminum Alloys", AFML TR 74-129, Part 1, December, 1974.

## APPENDIX

### MEASUREMENT OF SLIP OFFSET DISTRIBUTION

Measurements of the distribution of the sizes of slip-offsets (the dimension  $l$  in Figure A1) visible on the surface were obtained from shadowed cellulose acetate replicas by using the following simplified interpretation. The explanation is facilitated by the following symbols defined in Figure A-1:

$l$  - slip band offset

$h$  - slip band height

$w$  - width of the slip band or slip band shadow

$\alpha$  - inclination of the slip band

$\phi$  - angle between the shadowing beam and the plane of the replica

$\theta$  - angle between the shadowing beam and the projection of the slip band/shadow into the plane of the surface.

The dimension  $h$  can be obtained when the slip band casts a shadow (when  $0 < \alpha < \frac{\pi}{2}$ ) from measurements of  $w$ , the width of the shadow, and the angles  $\phi$  and  $\theta$ :

$$h = w \frac{\tan \phi}{\sin \theta} \quad (A-1)$$

The offset  $l$  can then be determined if the orientation of the slip system is known. In the case of polycrystalline samples, where the orientation of the different slip systems is not known, the dimension  $l$  can be determined for one special case, when portions of the surface of the offset are visible and portions are featureless, an indication that  $\alpha \approx \phi$ . However, relatively few slip bands will normally be inclined at this angle, and these do not necessarily represent a random sampling. To obtain a larger and random sampling, offsets were approximated for all the slip bands

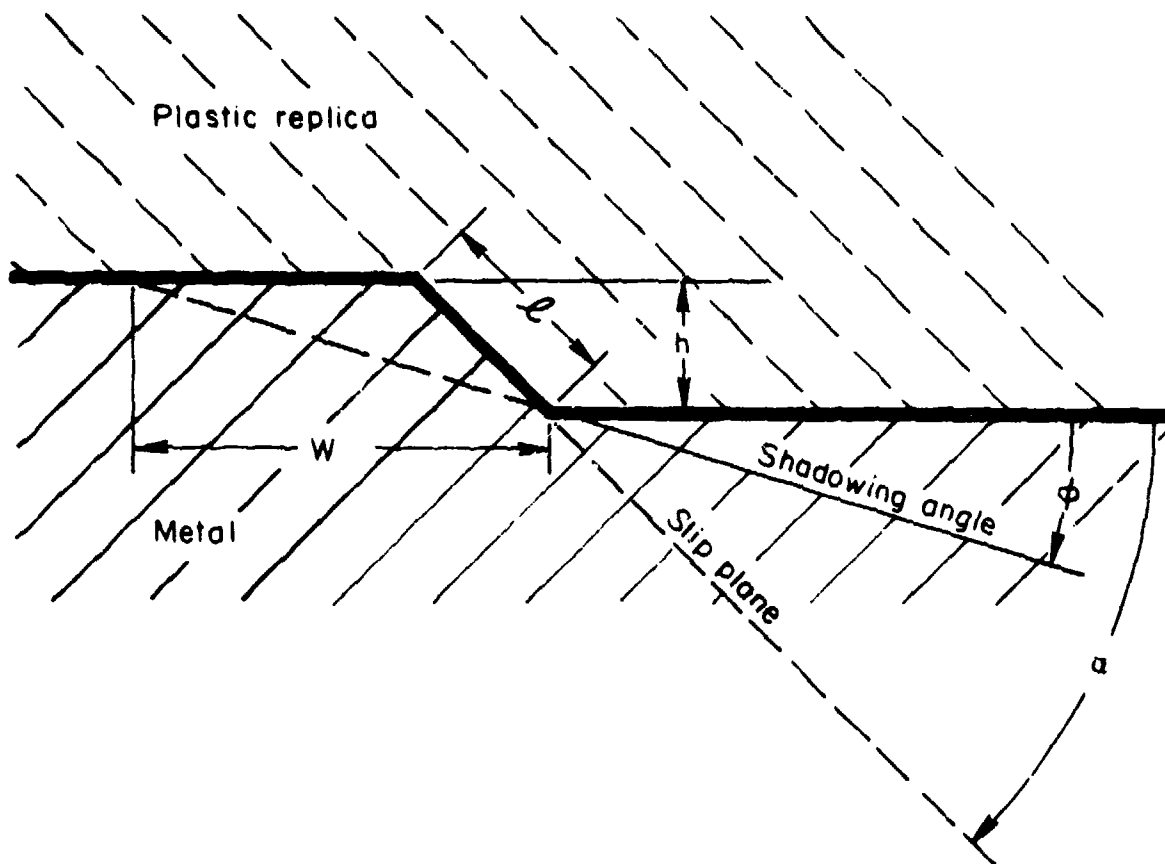


FIGURE A-1. SCHEMATIC REPRESENTATION OF SLIP BAND OFFSET ON METAL AND ON THE PLASTIC REPLICA

visible on the replica. This was done by dividing the bands into 4 categories based on the contrast between either the band or its shadow and the background. Values of  $l$  were then calculated from  $h$  or  $w$  under the assumption that the average inclination  $\bar{\alpha} \approx \frac{\pi}{4}$  ( $\phi$  was normally 10-15 degrees).

Category 1. Slip band offset surface is visible, but band is lighter than background;  $0 < \alpha < \phi$ ;  $l \approx w$ .

Category 2. Slip band offset appears white and fractureless;  $\phi < \alpha \leq \frac{\pi}{2}$ ;  $l \approx 1.4 h$ .

Category 3. Slip band offset surface is partly visible and partly featureless;  $\alpha \approx \phi$ ;  $l \approx w$ .

Category 4. Slip band offset surface is darker than background;  $-\frac{\pi}{2} < \alpha < 0$ ;  $l \approx 1.4 w$ .

In those cases where the slip offset was terraced (see Figure 50), the terraces were arbitrarily ignored as long as they represented less than 30% of the offset; otherwise the terraced band was interpreted as a group of closely spaced bands.

Figure A-2 compares two sets of measurements performed on different micrographs of the same surface, which show that measurements made in this way are quite reproducible.

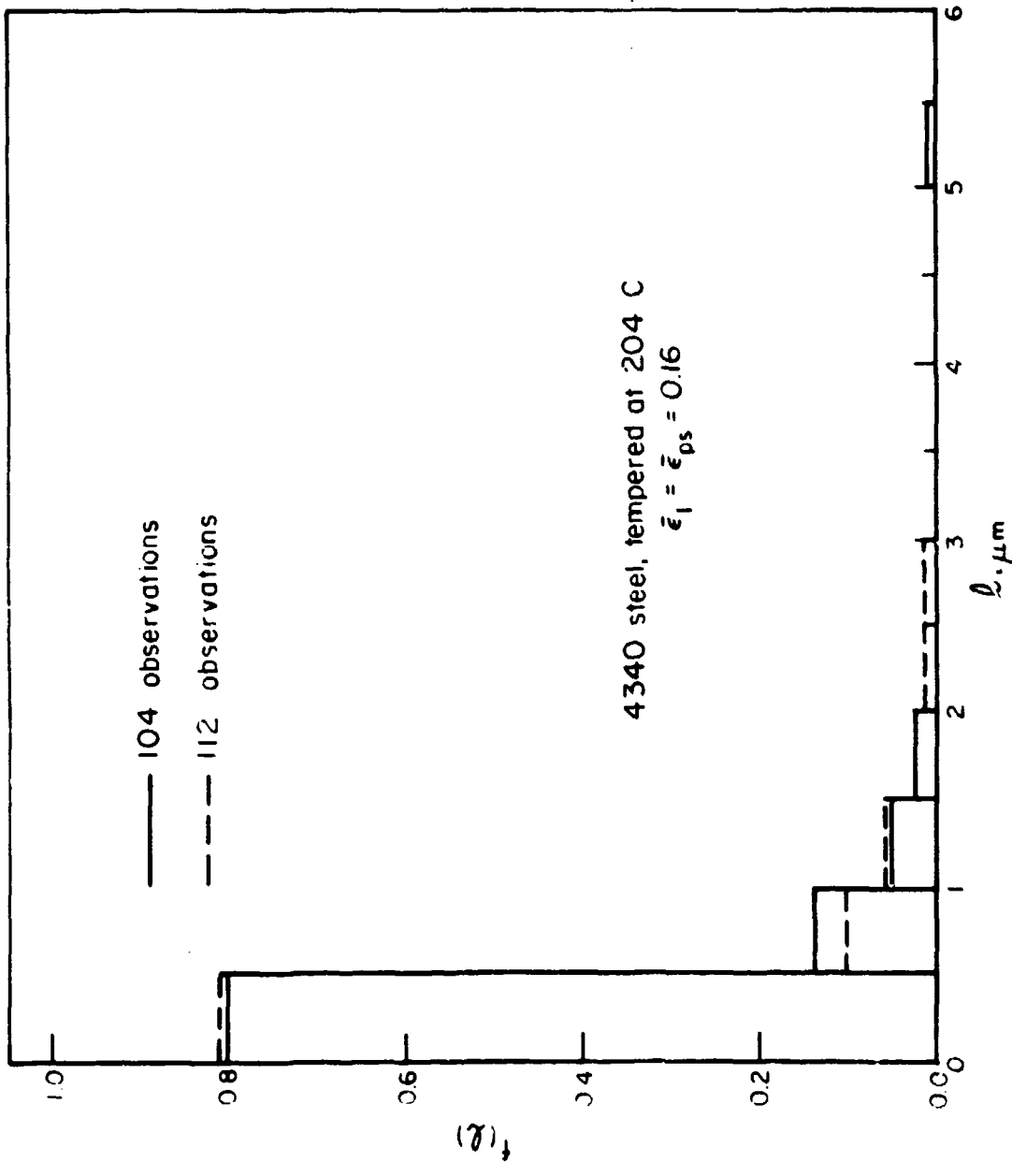


FIGURE A-2. DISTRIBUTION OF SLIP OFFSETS ON ELECTRON MICROGRAPH REPLICAS OF 4340 STEEL